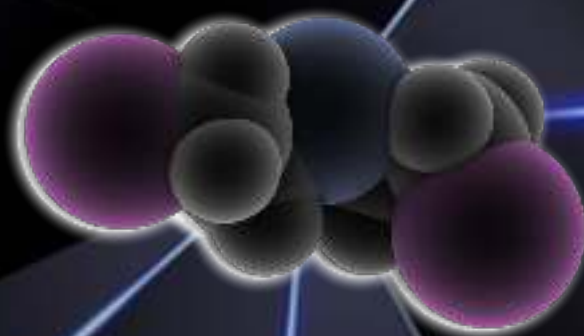# Adsorption of Harmful Gases from Air Using Porous Materials

Ismael Matito Martos

Adsorption of Harmful Gases from Air Using Porous Materials

By

ISMAEL MATITO MARTOS

Licenciado en Ciencias Ambientales

Department of Physcal, Chemical and Natural Systems

UNIVERSIDAD PABLO DE OLAVIDE

SUPERVISORS

Sofía Calero

Prof. Universidad Pablo de Olavide

Ana Martín Calvo

Dr. Universidad Pablo de Olavide

Dissertation submitted to obtain the degree of Doctor with International Mention.

SEVILLE, JULY 2019

0000-0002-2107-0927

Cover has been designed using images from Freepik.com

- **Doctoral Supervisors**

    Prof. Sofía Calero

    Dr. Ana Martín Calvo

- **Examination Committe**

    Chair: Prof. Joaquín Silvestre-Albero

    Secretary: Dr. Juan M. Castillo

    Member: Prof. Flor Siperstein

- **External Committe**

    Prof. Titus Sebastiaan van Erp

    Dr. Ozgur Yazaydin

Table of Contents

Introduction

This thesis deals with the use of post-production solutions for the capture and reduction of a variety of pollutants. For this purpose, nanonporous materials have been successfully proven to have an excellent performance as molecular sieves. The nanostructured channels and cavities and the diverse chemical composition of these materials give to them some attractive properties for adsorption and separation processes (i.e. high surface area and pore volume, channels of molecular size, and thermal stability). Among others, most explored materials include zeolites, metal-organic frameworks (MOFs), pillared clays, and activated carbons. Due to the huge amount of possible structures to explore and taking into account that sometimes experiments with certain pollutants exhibit practical and safety complications, the use of an alternative strategy to guide experimental procedures is required. In this regard, molecular simulation allows to study the interactions that take place between the adsorbates of interest and a large amount of real and hypothetic materials with very low cost and no safety risk associated [1, 2]. Simulation techniques are used in this thesis to explore the suitability of a variety of materials for the capture and removal of molecules with environmental relevance. Adsorption and diffusion processes are calculated for in zeolites and MOFs, providing useful information about the mechanisms that govern at molecular level the capture and separation processes of pollutants including combustion gases (SO_2, CO_2, CO, and NO_x) , greenhouse gases (SF_6), and chemical warfare agents (mustard gas, sarin, and soman).
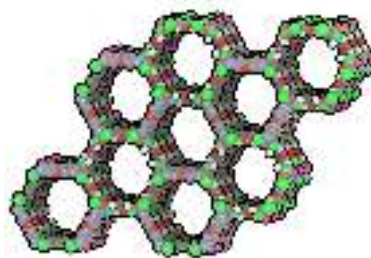
1.1 CAPTURE OF HARMFUL GASES FROM AIR

Nowadays, global energy demands strongly depends on burning fossil fuels such as coal, petroleum, and natural gas for electricity, heat, and transportation [3]. However, the use of fossil fuels produces a large amount of pollutants. These gases include not only carbon dioxide, but also carbon monoxide, sulfur dioxide, and nitrogen oxides, that reduce air quality and affect climate change.

Carbon dioxide (CO_2) is considered the main responsible of global warming along with other environmental problems. In fact, the growing concentration of CO_2 in atmosphere caused by anthropic emissions has become global climate change a severe problem [4]. In this concern, many efforts have been made to reduce emissions of greenhouse gases in general, and CO_2 in particular. Among others, carbon capture and sequestration (CCS) technology has been proposed for reducing CO_2 emissions. In this process, CO_2 is concentrated from a gas steam and injected into geological formations for permanent storage [5, 6]. However, combustions gases typically contain traces of others compounds such as sulfur and nitrogen oxides, and carbon monoxide [7, 8]. These traces strongly reduce the efficiency of the CSS process by affecting the CO_2 selective capture [9–11].

In addition to reduce the efficiency of CCS processes, sulfur and nitrogen oxides are gases with relevant environmental impact and capital importance in atmospheric chemistry. Sulfur dioxide (SO_2), a typical component of fuel combustion exhausts from coal fire plants, is a toxic and irritant gas and, along with NO_x, the main precursor of acid rain when combined with water vapor [12, 13]. Nitrogen monoxide (NO) and nitrogen dioxide (NO_2) are commonly generated from internal combustion engine exhaust and power station boilers [14, 15]. These gases are also toxic to human inhalation and have a high reactivity with the oxygen from air. They are precursors of tropospheric ozone and other secondary pollutants when they react with oxide volatile organic compounds in presence of sunlight. The release of NO_x from combustion also favors photochemical reactions resulting in photochemical smog. Carbon monoxide is another gas typically formed by burning carbon-based fuels. This toxic gas prevents the ability of our bodies from transporting oxygen due to its high affinity to hemoglobin protein. Regarding to global warming, there are some other gases with high relevance. One of them is sulfur hexafluoride (SF_6), a strong greenhouse gas with a global warming power about 23.900 times larger than CO_2 [16, 17]. As a result of its different uses, mainly in the electrical industry as insulating gas [18], its atmospheric concentration has been increased from less than 1 ppt in 1975 to about 7-8 ppt nowadays [19, 20].

Another class of toxic compounds that have been received great attention are

chemical warfare agents (CWAs) such as sarin, soman, or sulfur mustard. They are highly toxic compounds intentionally designed and released to cause harm, death, temporary incapacitation or sensory irritation. Major international efforts to prohibit the use of these chemicals, or protection against deliberate attacks are still critical challenges. However several countries are believed to still have stockpiles and operational production facilities [21]. Nowadays, population exposure to nerve gas attacks has continued occurring; for example, chemical attacks in Syria reported in 2013 and 2016 [22]. For this reason, the development of suitable defenses against these weapons are highly needed [23, 24].

The effects of these gases on the environment and the human health, along with increasing concerning about air quality lead to the establishment of more restrictive levels of emissions. In this regard important efforts have been made to reduce and control their emissions and to selectively capture harmful gases from air. There are two main approaches to achieve this aim. One focuses on the production process itself, trying to reduce the amount of gases generated. This strategy includes for example the reduction of the amount of nitrogen and sulfur compounds in fuels before combustion or the use of inert gases such as nitrogen in mixtures with SF_6, keeping all its interesting properties while reducing the amount of SF_6 used. The other approach includes

strategies to efficiently capture the harmful gases after production [25–28]. One example is the wet amine scrubbing method such as monoethanolamine (MEA) for the chemical CO_2 absorption [26, 27]. Sulfur dioxide removal via scrubbing is also the most widely applied approach for the post-combustion removal of this gas. Sulfur hexafluoride can be also decomposed by plasma, electrical discharge, or spark [29]. However, all these methods rely on high energy consumption to regenerate the absorbent solutions, solvent loss due to the degradation and evaporation, and high equipment corrosion [25, 27]. For example, approximately 70% of the cost of CCS is associated with the selective capture of CO_2 and the large energy input required for regeneration of the capture material [6]. Unfortunately, these processes also generate large amounts of solid wastes and off-gas streams whose further management entails the most important drawback of this approach. In the case of CWA, detoxification methods involve hydrolysis or incineration [30]. However, incomplete incineration can pose a serious risk of accidental exposure. Besides, hydrolysis leads to relatively slow and ineffective processes for non-miscible CWAs such as sulfur mustard (HD) [31]. The selective catalytic reduction (SCR) is also used to process the off-gas stream containing SO_2 [32], NO_x [33, 34], or SF_6 [19, 35]. SCR leads to high decomposition ratios with fewer wastes produced.

The minimization of the energy input

for the regeneration of absorbent materials and the reduction of secondary wastes are important challenges to improve the capture strategies and to accelerate the implementation of this technology [11, 36]. For this purpose, physical adsorption using solid adsorbents as molecular sieves has emerged as a promising alternative. This solution includes porous crystalline materials such as porous carbons [37, 38], zeolites [39, 40], or metal-organic frameworks [4, 41–43]. This method reduces both the production of wastes and energy requirements, and the efficiency of the process is even better than for SCR solutions [44, 45].

1.2 MOLECULAR SIEVES

Two main groups of materials with different composition and properties are used in this thesis. A general description of zeolites and Metal Organic Frameworks (or MOFs), is included in the following section. Details of specific materials can be found in the specific chapters.

1.2.1 Zeolites

Zeolites are silicates consisting of tetrahedral units with four oxygen atoms (O atoms) bonded to atoms of silicon, aluminum, or other metal (T atoms) [46]. The tetrahedra Primary Building Units (PBUs, Figure 1) are connected by the oxygen atoms, generating Secondary Building Units (SBUs). The combination of SBUs

creates ordered and nanostructured three-dimensional networks (Figure 1) with pores, windows, and channels of molecular size (3-14 Å in diameter). When an aluminum atom replaces an atom of silicon, it generates a negative net charge in the structure. This charge is balanced by the addition of protons and/or cations to the system [47, 48]. Tetrahedra containing aluminium should obey the Lowënstein rule [49]. According to this rule the Al-O-Al connection is forbidden. The shape and size of channels, windows and cavities as well as the silicon/aluminum ratio, and the presence of several cations are very important features because they influence the adsorption and separation properties of the materials. Due to these different possibilities, there are about 48 natural zeolites and more than 240 synthetic structures [49, 50].
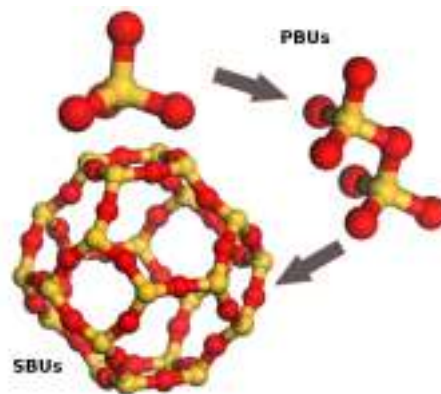
Figure 1. Graphical representation of tetrahedral Primary and Secondary Building Units (PBUs and SBUs) of zeolites. Oxygen and silicon atom are depicted in red and yellow, respectively.

The highly ordered structure gives to zeolites interesting properties like high surface area, thermal stability, ion exchange capacity, or fluid permeability [51–53]. These characteristics make zeolites good materials for storage, separation, and purification of gas mixtures [54]. Zeolites are also used in industry like fertilizer, food supplement for fish farms, ionic exchanger, and catalyst for many reactions with organic molecules like cracking and hydrocracking, isomerization, and synthesis of hydrocarbons [55]. Furthermore, zeolites are used on environmental applications in treatment of water, as filters for the removal of heavy metals, ammonium, and sludge; and soils, to immobilize heavy metals and others metallurgical wastes [56–58]. Zeolites are also useful as molecular sieves to capture gases with small sizes as Volatile Organic Compounds (VOCs) or some greenhouse gases (CO_2 or N_2O, among others) [59].

In this thesis *c.a.* 200 pure-silica zeolite structures from the International Zeolite Association (IZA) are used [50]. In order to obtain topological insights of the adsorption and diffusion processes, every single structure was characterized using Zeo++ software [60]. For each zeolite, Zeo++ calculates dimensionality of the pore system, the diameter of the largest included sphere (Di), the largest free sphere (Df), and the largest included sphere along the free sphere path (Dif). Di measures the largest opening in the structure while Df measures the restriction along the dif-

fusion pathway of the largest spherical probe. Figure 2 shows a representation of the characterization parameters. For a better understanding, each characterized zeolite is classified according the corresponding directionality of the pore space (i.e 1D,2D, or 3D). Additionality, the pore system is classified acording to the ratio of Dif and Df. A channel is recognized for structures with Dif/Df < 1.5, and an interconnected cage system otherwise. A representative set of zeolites of each of these six classes is used in Chapters 2, 3, and 4 to study the selective adsorption and diffusion performance of smalls gases.
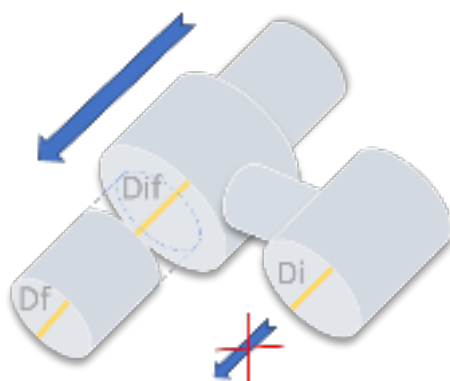
Figure 2. Graphical representation of the characterization parameters used for the clasification of zeolite structures.

1.2.2 Metal Organic Frameworks

Metal-organic frameworks (MOFs) are a relatively new class of synthetic crystalline porous materials. The first MOF material was reported in 1999 by Yaghi *et al.* [61]. Since then, they have received a

great attention becoming one of the most studied nanonporous materials [21, 62]. Nowdays, *ca.* 84.000 MOFs materials have been already synthesized and identified in the Cambridge Crystallographic Database Centre [63], and more than 130.000 hypothetical MOFs have been generated by combination of building units [64], numbers that continue growing every year. MOFs are built from metal or metal-based clusters (nodes) linked by organic ligands (linkers) to form a three-dimensional structure (Figure 3) [62, 65–68]. Nodes usually involve transition metals [61, 69–72], while spacers are organic molecules containing a variety of functional groups such as carboxylate [66, 73], amine [74], or thiol [75]. The combination of different

Figure 3. Graphical representation of building units (left, nodes and linkers), and atomistic view of a sample MOF. Oxygen, nitrogen, cobalt, chlorine, carbon, and hidrogen atoms are depicted in red, dark blue, green, light blue, grey, and white, respectively.

nodes and linkers results in three dimensional well define structures with high pore volume and surface area, low density, high storage capacity, and a wide range of pore size [21, 76, 77]. The large diversity of nodes and organic ligands that can be included as well as the post-synthetic modification of the structures gives MOFs a huge degree of tunability [78]. This high tunability of MOFs allows a targeted control and design of structural features such as pore size and geometry, surface area, and surface chemistry for specific applications, which lead to unbeatable adsorptive and catalytic properties [79]. Among other applications, MOFs have been successfully used for hydrogen storage [77, 80], greenhouse gas capture [81, 82], capture and/or decomposition of harmful volatile chemicals [83–87], and many separation and purification processes with industrial and/or environmental interest [88–91].

However, stability of MOFs in many cases is an important drawback when comparing with other materials such as zeolites or activate carbons [21, 31, 65]. Some of them lose their crystallinity after synthesis and activation by the removal of solvent molecules. Adsorption of water or other guest molecules, such as ammonia, can also endanger the crystallinity of the structure by attacking exposed metallic centers [68, 92, 93]. Additionally, the structural flexibility is very important in this kind of materials [94]. Flexibility can be induced by the adsorption of guest molecules, the application of external forces, pressure

and/or temperature modifications, or interaction with light [94]. The most studied flexible behavior exhibited by MOFs materials are breathing [95], swelling [96], thermal expansion [97], linker rotation [98], and subnetwork displacement [99].

MOFs allow an almost inexhaustible source of possibilities. By finding the appropriate combination of elements one can obtain solids with cavities of predefined shapes, sizes, and surface chemistry. In this regard, molecular simulation plays a very important role as powerful tool to explore the properties of existing MOFs and to design new materials for specific applications [1, 2].

In Chapter 5 we focus on the 1647 MOF materials provided in the DDEC database with size pores big enough for the inclusion of CWA molecules [100]. As in the case of zeolites, a previously geometrical characterization of the pore space of each structure is performed. The water affinity and stability using is also studied using a high-throughput screening strategy based on the calculation of Henry's constants. This these materials in which water adsorption could compromise the ability of the materials for CWA protection are discarded.

1.3 HIGH-THROUGHPUT COMPUTATIONAL SCREENING

Given the wide range of possible materials, the key point for the capture and removal of targeted pollutants is the identification and/or design of the most suitable options and the application of the most favorable operation conditions (i.e. pressure and temperature). Molecular simulation plays a significant role in the development of the field, not only by explaining experimental results from a molecular point of view [101], but also by guiding future experiments testing huge amount of real and hypothetical materials and exploring operation conditions difficult to reproduce by experiments [102–104]. Computational work also avoids the experimental complications associated with toxic and/or corrosive compounds such as SO_2 or CWAs.

Computational high-throughput screening approaches (HTS) consist on large-scale testing materials taking advantage of low time-consuming simulation techniques [1, 64, 105]. The approach includes the exploration of real materials and the generation of new ones by combination of building blocks and chemical intuition. This generation process ends up in thousands of new opportunities impracticably to aboard experimentally. Instead of that, a low computational cost screening using Monte Carlo and Molecular Dynamic classical techniques is applied to efficiently identify the most promising candidates for a specific application in a relatively short period of time [106]. This way, HTS can significantly accelerate materials discovery when combined with experimental efforts. As starting point, molecular simulation is usually used to

rapidly obtain low coverage adsorption properties such as adsorption enthalpies, Henry's constants or heat of adsorptions for a wide range of candidate materials [87]. All these properties give useful information about low coverage interaction between the harmful gases of interest and the studied materials. However, an efficient identification of suitable materials needs to consider not only low coverage adsorption properties but also the adsorption capacity and selectivity at a temperature and/or pressure relevant for the separation process. Besides, Molecular dynamics (MD) simulations provide diffusion coefficients and other transport properties which are critical for the capture and separation process [1].

The purpose of this thesis is the application of molecular simulation techniques to the identification of materials for the selective capture of harmful gases from air. The adsorption and diffusion properties of these gases are studied in a wide range of materials and results reemphasize the need for considering both adsorption and diffusion processes in the selection of the optimal structures for a given separation process. A brief description of most important properties and the basis of the methodology used in this thesis can be found in the following sections. There are well-known and stablished methods that can are reviewed elsewhere [107].

1.4 FORCE FIELDS AND MODELS

In molecular simulations one needs to model the molecules, the structures, and their interactions. This section gives a general description of the force fields and models used in this thesis. A deeper description of particularities about them can be found on each chapter.

1.4.1 Force Fields

A force field is a set of functions and parameters that describes the interactions between the different components of a system. These interactions can be parameterized in a variety of analytical forms and the decision of how to model a system needs to be made based on the nature of the molecules and structures, as well as the properties under study. A wide variety of generic force fields can be found in the literature (e.g. the Universal Force Field, UFF [108]; CVFF [109]; Dreiding [110]; or OPLS [111]). However, the development of specific force fields is commonly necessary for particular systems. In this section the most common functional forms are described.

For a given system, the total potential energy can be obtained by the summation of the energy corresponding to bonded atoms (U_{bonded}) plus the energy corresponding to non-bonded atoms ($U_{non-bonded}$):

$$U_{total} = U_{bonded} + U_{nonbonded} \qquad (1.1)$$

The bonded term (U_{bonded}) defines the energy of the interactions between bonded atoms. In this part, interactions between two (bonding energy), three (bending energy), and four (torsion energy) consecutive atoms are considered. Figure 4 shows a representation of these energies:

$$U_{bonded} = U_{bond} + U_{bend} + U_{torsion} \quad (1.2)$$

Bond energy (U_{bond}) describes the change in energy as a bond between two atoms stretches or contracts. The most extended functional form to describe the bond energy is the harmonic potential:

$$U_{bond} = \frac{1}{2}k_{bond}(l - l_0)^2 \qquad (1.3)$$

where k_{bond} is the force constant, l is the interaction distance between the atoms, and l_0 is the equilibrium bond length.
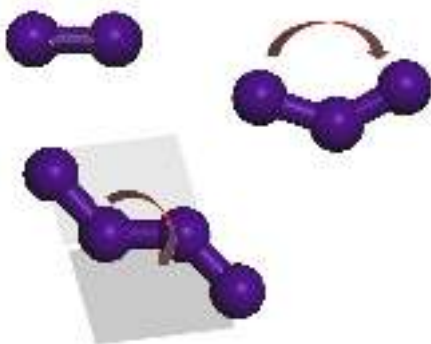
Figure 4. Schematic representation of the interatomic bonded interactions: bond stretching, angle bending, and torsion.

Bend energy (U_{bend}) describes the interaction between three neighboring atoms. The harmonic potential describes this interaction as follows:

$$U_{bend} = \frac{1}{2}k_{bend}(\Theta - \Theta_0)^2 \qquad (1.4)$$

where Θ is the measured bond angle, Θ_0 the equilibrium bond angle, and k_{bend} the force constant.

Torsion energy ($U_{torsion}$) is related to the dihedral angle of four consecutive atoms. Considering four bonded atoms, the dihedral angle is defined as the angle between the plane containing the first three atoms and the plane containing the last three atoms. Just as an example, the TraPPE dihedral potential describes this energy as:

$$\begin{aligned} U_{torsion} = &C_0 + C_1[1 + cos(\varphi)] + \\ &C_2[1 - cos(2\varphi)] + C_3[1 + cos(3\varphi)] \end{aligned}$$
$$(1.5)$$

where φ is the dihedral angle, and C_i are Fourier constants. In Chapter 5 of this thesis functionals forms different than TraPPE dihedral are used to describe the torsion energy for CWAs molecules. The full description of these potentials is include in a following section.

The non-bonded term ($U_{nonbonded}$) includes the energy from the interactions between non-bonded atoms, normally atoms of different molecules, atoms of the molecules with the atoms of the structures, and also atoms separated for more than four atoms in a given molecule.

It can be defined by a combination of van der Waals forces (U_{vdW}) and electrostatic interactions (U_{elec}).

$$U_{nonbonded} = U_{vdW} + U_{elec} \qquad (1.6)$$

Van der Waals interactions are often modeled by the Lennard-Jones potential [107]. The Lennard-Jones interatomic potential is a mathematical approach that allows to model the interaction between a pair of atoms or molecules subject to two different forces: an attractive force which acts at a long distance (van der Waals force) and a repulsive force at short distances (the repulsive force of Pauli) associated with the repulsion between the charge clouds overlap. The force is computed through two parameters: σ, which is the distance in which the potential is zero; and ε, which is the depth of the energy potential.

$$U_{vdW}(r_{ij}) = 4\varepsilon_{ij}\left[\left(\frac{\sigma_{ij}}{r_{ij}}\right)^{12} - \left(\frac{\sigma_{ij}}{r_{ij}}\right)^{6}\right] \quad (1.7)$$

where r_{ij} is the distance between two interacting particles and σ and ε are the Lennard-Jones parameters.

In general, the force field parameters are defined for the interactions of identical atoms while these for the interaction between different atoms are computed using generic mixing rules. Using the Lorentz-Berthelot mixing rules, the collision diameter (σ) is calculated by the arithmetic mean and the depth of the potential (ε)

by the geometric mean of the parameters of the involved atoms [112].

$$\sigma_{ij} = \frac{\sigma_{ii} + \sigma_{jj}}{2} \qquad (1.8)$$

$$\varepsilon_{ij} = \sqrt{\varepsilon_{ii}\varepsilon_{jj}} \qquad (1.9)$$

The electrostatic term (U_{elec}) accounts to the long-range interactions and is described according to a classical Coulombic potential:

$$U_{elec}(r_{ij}) = \frac{1}{4\pi\varepsilon_0\varepsilon_r}\frac{q_iq_j}{r_ir_j} \qquad (1.10)$$

where ε_r is the electric constant of the medium where the charges are placed, ε_0 is the permittivity in vacuum, q_i and q_j are the charges of the interacting atoms, and r_{ij} the distance between the atoms i and j. The Ewald summation method is used in this thesis to calculate the electrostatic energy in the periodic system [113].

Calculating the total energy of the system could lead to extremely time consuming and convergence problems due the huge amount of terms that need to be taken into account and the very long-range nature of the electrostatic interactions. For this reason, it is necessary to set a cut off distance for the potentials where they are cut and shifted to zero, so interactions longer than the cut off are omitted from the energy and force calculations. Alternatively, the potential can be truncated at the cut off distance. The energy correction due to this truncation, called tail correction, is then approximated and

added to the total energy. The truncation distance and whether to use tail correction or not should be considered on the description of each force field. Shifted potentials with a cut off distance of 12 Å are used in Chapters 2-4, while a truncated potential at a distance of 14 Å and the application of tails corrections are used in Chapter 5 for the description of CWAs molecules. The cut off distance also determines the amount of crystallographic unit cells that are used in simulations because the smallest perpendicular distance of the simulation cell has to be larger than twice the cut off.

Due to computational limitations, simulations are restricted to a few thousand atoms, a number that is still far from the thermodynamic limit. In order to extrapolate the obtained properties to a macroscopic system and to overcome problems of surface effects and long-time simulations, we employ periodic boundary conditions [107]. Using this, the simulation box is replicated in every direction of the space, and identical images of each particle are created at equivalent positions. Due to the application of boundary conditions and the cut off distance, the length of the simulations boxes in adsorption studies is usually about 20-40 Å.

1.4.2 Models for Zeolites and MOFs

The homogeneity in the composition and the structure of zeolites facilitates the development of transferable force fields for them. These materials consist of basic tetrahedral units made by oxygen and silicon, where silicon can be substituted in some zeolites by aluminum or other metallic atoms. Because of the different net charge of the substituted atoms, a negative net charge is generated in the system, which needs to be compensated by the addition of extra-framework cations, such as sodium or calcium. However, this thesis focuses on pure-silica zeolites. Regarding flexibility of these materials, it is well-established that it is generally reduced to atom vibrations and therefore, it does not affect their crystalline regularity. Hence, the effect of flexibility on the adsoprtion is usually negligible [114, 115]. It is for this reason that within this thesis the structure of the zeolitic frameworks is considered rigid and kept fixed during the simulation. The starting point is reported crystallographic position of the atoms of the dehydrated structures.

Generic and transferable force fields for zeolites, such as TraPPE-zeo force field [116], provides Lennard-Jones parameters and charges for the oxygen and silicon atoms, allowing the calculation of host-guest interaction parameters through the application of mixing rules. This aproach is used in Chapter 4. Unfortunately, for zeolites mixing rules not always perform well and the interactions parameters are usually refitted using experimental data to improve the obtained results. In these cases, is common to assume that the dis-

persive interaction of the atoms of the structure with the adsorbate is described by this of the oxygen atoms as the silicon atoms are placed in the center of the tetrahedron and surrounded by the oxygen atoms. This thesis uses this aproach in Chapters 2 and 3, taking the set of charges for the framework atoms from Garcia-Sanchez *et al.* [117].

The wide variety of centers and organic ligands in MOFs explains the lack of specific force fields to model host-guest interactions. Additionally, the weak nature of the metal-linker bond generally confers to MOFs materials a degree of flexibility much more important than in zeolites, showing some of them large structural changes that strongly affects adsorption and diffusion performance [94]. However, to computationally deal with this flexibility relies on the existence of experimental information about the specific flexible behavior of each framework and the development of a force field to reproduce this behavior. In addition, the use of these force fields strongly increases the computational time for the complexity. Due the lack of experimental evidences and to overcome extremely high time-consuming simulations [68], MOFs structures are commonly reproduced as rigid by using their most representative crystallographic positions. Experimentally reported structures included in the Cambridge Crystallographic Database Centre are used in this work, keeping the framework rigid during the simulations. Lennard-Jones and par-

tial charges, are assigned to each framework atom and Lorentz-Berthelot combining rules are usually applied to compute host-guest interactions. There are several generic force fields available in the literature for MOFs, but the most extended that is used in this thesis is a combination of parameters from Dreiding [110] and UFF [108] force fields.

1.4.3 Models for Harmful Gases and Water

The definition of adsorbate molecules in this thesis is made using classical models. For combustion gases (i.e. CO_2, CO, SO_2, NO_2 and N_2O_4), SF_6, and N_2 we use rigid full atom models. The description of a given molecule as rigid means that the model has no intramolecular contributions to energy (U_{bonded} = 0). This way, the molecule is inserted and deleted as one in the simulation box. The model used for CO_2 is inspired in that proposed by Harris and Yung [118]. This model has three interaction points with L-J parameters and charges centered at each atom. L-J parameters describing both gas-gas and gas-zeolite interaction are taken from Garcia-Sanchez *et al.* [117]. The model and parameters for CO were proposed by Martin-Calvo *et al.* [119]. This model includes one interaction center with L-J parameters and negative charge on each atom and an additional positive point charge with no mass in order to reproduce the experimental dipole moment of the molecule. SO_2

molecule is modeled with three interaction centers including both L-J parameters and point charges to mimic its dipole moment. The molecule-molecule interaction parameters are obtained in this thesis by fitting to the experimental vapor-liquid equilibrium (VLE). As explained above, zeolites not always obey mixing rules for the computation of molecule-zeolite interactions. Parameters for CO and SO_2 have been developed in this thesis by fitting computational results to experimental adsorption isotherms. N_2 molecule is modeled as proposed by Martin-Calvo *et al.* [120]. The model includes two L-J interaction centers with negative point charges (one on each nitrogen atom) that are offset by a positive charge at the center of mass of the molecule to reproduce the quadrupole moment of the molecule. Already reported parameters are used to reproduce the interactions of N_2 with oxygen atoms of the zeolite [121]. Sulfur hexafluoride is modeled with six non-charged L-J interaction centers (one on each fluorine atom) and an additional point with mass to mimic the sulfur atom in the center of the symmetric structure. As for SO_2, L-J parameters for sulfur hexafluoride were obtained by fitting to the experimental VLE and the interaction parameters with oxygen atoms of the zeolite are developed by fitting to experimental adsorption isotherms and heats of adsorption. In Chapter 4, NO_2 and its dimmer form (N_2O_4) are modeled according to models developed by Bourasseau *et al.* [122]. These models in-

clude three and six interaction centers, respectively, with L-J and point charges associated. For these molecules, interactions with zeolite atoms are calculate by mixing rules. The molecules of water are reproduced as rigid by using the well-known TIP4P model [123]. This model includes only one L-J interaction center in the oxygen atom and two positive charges on each hydrogen atom that are compensated with an additional negative charge moved off the oxygen and towards the hydrogens at a point (M) on the bisector of the HOH angle.

The use of rigid models is a good approximation for small gases as studied in Chapters 2-4. However, more complex molecules, such us CWAs, require to increase the accuracy of the models with a full description of bond lengths, angles, and torsions, including in this way the intramolecular energy (U_{bonded}) of the molecule. Flexible united atoms models for CWAs molecules and their simulants are used in Chapter 5. All these models describe each atom independently, as single interaction center with L-J and charges associated, except for CH_x groups which are considered as a single interaction center with its own effective potential (pseudo-atom). TraPPE force field was used for dimethyl methylphosphonate (DMMP), sarin, soman [124], and diethylsulfide (DES) [125]; while parameters for mustard gas were taken from Müller *et al.* [126] and these for diisopropylfluorophosphate (DIFP) from Vishnyakov *et*

al. [127]. The TraPPE force fields (sarim, soman, and DMMP) as well as Müller *et al.*(Mustard) use fixed bond lengths, while the Vishnyakov *et al.* force field (DIFP) uses a harmonic potential to model bond stretching. For all CWAs, a harmonic potential was used to describe angle bending. The description of fuctional forms for harmonic potentials is included in a previous subsection. Rotation about dihedral angles was controlled through a cosine series, including a phase angle term f to account for asymmetric rotational barriers:

$$
\begin{aligned}
U_{torsion} = & C_0 + C_1[1 + cos(\varphi + f)] + \\
& C_2[1 - cos(2\varphi + f)] + \\
& C_3[1 + cos(3\varphi + f)]
\end{aligned}
\tag{1.11}
$$

where φ is the dihedral angle, and C_i are Fourier constants. Additionally, a six-cosine dihedral is employed to describe the F-P-O-CH dihedral angle for DIFP.

$$
\begin{aligned}
U_{Tors} = & \sum_{n=0}^{5} C_n cos^n(\varphi) = C_0 - C_1 cos^1(\varphi) + \\
& C_2 cos^2(\varphi) - C_3 cos^3(\varphi) + \\
& C_4 cos^4(\varphi) - C_5 cos^5(\varphi)
\end{aligned}
\tag{1.12}
$$

Finally, the harmonic dihedral potentialc was used by Müller *et al.* to describe intramolecular rotations in the mustard gas molecule.

$$
U_{Tors} = \frac{1}{2} C_0 (\varphi - \tau)^2
\tag{1.13}
$$

A more detailed description of all used models is included on each chapter.

1.5   METHODS

Molecular simulation is nowadays an outstanding tool in many fields and a perfect complement for experimental techniques [103, 107, 112]. Simulations offer some advantages over experiments such as a microscopic point of view of the system, the possibility to study extreme conditions (i.e. pressure and/or temperature), or the exploration of wide hypothetical scenarios and theories such as the high-throughput screening (HTS) of a wide variety of materials, with low cost associated.

Before performing simulations one needs to think about the property that is going to study and how to describe the system. According to that, different methods might be selected. This work employs two classical methods: Monte Carlo and Molecular Dynamics. The basis of the main techniques used in this thesis are described below. More details about these methods can be found elsewhere [107].

1.5.1   Monte Carlo

Monte Carlo method (MC) is used to compute adsorption properties such as adsorption isotherms or isobars. This numerical statistical method approximates complex mathematical expressions that cannot be evaluated accurately. It is based on the use of random numbers and probabilities to calculate macroscopic properties. The Markov Chain Monte Carlo method based in the Metropolis (MCMC) algorithm is applied to systems in which the number of

accessible microstates is too large [128]. It allows the estimation of a macroscopic property without accounting for all the microstates. System configurations are generated with a probability proportional to their Boltzmann weight. It assumes that only the relative probability of visiting microstates of a system is needed instead of the absolute probability with the correct frequency [107].

A MC simulation is performed in cycles. During each cycle, a random move can be applied to a randomly selected molecule. Monte Carlo moves include rotation, regrow, insertiond and deletion, and identity change in the case of mixtures including two or more components, allowing a random molecule from one component to change its identity to become a molecule of another defined component.

Configurational Bias Monte Carlo

As the size of the modeled molecules increases the required computational time, the use of conventional Monte Carlo becomes too high time consuming due to the low efficiency of the insertions of molecules in the system. To improve the efficiency of the insertions and to avoid overlaps with the framework and other particles, Configurational Bias Monte Carlo method (CBMC) was developed [129]. Using the CBMC method, the molecule is inserted in the simulation box bead by bead. For each inserted bead k, trial orientations are generated according to the internal energy

(U^{int}). Then, the external energy (U^{ext}) of each trial position j of segment i is computed and the most favorable orientation is selected according this energy following the expression:

$$P_i(j) = \frac{exp\left(-\beta U_i^{ext}(j)\right)}{\sum_{i=1}^{k} exp\left(-\beta U_i^{ext}(j)\right)} = \frac{exp\left(-\beta U_i^{ext}(j)\right)}{\omega_i}$$

(1.14)

where $\beta = 1/(k_B T)$, k_B is the Boltzmann constant, T is the temperature and ω_i is the Rosenbluth weight.

When a trial orientation is selected, this is added to the chain and the procedure is repeated until the entire molecule is grown. For the newly grown molecule the acceptance or rejection is calculated based on the Rosenbluth factor of the new configuration [130]:

$$W^{new} = \prod_i \omega_i$$

(1.15)

Continuous Fractional Monte Carlo

In open systems where the number of molecules varies, the insertion probability of the molecules becomes very low at high densities. The insertion can be improved in this case by using the Continuous Fractional Component Monte Carlo method (CFCMC) [131]. The system is expanded with an additional fractional particle with scaled interactions using a parameter λ that ranges from 0 to 1. Only the inter-molecular energy of the molecule is

scaled, being inflated and deflate like a balloon. Instead of inserting a new molecule, a trial change in λ is attempted using $\lambda(n) = \lambda(o) + \Delta\lambda$.

In some systems changes in λ are hard to obtain. To prevent the system from getting stuck, an additional bias η on λ can be used, where each λ has an associated biasing factor η that needs to be calibrated in the system. This bias does not affect the outcome as it is later compensated by the acceptance rules. There are three possible outcomes of a change from $\lambda(o)$ to $\lambda(n)$:

- $\lambda(n)$ remains between 0 and 1. The inter-molecular energy of the particle with the new $\lambda(n)$ is computed and compared to the old energy. There is no change in the number or position of the particles.

- $\lambda(n)$ becomes larger than 1. When λ exceeds unity, $\lambda(n) = 1 + \varepsilon$, the current fractional molecule is fully inserted ($\lambda = 1$) and an additional particle is randomly generated with $\lambda = \varepsilon$.

- $\lambda(n)$ becomes smaller than 0. When λ falls below 0, $\lambda(n) = -\varepsilon$, the current fractional molecule is deleted ($\lambda = 0$) and a new molecule from the sytem is chosen with a new $\lambda = 1 - \varepsilon$.

A downside of CFCMC compared to CBMC is that it takes longer to equilibrate at low density. However, it is possible to combine CFCMC and CBMC schemes, performing insertion ($\lambda = 1$) and deletion ($\lambda = 0$) moves using configurational biasing [132].

1.5.2 Reactive Monte Carlo

To compute the equilibrium properties of chemically reacting or associating systems, the reactive Monte Carlo (RxMC) is used. The RxMC algorithm samples reactions directly, without going through the transition states. [133, 134] Therefore, only equilibrium properties can be computed. RxMC simulations provide equilibrium concentrations for each specie, and relevant thermodynamic properties such as the density, pressure and energy, in addition to fluid structure. For this purpose, the stoichiometry of the reactions needs to be specified. The method does not require a reactive potential that mimics bond breaking or forming. It only requires ideal-gas free energy information for the reacting species and a description of the relevant intermolecular forces. Essentially, the method introduces in the GCMC a "forward" and "backward" reaction step, which ensures that the chemical reaction equilibria between the reactants and the products is maintained. For a chemical reaction at equilibrium in a single- or a two-component system, the stoichiometric coefficient (v_i) of each component (i) times the chemical potential of each component (μ_i) must be zero:

$$\sum_i v_i \mu_i = 0 \qquad (1.16)$$

The forward and reverse reaction steps

are combinations of particle creation and destruction moves that must be chosen with equal probability in order to maintain microscopic reversibility in the system [135]. In this thesis the RxMC method is used to study the effect of confinement in the N_2O_4-NO_2 reaction system (Chapter 4). Using as example this reaction (i.e $N_2O_4 \longleftrightarrow 2\ NO_2$), the forward move removes one molecule of N_2O_4 from the system and inserts $2\ NO_2$. The backward move removes 2 molecule of NO_2 molecules and inserts one of N_2O_4. Details about acceptance rules for the movements can be found elsewhere [136].

The RxMC method is compatible with the canonical, grand canonical, isothermal-isobaric, Gibbs and some other ensembles. It has also been combined with CBMC and CFMC methods and MD. The RxMC in the isothermal-isobaric ensemble is used in this thesis to validate the partition fuctions calculated by reproducing experimental equilibrium bulk phase mole fractions of each species and reaction constants at different temperautes. The reaction inside the pores of zeolites is also studied using RxMC simulations in the grand canonical and the Gibbs ensembles. Results from both methods are compared to ensure that both lead to the same results. This allows the use of reactive GCMC simulations taking advantage of its lower computational cost in comparison to Gibbs aproach. The highest cost of the later is related to the necessity of simulating both bulk and pore phases simul-

taneously [137]. This requirement can be omited with GCMC simulations for what the composition of the reservoir phase at equilibrium is obtained from the previous isothermal-isobaric simulations.

A full explanation of the RxMC method and its applications can be found in the new edition of Allen and Tildesley [112].

1.5.3 Molecular Dynamics

Molecular dynamics (MD) is a simulation method that predicts the evolution of the system and its properties over time. Successive configurations of the system are generated, in which the position, velocity, trajectories, and acceleration of the atoms are calculated using Newton's laws of motion. The velocity-Verlet algorithm is the most common method to integrate the equations of motion [107].

From an initial configuration of the particles of a given system, MD simulations calculate forces and generates new velocities and positions. On each time step successive configurations are generated obtaining the trajectories of the particles from which average properties of the system can be obtained. The starting configuration is usually obtained by performing a previous MC simulation. Then the MD simulation itself is performed up to equilibrate the system, and after that one can start collect information about the property of interest.

1.6   ADSORPTION AND
DIFFUSION PROPERTIES

This thesis contains the calculation of a variety of adsorption and diffusion properties. Together with the adecuate method, a suitable statistical ensemble must be selected according to the property of interest. A statistical ensemble is a probability distribution for the state of the system and refers to a collection of systems that share common macroscopic properties. This way, different macroscopic constraints lead to different types of ensembles, with particular statistical characteristics. This section contains a brief description of the most important properties and associated statistical ensemble included in this thesis.

Vapor-liquid coexistence curve

The vapor liquid equilibrium (VLE) curve can be modeled using Gibbs ensemble Monte Carlo simulations [107]. In these simulations there are two microscopic regions (two simulation boxes) within the bulk phases away from the interface. Temperature, total number of molecules, and total volume remain constant during the simulation and both regions should be in internal equilibrium. The use of different Monte Carlo moves allows the satisfaction of the phase coexistence requirements. The internal equilibrium of each region is ensured by the displacement of the particles between cages (satisfying equality of chemical potential), while volume fluctu-

ations in the simulation boxes keeps the equality of pressure.

The calculation of the VLE is the first step in most simulation studies as it allows to obtain the interaction parameters for gas intermolecular interactions. They are commonly obtained by fitting computed data to the experimental vapor-liquid equilibrium curve. This methodology is used here to develop intermolecular interaction parameters for SO_2 and SF_6 molecules.

Adsorption loading

Adsorption isotherms are obtained by using Monte Carlo simulations in the grand-canonical ensemble (GCMC) [107]. In this ensemble the chemical potential (μ), the volume (V), and the temperature (T) remain fixed. The Grand-canonical ensemble represents an open system that can exchange both heat and mass with the surroundings. Consequently, the equilibrium temperature and the chemical potential should be specified to define the state of the system. This ensemble is commonly employed to obtain adsorption properties such as adsorption isotherms. During simulations, molecules are added or removed from the system to a connected reservoir with the same chemical potential and temperature. The average number of molecules adsorbed in the structure (N) can be obtained during the simulation giving useful information about the adsorption capacity of the material.

For adsorption isotherms, it is common to study the number of adsorbed particles at certain conditions of temperate, volume, and pressure instead of using chemical potential directly. The adsorbed quantity can also be studied at a fixed pressure and different temperatures (adsorption isobars). For these purposes, the pressure p can be fixed in the simulations through the fugacity f as:

$$p = \phi f \qquad (1.17)$$

where ϕ is the fugacity coefficient obtained from the equation of state of the vapor in the reservoir. For ideal or real gaes below one bar of pressure, it is possible to assume fugacity as pressure ($\phi = 1$). Following this strategy, the chemical potential is computed using the fugacity:

$$\mu = \mu^0 + RTln\left(\frac{f}{f_0}\right) \qquad (1.18)$$

where f_0 is the standard fugacity, μ_0 is the standard chemical potential, R is the ideal gas constant, and T is the temperature of the system.

From GCMC simulations we obtain the total amount of molecules located inside the pores of the structure (absolute adsorption). In order to compare with experimental measurements, molecules that are in the pores without gas-solid interactions need to be excluded (excess adsorption). The conversion between absolute and excess adsorption is done according to the following expression [138, 139]:

$$n_{exc} = n_{abs} - V^g \rho^g \qquad (1.19)$$

where V^g is the pore volume of the adsorbent and ρ^g is the molar density of the bulk gas phase. The value of the pore volume can be obtained experimentally or by simulation measuring helium adsorption [138].

Along this thesis GCMC simulations are performed to study the adsoprtion capacity of zeolites (Chapters 2-4) and MOFs (Chapter 5) at specific conditions of pressure and temperaute. Additionally, in Chapters 2 and 3 GCMC is used to develop gas-zeolite L-J interaction parameters by fitting experimental and computed adsoprtion isotherms for SO_2, CO, and SF_6.

Henry coefficients and heats and entropies of adsorption

Henry coefficients (K_H) and heats of adsorption (Q_{st}) provide information about the strength of the adsorbate-adsorbent interaction. These adsorption properties are temperature-dependent and are usually obtained in the low-coverage regime. K_H and Q_{st} can be obtained using the Widom test particle insertion method [140] and MC simulations in the canonical ensemble (NVT).

In the canonical ensemble the number of particles *(N)*, the temperature *(T)*, and the volume *(V)*, remains constant. As a consequence, the equilibrium temperature T defines the state of the system. It can be represented as a closed system that can

exchange heat but not particles with the surroundings.

The Widom test particle insertion method [140] consists in the insertion of a "ghost" molecule in the system and the computation of its energy and Rosenbluth factor, deleting it afterwards. With successive insertions, the whole system can be sampled without affecting it.

Henry coefficients are related to the excess free energy (F, or excess chemical potential) of the guest molecule and both can be obtained from the Rosenbluth factor as follows:

$$K_H = \frac{1}{RT\rho} \frac{<W>}{<W^{IG}>} \quad (1.20)$$

$$F = -RTln\frac{<W>}{<W^{IG}>} \quad (1.21)$$

where R is the ideal gas constant, T is the temperature of the system, ρ is the density of the adsorbent, $<W>$ is the average Rosenbluth factor of a single molecule in the system and $<W^{IG}>$ is the average Rosenbluth factor of the molecule in the ideal gas [107].

The isosteric heat of adsorption is calculated from the average energies sampled of the system:

$$Q_{st} = \Delta H = \Delta U - RT =$$
$$\left(<U_{hg}> - <U_h> - <U_g>\right) - (RT) \quad (1.22)$$

where $<U_{hg}>$ is the host-guest average energy, $<U_h>$ is the average potential energy of the host, and $<U_g>$ is the potential energy of an isolated single molecule.

Finally, it is possible to calculate the entropy (ΔS) following the expression:

$$\Delta F = \Delta U - T\Delta S \quad (1.23)$$

The above mentioned energies need to be obtained from two separated simulations. First, one simulation is required to obtain the potential energy of an isolated single molecule. Finally, we run other simulation to obtain the average energy of the molecule inside the structure.

The Widom test particle insertion method in combination with CMC simulations has been used along this thesis to evaluted the strength of gas-material interactions in the low regimen. In Chapter 2 and 3 the adsorption selectivity of a wide range of zeolitic materials for SO_2/CO_2 and SF_6/N_2 separations is analyzed using the ratio of Henry's constants and heats of adsorption for each molecule. These properties are also used in Chapter 3 to validate developed LJ parameters for SF_6-zeolite interaction by comparing calculated and already published experimental heats of adsorption in MFI zeolite. In Chapter 5 Henry's constants and heats of adsorption are calculated for more than 1600 MOFs materials. These properties not only provides useful information about CWAs-MOFs interaction but also give support to experimental use of simulants instead of theirs more toxic counterparts and efficiently screen the database of MOFs looking for hydrophobic candidates that minimize water competition.

Diffusion coefficients

Diffusivity of guest molecules through the host system can be obtained using MD simulations. As explained above, the NVT ensemble can be used in combination with MD simulations to obtain diffusion coefficients. The isobaric-isothermal ensemble (NPT) can also be used to describe systems with variable volume, allowing a variation of this property while keeping fixed the number of particles *(N)* and the temperature *(T)*. This ensemble represents a closed system with fixed pressure *(P)*.

Self-diffusion describes the diffusive motion of a single particle. In an equilibrium MD simulation, a separation of time scales occurs for interacting particles [141]. At very short time the mean square displacement (MSD) shows a quadratic dependence on time, what is known as the ballistic regime. In a intermediate regime, particles colide with other particles due to confinement. The diffusional regime is reached when particles are able to escape from the local environment and explore the full periodic lattice. In this regime the MSD becomes linear with time (a slope of 1 on a log-log plot). The self-diffusion coefficient (D_S) is obtained from the slope of the MSD in the diffusional regimen at long time, as follows:

$$D_S^\alpha = \frac{1}{2N} \lim_{t \to \infty} \frac{d}{dt} < \sum_{i=1}^{N} (r_{i\alpha}(t) - r_{i\alpha}(t_0))^2 >$$

(1.24)

where N is the number of molecules, t is

the time, and $r_{i\alpha}$ is the α-component of the position of molecule i. Equation (1.24) is known as the Einstein equation.

The diffusion coefficients in the $x-$, $y-$, and $z-$ directions (D_S^x, D_S^y, D_S^z) are averaged to obtain the self-diffusion coefficient (D_S):

$$D_S = \frac{D_S^x + D_S^y + D_S^z}{3}$$

(1.25)

In this thesis MD simulations are performed to obtain self-diffusion coefficients for small harmful gases molecules in a wide variety of zeolites. These coefficients are used to discard materials in which the diffusion of the studied gases is poor or not allowed and to identify and properly block experimental non-accesible fractions of the pore space of some frameworks in which molecules could be wrongly inserted during MC simulations.

1.7   OUTLINE OF THE THESIS

In this thesis molecular simulations are used for the study of the capture and removal of several gases with environmental relevance using nanoporous materials as molecular sieves. Adsorption and diffusion properties are calculated to predict the performance of real or hypothetical materials, providing insights of the microscopic process. The suitability of zeolites and MOFs as adsorbents is analyzed. These are two families of nanoporous materials with desirable properties that make them promising materials for the storage, separation, and purification of gas mixtures.

This thesis is divided into three blocks covering the use of zeolites for the adsorption of small gases containing sulfur, and nitrogen, and the use of MOFs for the capture of biomolecules. General methods and models employed in all these studies are described in previous sections and specific developed force fields parameters are defined in the chapter in which each issue is tackled.

Effect of zeolite topology on adsorption and separation processes of sulfur compounds pollutants (Chapters 2 and 3)

In Chapters 2 and 3 the effect of zeolite topology on the capture and separation of sulfur compounds with environmental relevance is investigated at molecular level. A wide variety of zeolites are screened, considering not only low coverage and adsorption capacities, but also diffusion properties, selectivity, and so forth the optimal temperature and/or pressure for an efficient separation process.

The capture and separation of sulfur dioxide (SO_2) from mixtures containing carbon dioxide and carbon monoxide is studied in Chapter 2, while Chapter 3 deals with the separation of the greenhouse gas sulfur hexafluoride (SF_6) from industrial mixtures containing nitrogen. Besides adsorption and diffusion analyses, interaction force field parameters between zeolites and both sulfur compounds are proposed.

Effect of confinement in an equilibrium chemical reaction containing nitrogen compounds pollutants (Chapter 4)

Chapter 4 provides insights to understand the effect of zeolite topology on the nitrogen dioxide-dinitrogen tetroxide (NO_2-N_2O_4) equilibrium reacting mixture. The performance of the reaction in the bulk phase and inside the pores of the zeolites at different conditions of pressure and temperature is successfully described by adsorption isotherms and isobars.

Selective chemical warfare agents capture using MOFs (Chapter 5)

This Chapter provides a high-through molecular simulation screening to explore the suitability of MOF structures for chemical warfare agents (CWA) protection. Low regimen adsorption properties (Henry's constants and heats of adsorption) are used to select promising materials for the capture of sarin, soman, mustard gas, and their simulants in presence of water. After a new selection of materials based on their water affinity, their storage capacity is also identified. The screening is completed by successfully synthesizing and testing one of the top structures.

Chapter 6 compiles the specific conclusions obtained from each chapter and the general conclusions of this thesis.

1.8 Bibliography

[1] Colon, Y. J.; Snurr, R. Q. *Chemical Society Reviews* **2014**, *43*, 5735–5749.

[2] Moghadam, P. Z.; Islamoglu, T.; Goswami, S.; Exley, J.; Fantham, M.; Kaminski, C. F.; Snurr, R. Q.; Farha, O. K.; Fairen-Jimenez, D. *Nature Communications* **2018**, *9*, 1378.

[3] Landon, S. M. *International Geology Review* **2002**, *44*, 1105–1114.

[4] Lin, Y.; Kong, C.; Zhang, Q.; Chen, L. *Advanced Energy Materials* **2017**, *7*.

[5] Chu, S. *Science* **2009**, *325*, 1599.

[6] Haszeldine, R. S. *Science* **2009**, *325*, 1647–1652.

[7] Son, B.; Yang, W.; Breysse, P.; Chung, T.; Lee, Y. *Environmental Research* **2004**, *94*, 291–296.

[8] Das, A. K.; Wilde, J. D.; Heynderickx, G. J.; Marin, G. B. *Aiche Journal* **2001**, *47*, 2831–2844.

[9] de Visser, E.; Hendriks, C.; Barrio, M.; Mølnvik, M. J.; de Koeijer, G.; Liljemark, S.; Le Gallo, Y. *International Journal of Greenhouse Gas Control* **2008**, *2*, 478–484.

[10] Ding, L. F.; Yazaydin, A. O. *Journal of Physical Chemistry C* **2012**, *116*, 22987–22991.

[11] Yu, C.-H.; Huang, C.-H.; Tan, C.-S. *Aerosol and Air Quality Research* **2012**, *12*, 745–769.

[12] Iyer, M. V.; Gupta, H.; Sakadjian, B. B.; Fan, L.-S. *Industrial & Engineering Chemistry Research* **2004**, *43*, 3939–3947.

[13] Hartman, M.; Trnka, O. *AIChE Journal* **1993**, *39*, 615–624.

[14] Rao, A. B.; Rubin, E. S. *Environmental Science & Technology* **2002**, *36*, 4467–4475.

[15] Singh, D.; Croiset, E.; Douglas, P. L.; Douglas, M. A. *Energy Conversion and Management* **2003**, *44*, 3073–3091.

[16] Cha, I.; Lee, S.; Lee, J. D.; Lee, G.-W.; Seo, Y. *Environmental Science & Technology* **2010**, *44*, 6117–6122.

[17] Houghton, J. T.; Meira Filho, L. G.; Callander, B. A.; Harris, N.; Kattenberg, A.; Maskell, K. In *Intergovernmental Panel on Climate Change (IPCC)*; Press, C. U., Ed.; Cambridge University Press: Cambridge, U. K., 1996; pp 23–28.

[18] Builes, S.; Roussel, T.; Vega, L. F. *AIChE Journal* **2011**, *57*, 962–974.

[19] Zhang, J.; Zhou, J. Z.; Liu, Q.; Qian, G.; Xu, Z. P. *Environmental science & technology* **2013**, *47*, 6493–6499.

[20] Rigby, M. et al. *Atmospheric Chemistry and Physics* **2010**, *10*, 10305–10320.

[21] Decoste, J. B.; Peterson, G. W. *Chemical Reviews* **2014**, *114*, 5695–5727.

[22] Enserink, M. *Science* **2013**, *341*, 1050 – 1051.

[23] Geraci, M. J. *Annals of Pharmacotherapy* **2008**, *42*, 237–246.

[24] Szinicz, L. *Toxicology* **2005**, *214*, 167–181.

[25] Rochelle, G. T. *Science* **2009**, *325*, 1652–1654.

[26] Tobiesen, F. A.; Svendsen, H. F.; Hoff, K. A. *International Journal of Green Energy* **2005**, *2*, 201–215.

[27] Ma, X.; Wang, X.; Song, C. *Journal of American Chemical Society* **2009**, 5777–5783.

[28] Saravanamurugan, S.; Kunov-kruse, A. J.; Fehrmann, R.; Riisager, A. *ChemSusChem* **2014**, *7*, 897–902.

[29] Tsai, C.-H.; Shao, J.-M. *Journal of Hazardous Materials* **2008**, *157*, 201–206.

[30] Liu, Y.; Howarth, A. J.; Vermeulen, N. A.; Moon, S. Y.; Hupp, J. T.; Farha, O. K. *Coordination Chemistry Reviews* **2017**, *346*, 101–111.

[31] Bobbitt, N. S.; Mendonca, M. L.; Howarth, A. J.; Islamoglu, T.; Hupp, J. T.; Farha, O. K.; Snurr, R. Q. *Chem. Soc. Rev.* **2017**, *46*, 3357–3385.

[32] Srivastava, R. K.; Jozewicz, W.; Singer, C. *Environmental Progress* **2001**, *20*, 219–228.

[33] Forzatti, P.; Lietti, L. *Heterogeneous Chemistry Reviews* **1996**, *3*, 33–51.

[34] Shelef, M. *Chemical Reviews* **1995**, *95*, 209–225.

[35] Song, X.; Liu, X.; Ye, Z.; He, J.; Zhang, R.; Hou, H. *Journal of Hazardous Materials* **2009**, *168*, 493–500.

[36] Ben-Mansour, R.; Habib, M. A.; Bamidele, O. E.; Basha, M.; Qasem, N. A. A.; Peedikakkal, A.; Laoui, T.; Ali, M. *Applied Energy* **2016**, *161*, 225–255.

[37] Wu, Z.; Zhao, D. *Chemical Communications* **2011**, *47*, 3332–3338.

[38] Zhao, L.; Bacsik, Z.; Hedin, N.; Wei, W.; Sun, Y.; Antonietti, M.; Titirici, M.-M. *ChemSusChem* **2010**, *3*, 840–845.

[39] Cavenati, S.; Grande, C. A.; Rodrigues, A. E. *Chemical Engineering Science* **2006**, *61*, 3893–3906.

[40] Ghoufi, A.; Gaberova, L.; Rouquerol, J.; Vincent, D.; Llewellyn, P. L.; Maurin, G. *Microporous and Mesoporous Materials* **2009**, *119*, 117–128.

[41] Jasuja, H.; Peterson, G. W.; Decoste, J. B.; Browe, M. A.; Walton, K. S. *Chemical Engineering Science* **2015**, *124*, 118–124.

[42] Kim, K. C. *Journal of Organometallic Chemistry* **2018**, *854*, 94–105.

[43] Rieth, A. J.; Dinca, M. *Journal of the American Chemical Society* **2018**, *140*, 3461–3466.

[44] Deng, H.; Yi, H.; Tang, X.; Yu, Q.; Ning, P.; Yang, L. *Chemical Engineering Journal* **2012**, *188*, 77–85.

[45] Liu, Y.; Bisson, T. M.; Yang, H.; Xu, Z. *Fuel Processing Technology* **2010**, *91*, 1175–1197.

[46] Lin, Z.-E.; Zhang, J.; Yang, G.-Y. *Inorganic Chemistry* **2003**, *42*, 1797–1799.

[47] Gómez, J. M.; Ovejero, G.; Romero, M. D. No Title. Ph.D. thesis, 2005.

[48] García Martínez, J. Sńtesis y caracterización de zeolitas y materiales compuestos zeolita/carbń. Aplicaciones para la eliminaćin de SO$_2$. Ph.D. thesis, 2000.

[49] Loewenstein, W. *American Mineralogist: Journal of Earth and Planetary Materials* **1954**, *39*, 92–96.

[50] Baerlocher, C.; McCusker, L. B.; Olson, D. *Atlas of Ze-*

olite Framework types, 6th ed.; Elsevier: London, 2007.

[51] Romero, M. D.; Ovejero, G.; Rodríguez, A.; Gómez, J. M. *Microporous and Mesoporous Materials* **2005**, *81*, 313–320.

[52] Altshuler, G. N.; Shkurenko, G. Y. *Bulletin of the Academy of Sciences of the USSR Division of Chemical Science* **1990**, *39*, 1331.

[53] Anerousis, J. P. *Chemical Engineering* **1976**, *83*, 128.

[54] Bernal, M. P.; Coronas, J.; Menendez, M.; Santamaria, J. *AIChE Journal* **2004**, *50*, 127–135.

[55] Chambellan, A.; Chevreau, T.; Khabtou, S.; Marzin, M.; Lavalley, J. C. *Zeolites* **1992**, *12*, 306–314.

[56] Querol, X.; Alastuey, A.; Moreno, N.; Alvarez-Ayuso, E.; Garcia-Sanchez, A.; Cama, J.; Ayora, C.; Simon, M. *Chemosphere* **2006**, *62*, 171–180.

[57] Aguilar, J.; Dorronsoro, C.; Fernandez, E.; Fernandez, J.; Garcia, I.; Martin, F.; Simon, M. *Water Air and Soil Pollution* **2004**, *151*, 323–333.

[58] Cama, J.; Ayora, C.; Querol, X.; Moreno, N. *Journal of Environmental Engineering-Asce* **2005**, *131*, 1052–1056.

[59] Zhang, X. Y.; Shen, Q.; He, C.; Ma, C. Y.; Cheng, J.; Hao, Z. P. *Catalysis Communications* **2012**, *18*, 151–155.

[60] Willems, T. F.; Rycroft, C. H.; Kazi, M.; Meza, J. C.; Haranczyk, M. *Microporous and Mesoporous Materials* **2012**, *149*, 134–141.

[61] Li, H.; Eddaoudi, M.; O'Keeffe, M.; Yaghi, O. M. *Nature* **1999**, *402*, 276–279.

[62] Zhou, H. C.; Long, J. R.; Yaghi, O. M. *Chemical Reviews* **2012**, *112*, 673–674.

[63] Moghadam, P. Z.; Li, A.; Wiggin, S. B.; Tao, A.; Maloney, A. G. P.; Wood, P. A.; Ward, S. C.; Fairen-Jimenez, D. *Chemistry of Materials* **2017**, *29*, 2618–2625.

[64] Wilmer, C. E.; Leaf, M.; Lee, C. Y.; Farha, O. K.; Hauser, B. G.; Hupp, J. T.; Snurr, R. Q. *Nature Chemistry* **2012**, *4*, 83–89.

[65] Kitagawa, S.; Kitaura, R.; Noro, S.-i. *Angewandte Chemie - International Edition* **2004**, *43*, 2334–2375.

[66] Eddaoudi, M.; Kim, J.; Rosi, N.; Yaghi, O. M. *Science* **2002**, *295*, 469–472.

[67] Furukawa, H.; Cordova, K.; O'Keeffe, M.; Yaghi, O. *Science* **2013**, *341*, 974.

[68] Meek, S. T.; Greathouse, J. A.; Allendorf, M. D. *Advanced Materials* **2011**, *23*, 249–267.

[69] Dybtsev, D. N.; Chun, H.; Yoon, S. H.; Kim, D.; Kim, K. *Journal of the American Chemical Society* **2004**, *126*, 32–33.

[70] Fletcher, A. J.; Cussen, E. J.; Prior, T. J.; Rosseinsky, M. J.; Kepert, C. J.; Thomas, K. M. *Journal of the American Chemical Society* **2001**, *123*, 10001–10011.

[71] Bourrelly, S.; Llewellyn, P. L.; Serre, C.; Millange, F.; Loiseau, T.; Férey, G. *Journal of the American Chemical Society* **2005**, *127*, 13519–13521.

[72] Millward, A. R.; Yaghi, O. M. *Journal of the American Chemical Society* **2005**, *127*, 17998–17999.

[73] Vishnyakov, A.; Ravikovitch, P. I.; Neimark, A. V.; Bu, M.; Wang, Q. M. *Nano Lett.* **2003**, *3*, 713–718.

[74] Banerjee, R.; Phan, A.; Wang, B.; Knobler, C.; Furukawa, H.; O'Keeffe, M.; Yaghi, O. M. *Science* **2008**, *319*, 939–943.

[75] Matlock, M. M.; Howerton, B. S.; Henke, K. R.; Atwood, D. A. *Journal of Hazardous Materials* **2001**, *82*, 55–63.

[76] Rowsell, J. L.; Yaghi, O. M. *Microporous and Mesoporous Materials* **2004**, *73*, 3–14.

[77] Rowsell, J. L.; Yaghi, O. M. *Angewandte Chemie - International Edition* **2005**, *44*, 4670–4679.

[78] Tanabe, K. K.; Cohen, S. M. *Chemical Society Reviews* **2011**, *40*, 498–519.

[79] Britt, D.; Furukawa, H.; Wang, B.; Glover, T. G.; Yaghi, O. M. *Proceedings of the National Academy of Sciences of the United States of America* **2009**, *106*, 20637–20640.

[80] Panella, B.; Hirscher, M. *Advanced Materials* **2005**, *17*, 538–541.

[81] Sumida, K.; Rogow, D. L.; Mason, J. A.; McDonald, T. M.; Bloch, E. D.; Herm, Z. R.; Bae, T.-H.; Long, J. R. *Chemical Reviews* **2012**, *112*, 724–781.

[82] Chaemchuen, S.; Kabir, N. A.; Zhou, K.; Verpoort, F. *Chemical Society Reviews* **2013**, *42*, 9304–9332.

[83] Grant Glover, T.; Peterson, G. W.; Schindler, B. J.; Britt, D.; Yaghi, O. *Chemical Engineering Science* **2011**, *66*, 163–170.

[84] Britt, D.; Tranchemontagne, D.; Yaghi, O. M. *Proceedings of the National Academy of Sciences of the United States of America* **2008**, *105*, 11623–11627.

[85] Kim, K. C.; Moghadam, P. Z.; Fairen-Jimenez, D.; Snurr, R. Q. *Industrial & Engineering Chemistry Research* **2015**, *54*, 3257–3267.

[86] Ghosh, P.; Kim, K. C.; Snurr, R. Q. *Journal of Physical Chemistry C* **2014**, *118*, 1102–1110.

[87] Moghadam, P. Z.; Fairen-Jimenez, D.; Snurr, R. Q. *J. Mater. Chem. A* **2015**, *4*, 529–536.

[88] Snurr, R. Q.; Hupp, J. T.; Nguyen, S. B. T. *AIChE Journal* **2004**, *50*, 1090–1095.

[89] Lee, J. Y.; Olson, D. H.; Pan, L.; Emge, T. J.; Li, J. *Advanced Functional Materials* **2007**, *17*, 1255–1262.

[90] Keskin, S.; Sholl, D. S. *Journal of Physical Chemistry C* **2007**, *111*, 14055–14059.

[91] Van de Voorde, B.; Bueken, B.; Denayer, J.; De Vos, D. *Chemical Society reviews* **2014**, *43*, 5766–88.

[92] Canivet, J.; Fateeva, A.; Guo, Y.; Coasne, B.; Farrusseng, D. *Chemical Society reviews* **2014**, 5594–5617.

[93] Gul-E-Noor, F.; Jee, B.; Pöppl, A.; Hartmann, M.; Himsl, D.; Bertmer, M. *Physical Chemistry Chemical Physics* **2011**, *13*, 7783–7788.

[94] Schneemann, A.; Bon, V.; Schwedler, I.; Senkovska, I.; Kaskel, S.; Fischer, R. A. *Chemical Society Reviews* **2014**, *43*, 6062–6096.

[95] Millange, F.; Guillou, N.; Walton, R. I.; Grenèche, J. M.; Margiolaki, I.; Férey, G. *Chemical*

Communications **2008**, 4732–4734.

[96] Surblé, S.; Serre, C.; Mellot-Draznieks, C.; Millange, F.; Férey, G. *Chemical Communications* **2006**, 284–286.

[97] Dubbeldam, D.; Walton, K. S.; Ellis, D. E.; Snurr, R. Q. *Angewandte Chemie - International Edition* **2007**, *46*, 4496–4499.

[98] Fairen-Jimenez, D.; Galvelis, R.; Torrisi, A.; Gellan, A. D.; Wharmby, M. T.; Wright, P. A.; Mellot-Draznieks, C.; Düren, T. *Dalton Transactions* **2012**, *41*, 10752–10762.

[99] Maji, T. K.; Matsuda, R.; Kitagawa, S. *Nature Materials* **2007**, *6*, 142–148.

[100] Nazarian, D.; Camp, J. S.; Sholl, D. S. *Chemistry of Materials* **2016**, *28*, 785–793.

[101] Lee, J. S.; Vlaisavljevich, B.; Britt, D. K.; Brown, C. M.; Haranczyk, M.; Neaton, J. B.; Smit, B.; Long, J. R.; Queen, W. L. *Advanced Materials* **2015**, *27*, 5785–5796.

[102] Sun, W.; Lin, L.; Peng, C.; Smit, B. *AIChE Journal* **2014**, *60*, 2314–2323.

[103] Lin, L.-C.; Berger, A. H.; Martin, R. L.; Kim, J.; Swisher, J. A.; Jariwala, K.; Rycroft, C. H.; Bhown, A. S.; Deem, M.; Haranczyk, M.; Smit, B. *Nature Materials* **2012**, *11*, 633–641.

[104] Bernales, V.; League, A. B.; Li, Z.; Schweitzer, N. M.; Peters, A. W.; Carlson, K.; Hupp, J. T.; Cramer, C. J.; Farha, O. K.; Gagliardi, L. *J. Phys. Chem. C* **2016**, *120*, 23576–23583.

[105] Witman, M.; Ling, S.; Anderson, S.; Tong, L.; Stylianou, K. C.; Slater, B.; Smit, B.; Haranczyk, M. *Chemical Science* **2016**, *10*, 6263–6272.

[106] Borboudakis, G.; Stergiannakos, T.; Frysali, M.; Klontzas, E.; Tsamardinos, I.; Froudakis, G. E. *npj Computational Materials* **2017**, *3*, 1–6.

[107] Frenkel, D.; Smit, B. *Understanding Molecular Simulations: From Algorithms to Applications*, second edi ed.; C. Academic Press: San Diego, CA, 2002.

[108] Rappe, A. K.; Casewit, C. J.; Colwell, K. S.; Goddard, W. a.; Skiff, W. M. *Journal of the American Chemical Society* **1992**, *114*, 10024–10035.

[109] Hagler, A. T.; Ewig, C. S. *Computer Physics Communications* **1994**, *84*, 131–155.

[110] Mayo, S. L.; Olafson, B. D.; Goddard, W. A. I. *Journal of Physical chemistry* **1990**, *101*, 8897–8909.

[111] Jorrgensen, W. L.; Tirado-Rives, J. *Journal of the American Chemical Society* **1988**, *110*, 1510–1657.

[112] Allen, M. P.; Tildesley, D. J. *Computer Simulation of Liquids*, second edi ed.; Oxford Clarendon Press: Oxford, 2017; p 640.

[113] Ewald, P. P. *Annalen Der Physik* **1921**, *64*, 253.

[114] Garcia-Perez, E.; Dubbeldam, D.; Maesen, T. L. M.; Calero, S. *Journal of Physical Chemistry B* **2006**, *110*, 23968–23976.

[115] Calero, S.; Dubbeldam, D.; Krishna, R.; Smit, B.;

Vlugt, T. J. H.; Denayer, J. F. M.; Martens, J. A.; Maesen, T. L. M. *Journal of the American Chemical Society* **2004**, *126*, 11377–11386.

[116] Bai, P.; Tsapatsis, M.; Siepmann, J. I. *The Journal of Physical Chemistry C* **2013**, *117*, 24375–24387.

[117] Garcia-Sanchez, A.; Ania, C. O.; Parra, J. B.; Dubbeldam, D.; Vlugt, T. J. H.; Krishna, R.; Calero, S. *Journal of Physical Chemistry C* **2009**, *113*, 8814–8820.

[118] Harris, J. G.; Yung, K. H. *Journal of Physical Chemistry* **1995**, *99*, 12021–12024.

[119] Martin-Calvo, A.; Lahoz-Martin, F. D.; Calero, S. *Journal of Physical Chemistry C* **2012**, *116*, 6655–6663.

[120] Martin-Calvo, A.; Garcia-Perez, E.; Garcia-Sanchez, A.; Bueno-Perez, R.; Hamad, S.; Calero, S. *Physical Chemistry Chemical Physics* **2011**, *13*, 11165–11174.

[121] Martin-Calvo, A.; Gutierrez-Sevillano, J. J.; Parra, J. B.; Ania, C. O.; Calero, S.; Gutiérrez-Sevillano, J. J.; Parra, J. B.; Ania, C. O.; Calero, S. *Phys. Chem. Chem. Phys.* **2015**, *17*, 24048–24055.

[122] Bourasseau, E.; Lachet, V.; Desbiens, N.; Maillet, J.-B.; Teuler, J.-M.; Ungerer, P. *The journal of physical chemistry. B* **2008**, *112*, 15783–15792.

[123] Jorgensen, W. L.; Chandrasekhar, J.; Madura, J. D.; Impey, R. W.; Klein, M. L. *The Journal of Chemical Physics* **1983**, *79*, 926.

[124] Sokkalingam, N.; Kamath, G.; Coscione, M.; Potoff, J. J. *The Journal of Physical Chemistry B* **2009**, *113*, 10292–10297.

[125] Stubbs, J. M.; Potoff, J. J.; Siepmann, J. I. *Journal of Physical Chemistry B* **2004**, *108*, 17596–17605.

[126] Müller, T. J.; Müller-Plathe, F. *Journal of Hazardous Materials* **2009**, *168*, 13–24.

[127] Vishnyakov, A.; Gor, G. Y.; Lee, M. T.; Neimark, A. V. *Journal of Physical Chemistry A* **2011**, *115*, 5201–5209.

[128] Metropolis, N.; Rosenbluth, A. W.; Rosenbluth, M. N.; Teller, A. H.; Teller, E. *The Journal of Chemical Physics* **1953**, *21*, 1087–1092.

[129] Smit, B.; Siepmann, J. I. *Journal of Physical Chemistry* **1994**, *98*, 8442–8452.

[130] Rosenbluth, M. N.; Rosenbluth, A. W. *The Journal of Chemical Physics* **1955**, *23*, 356–359.

[131] Shi, W.; Maginn, E. J. *Journal of Chemical Theory and Computation* **2007**, *3*, 1451–1463.

[132] Dubbeldam, D.; Calero, S.; Ellis, D. E.; Snurr, R. Q. *Molecular Simulation* **2016**, *42*, 81–101.

[133] Smith, W. R.; Triska, B. *The Journal of Chemical Physics* **1994**, *100*, 3019–3027.

[134] Johnson, J. K.; Panagiotopoulos, A. Z.; Gubbins, K. E. *Molecular Physics* **1994**, *81*, 717–733.

[135] Dubbeldam, D.; Torres-Knoop, A.; Walton, K. S. *Molecular Simulation* **2013**, *39*, 1253–1292.

[136] Turner, C.; Brennan, J. K.; Lísal, M.; Smith, W. R.; Karl Johnson, J.; Gubbins, K. E. *Molecular Simulation* **2008**, *34*, 119–146.

[137] Hansen, N.; Jakobtorweihen, S.; Keil, F. J. *Journal of Chemical Physics* **2005**, *122*, 164705.

[138] Talu, O.; Myers, A. L. *AIChE Journal* **2001**, *47*, 1160–1168.

[139] Duren, T.; Sarkisov, L.; Yaghi, O. M.; Snurr, R. Q. *Langmuir* **2004**, *20*, 2683–2689.

[140] Widom, B. *The Journal of Chemical Physics* **1963**, *39*, 2808.

[141] Dubbeldam, D.; Snurr, R. Q. *Molecular Simulation* **2007**, *33*, 305–325.

CHAPTER

2

Zeolite Screening for the Separation of Gas Mixtures Containing SO_2, CO_2, and CO

Ismael Matito-Martos, Ana Martín-Calvo, Juan José Gutierrez-Sevillano, Maciej Haranczyk, Manuel Doblaré, José Bernardo Parra, Conchi O. Ania, and Sofía Calero

We used a combination of experiments and molecular simulations to investigate at the molecular level the effects of zeolite structure on the adsorption and diffusion of sulfur dioxide, carbon dioxide and carbon monoxide as well as separation processes of their mixtures. Our study involved different zeolite topologies and revealed numerous structure–property trends depending on the temperature and pressure conditions. Sulfur dioxide, which has the strongest interactions with zeolites due to its size and polarity, showed the largest adsorption across investigated temperatures and pressures. Our results indicate that structures with channel–type pore topology and low pore volume are the most promising for selective adsorption of sulfur dioxide over carbon dioxide and carbon monoxide under room conditions, while structures with higher pore volume exhibit better storage capacity at higher pressure. Our results emphasize the need for considering both adsorption and diffusion processes in the selection of the optimal structure for a given separation process. Our findings help to identify the best materials for effective separation processes under realistic operating conditions.
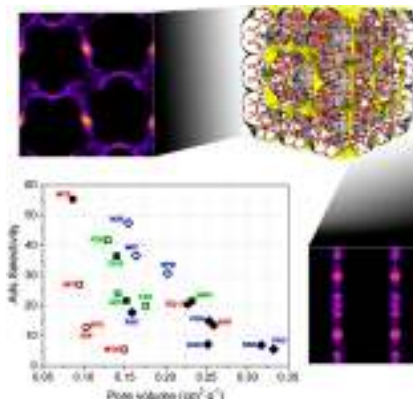
2.1   INTRODUCTION

Sulfur dioxide SO_2 is an ubiquitous component of fuel combustion exhausts and a gas of relevant environmental impact whose control remains a challenging issue [1]. Aside from the toxicity of sulfur dioxide itself, SO_2 emissions also affect the efficiency of carbon dioxide capture processes [2, 3] where investigations have been particularly intense over the last few years to fight the global warming and reduce greenhouse gas emissions. The trace amounts of SO_2 in the flue gas from coal fired plants (typical composition contains 10–15% CO_2, and many other contaminants such as O_2, H_2O, SO_2, NO_x, or H_2 at different levels of concentration) are known to undergo parasitic reactions with current methods for CO_2 capture (namely amines and calcium sorbents). For instance, in the separation of CO_2 by adsorption in amines it is necessary to lower the SO_2 concentration in the gas influent below 10 ppm to minimize the loss of the solvent associated with thermally stable salts of the amine with SO_2 [4, 5]. The sulfation of calcium based sorbents is also a competing process that affects the regeneration temperature of CaO, decreasing the regenerative capacity of the sorbent over subsequent cycles [6, 7]. Whereas research on the simultaneous removal of SO_2/CO_2 mixtures is still under development [8], separation of these gases is crucial to achieve high carbon capture efficiencies.

Over the past few decades, a number of technologies have been developed to prevent the generation and release of SO_2 during combustion processes. They are based on different approaches: before (fuel desulfurization before combustion), during (fluidized bed combustion coupled to integrated gasification combined cycle (IGCC) systems) or post-combustion (flue gas desulfurization) [9, 10]. Sulfur dioxide removal via scrubbing is the most widely applied approach for the post-combustion process due to the availability of efficient scrubber systems and their relatively low cost. However, this process still generates large amounts of solid wastes and off-gas streams, further management and disposal of which entail an important cornerstone of this technology. For instance, the catalytic reduction of SO_2 to elemental sulfur by CO ($2CO + SO_2 \longrightarrow 1/2\ S_2 + 2CO_2$) [11–13] is used to process the off-gas stream generated in flue gas desulfurization systems, to obtain high added value by-products such as elemental sulfur or sulfuric acid. Adsorption of SO_2 in nanoporous materials is a potential alternative technology to reduce or eliminate the emissions of SO_2 and other pollutants, as well as reducing the generation of solids in flue gas desulfurization systems. This would avoid the management and disposal of solid wastes, thereby decreasing the cost and accelerating the implementation of this technology.

In the present work, the separation efficiency of SO_2-containing binary and

ternary mixtures (CO_2/SO_2, CO/SO_2, CO/CO_2/SO_2) was studied through experimental measurements and molecular simulation calculations. We focus on systems containing SO_2 for which available data in the literature are rather scarce [14, 15].

Among nanoporous sorbents, zeolites are promising candidates for this application as molecular sieves [16–19]. Zeolites are crystalline aluminosilicates consisting of tetrahedral units with four oxygen atoms (O atoms) bonded to one atom of silicon, aluminium, or the other fourfold coordinated metal (T atoms). Each aluminium that replaces an atom of silicon generates a negative net charge in the structure that can be balanced by the addition of protons and cations in the system [20, 21]. Tetrahedra are connected via oxygen atoms, generating 3D structures with cages and/or channels. The shape and size of these channels and cages, as well as the silicon/aluminium ratio, and the presence of cations are very important because they influence the adsorption, diffusion, and separation properties [22–28]. Highly ordered zeolite structure have many desirable properties [20, 29, 30], such as high surface area or thermal stability, which make them promising materials for the storage, separation, and purification of gas mixtures [31–33].

The large amount of available zeolitic structures (about 200 unique topologies) and the corrosive nature of sulfur dioxide – hindering their handling – pose a challenge to experimentally screen many structures to identify the most adequate material(s) for the selective separation of sulfur dioxide from post-combustion streams containing carbon dioxide and carbon monoxide. In this study, we aim to guide experimental work by performing a molecular simulation screening of different zeolites, and predict their SO_2 adsorption and separation potential. We provide the molecular level understanding of the effect of the structural features of zeolites, such as the pore topology or accessible pore volume, on the adsorption, diffusion, and separation of sulfur dioxide from carbon dioxide and carbon monoxide. Our study focused on a set of zeolites with a diverse porosity (in terms of pore size, shape and topology) selected from 194 all silica zeolite structures from the IZA database [34]. For these selected structures we have computed adsorption properties and diffusion coefficients of the three gasses under study, and we have compared our simulations with the experimental data available from the literature. We describe the models for zeolites and adsorbates as well as the simulation techniques in Section 2. The obtained results are discussed in Section 3 and we summarize the most relevant conclusions in Section 4.

2.2 METHODS

2.2.1 Computational details

Adsorption isotherms were computed using Monte Carlo simulations in the Grand

Canonical ensemble (GCMC), where the temperature, the volume, and the chemical potential remain fixed. Chemical potential is associated with the fugacity, and fugacity is directly related to pressure with the fugacity coefficient. Simulations were performed at 298 K. Based on the type of gas and on the operating conditions, in this work we equate pressure with fugacity, i.e. the fugacity coefficient is 1. To compare simulated and experimental isotherms, absolute adsorption is converted to excess adsorption [35, 36]. Simulations were performed using our inhouse code RASPA [37]. This code has been extensively tested and validated with a large number of experimental and simulation data [17, 38–41]. Isosteric heats of adsorption and Henry coefficients were computed using the Widom test particle method [42]. Selfdiffusion coefficients were computed from the mean square displacements of the adsorbates calculated from molecular dynamic simulations in the canonical ensemble. Simulations start from equilibrium conditions previously achieved using GCMC simulations for ternary mixtures. Successive configurations of the system were generated by integrating Newton's laws of motion using the Verlet algorithm. We use the Nosé–Hoover thermostat with a time scale on which the system thermostat evolves of 0.15 ps. The self-diffusion coefficients were computed at 298 K from the slope of the mean-square displacement at long times. Simulations have been run for 1000-10.000 ps using an integration

time step of $\tau = 5x10^4$ ps. Before starting collecting data we perform a short MC simulation to obtain a sensible configuration. Other properties of the structures such as surface area and pore volume were also computed for later analysis.

Atomic interactions were described by Lenard-Jones and Coulomb potentials. We use a cutoff distance of 12 Å, and Ewald summation to calculate Coulombic interactions. We used previously published models for carbon dioxide and carbon monoxide [38, 40]. Sulfur dioxide molecules are modeled rigid with a S-O bond length of 1.431 Å and an O-S-O bond angle of 119° . To mimic the dipole moment of the molecule (1.62 Debye) [43] we assigned point charges to the sulfur atom (0.402 e^-) and to the oxygen atoms (-0.201 e^-). The Lennard-Jones parameters for sulfur dioxide were obtained by fitting to the vapour-liquid equilibrium curve (Figure A1. 1 in the Apendix 1) [44]. To compute this curve we used Gibbs-ensemble Monte Carlo simulations [42]. Interactions between adsorbates are computed using Lorentz-Berthelot mixing rules [45, 46]. Since zeolites not always obey the Lorentz-Bethelot mixing rules [17, 38] for the adsorbate-adsorbent interactions Lennard-Jones parameters have to be adjusted independently to reproduce the experimental data [17, 38]. We define the adsorbate-adsorbent interactions by those of the oxygen atoms of the framework (Ozeo) with all the atoms from the adsorbed molecules. We use the Lennard-

Table 1. Lennard-Jones parameters and partial charges of the adsorbates and the structure.

Atom 1	Atom2	ε/k_B(K)	σ(Å)	Charge (e^-)
Adsorbed molecules				
C(CO_2)	C(CO_2)	29.933	2.745	0.651
O(CO_2)	O(CO_2)	85.671	3.017	−0.326
C(CO)	C(CO)	16.141	3.658	−0.242
O(CO)	O(CO)	98.014	2.979	−0.274
Dum(CO)	Dum(CO)	—	—	0.517
S(SO_2)	S(SO_2)	189.353	3.410	0.402
O(SO_2)	O(SO_2)	58.725	3.198	−0.201
Zeolite				
O(Zeo)	O(Zeo)	—	—	−0.393
Si(Zeo)	Si(Zeo)	—	—	0.786
Zeolite – adsorbed molecules				
C(CO_2)	O(zeo)	37.595	3.511	—
O(CO_2)	O(zeo)	78.980	3.237	—
C(CO)	O(zeo)	40.109	3.379	—
O(CO)	O(zeo)	98.839	3.057	—
Dum(CO)	O(zeo)	—	—	—
S(SO_2)	O(zeo)	138.555	3.168	—
O(SO_2)	O(zeo)	77.161	3.066	—

Jones parameters proposed by Garcia-Sanchez *et al.* [38] to reproduce the interactions with carbon dioxide. The Lennard-Jones parameters to reproduce the interactions between the other two adsorbates (sulfur dioxide and carbon monoxide) and the zeolites were developed in this work. Lennard-Jones parameters and partial charges of the molecules are summarized in Table 1.

A set of 194 all silica zeolite structures from the International Zeolite Association (IZA) [34] was characterized in terms of pore geometry and topology using Zeo++ software [47, 48]. Zeo++ performs segmentation of the void space to identify pore systems accessible to a given probe. For each pore system Zeo++ calculates dimensionality of the pore system, the diameter of the largest included sphere (Di), the largest free sphere (Df), and the largest included sphere along the free sphere path (Dif).

Di measures the largest opening in the structure while Df measures the restriction along the diffusion pathway of the largest spherical probe. All calculations performed with Zeo++ involve hard sphere approximation for atoms. A radius of 1.35 Å was assumed for both O and Si atoms [49] while a probe radius of 1.4 Å was used for the void space segmentation to detect pore systems. Additionally, each characterized material is classified as either a channel or an interconnected cage system based on the ratio of Dif and Df, where a channel is recognized for structures with Dif/Df < 1.5, and an interconnected cage system otherwise. The results of the above characterization for the selected zeolites are collected in Tables A1.1-A1.4 in the Apendix 1. Thus, the structures were classified according to their channel or interconnected cage character, and the corresponding directionality, 1-3, of the pore space. We selected structures within each of these six classes to obtain representative sets: 1D channels (ASV, DON, ITW, JRY, LAU, LTL, MOR, NAT, PON), 2D channels (AFR, FER, IWV, NES, SFO, SFG, TER), 3D channels (AFY, BEC, BOG, MEL, MFI, ITR, SBT, STW, SZR), 1D interconnected cages (ITE, MTF, SAS), 2D interconnected cages (DDR, LEV, MWW), 3D interconnected cages (CHA, ERI, FAU, LTA, KFI, PAU, RHO, SBE). The pore landscapes of representative structures of each group are shown in Figure 1. The pore landscapes for all the selected structures
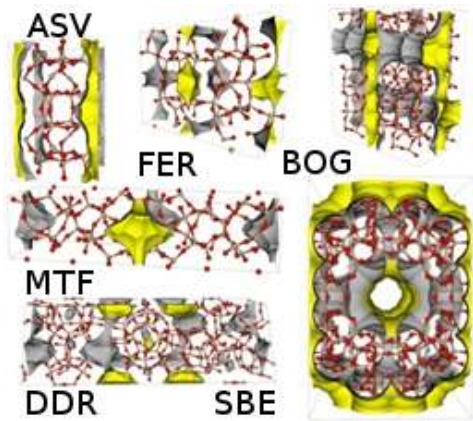
Figure 1. Pore landscapes of representative zeolites used in this work. Channels: 1D, 2D and 3D – ASV, FER and BOG, respectively; interconnected cages: 1D, 2D and 3D – MTF, DDR and SBE, respectively. The inner surface of the pores is highlighted in yellow. The color codes for atoms are red and beige for oxygen and silicon, respectively.

are shown in Figures A1.2-A1.4 in Apendix 1.

We considered all zeolites under study as all silica, rigid models [34, 50–67]. The set of charges of the frameworks are taken from Garcia-Sanchez *et al.* [38]. A summary of some characteristics of the different zeolites, such as their unit cell lengths, angles, computed pore volumes, and computed surface areas can be found in Table A1.5 in the Apendix 1.

2.2.2   Experimental details

All silica (Si/Al ≈ ∞) MFI was kindly supplied by the Instituto de Tecnología Química (ITQ) belonging to the Consejo Superior de Investigaciones Científicas (CSIC). Experimental adsorption isotherms of CO at temperatures near ambient conditions were performed in a volumetric analyzer (ASAP 2020, Micromeritics) in the pressure range from 10^{-2} up to 120 kPa; the instrument was equipped with a turbo molecular vacuum pump and three pressure transducers (0.13, 1.33, and 133 kPa, uncertainty within 0.15% of each reading) to enhance the sensitivity in the low pressure range. Prior to the adsorption measurements, the zeolite was in situ outgassed under vacuum (ca. 10^3 kPa) at 673 K overnight. All of the isotherms were done in triplicate, and the data are reproducible with an error below 0.1%. The temperature of the isotherms was controlled using a thermostatic circulating oil bath. Ultrahigh purity CO (i.e., 99.995%) was supplied by Air Products.

2.3   RESULTS AND DISCUSSION

The adsorption loadings computed for sulfur dioxide, carbon dioxide, and carbon monoxide, as pure components, as well as for the 20:40:40 ternary mixture ($SO_2/CO_2/CO$), and the CO_2/CO equimolar binary mixture were obtained at a pressure span from 10^{-1} to 10^4 kPa. Self-diffusion coefficients were obtained from the adsorption isotherms of ternary mixtures under ambient conditions. The adsorption properties in the low coverage regime (Isosteric heats of adsorption and Henry coefficients) were computed for the three adsorbates in all the zeolites under study. In the case of mixtures we studied

(a) the selective adsorption and diffusion behavior of the ternary mixture at atmospheric pressure and room temperature, and (b) the selective adsorption behavior of the CO_2/CO binary equimolar mixture. Based on our findings we have discussed separation performance in terms of both pore volume and permselectivity.

2.3.1 Adsorption of pure components for force field validation

Pure component gas adsorption isotherms were computed and compared to available experimental data to validate the force-field parameters developed in this work for CO and SO_2 accounting for the gas-adsorbent interactions. The parameters describing CO_2-zeolite interactions have been validated in a previous work [38]. Simulated and experimental adsorption isotherms of SO_2 and CO as pure components on MFI are shown in Figure 2. In order to compare with experimental data we performed additional adsorption isotherms in the range of temperature that spans from 258 K to 373 K. It should be mentioned that available experimental data for SO_2 adsorption on nanoporous materials are rather scarce, due to the corrosive nature of this gas that makes difficult its handling. Anyhow, Figure 2a shows a comparison of our simulated SO_2 adsorption isotherms in MFI at 298-373 K with the available experimental
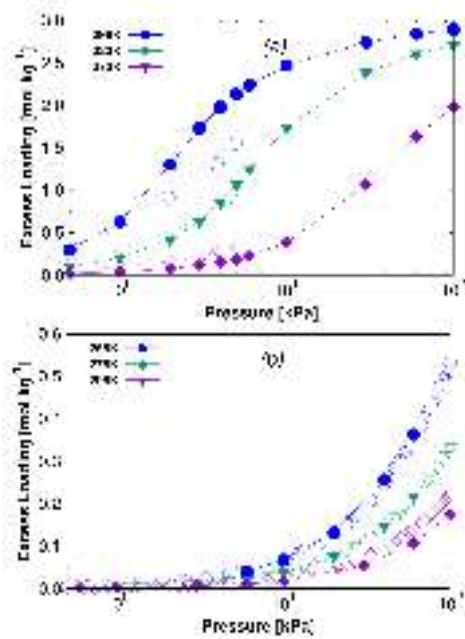
Figure 2. Comparison of simulated (open symbols) and experimental (closed symbols) pure component adsorption isotherms of (a) sulfur dioxide and (b) carbon monoxide in MFI at various temperatures. Experimental values of sulfur dioxide are taken from Deng and Lin [68]. The experimental values for carbon monoxide were measured in this work.

data from Deng and Lin [68]. Simulations are in good agreement with experiments at all three temperatures, with a slight overestimation of the adsorption capacity at 298 K. This could be attributed to the fact that simulations are computed considering rigid and clean zeolite structures while zeolites can exhibit some flexibility, and experimental data are recorded on materials that may often present structural defects or impurities (i.e. adsorbed water and/or other residues from the syn-

thesis) that would lead to a lower gas adsorption capacity. Figure 2b shows the perfect match between our experimental and computed adsorption isotherms of CO in MFI. The good agreement at several temperatures obtained for both CO and SO_2 validates the forcefields used in this study for both gases.

2.3.2 Isosteric heats of adsorption and Henry coefficients

Computed isosteric heats of adsorption for sulfur dioxide, carbon dioxide, and carbon monoxide as a function of the pore volume of the zeolites at 298 K are shown in Figure 3. The results show higher absolute values of sulfur dioxide, following the trend $SO_2 > CO_2 > CO$ regardless of the zeolite. Similar trends were reported by Ding and Yazaydin for several MOFs [2]. This behaviour can be related to the shape and size of the molecules in combination with the Coulombic interactions between the adsorbate and the adsorbent. Among the three gases, SO_2 is not only the biggest molecule (molecular diameter, 4.11-4.29 Å) [43, 69] but also has the highest dipole moment. More specifically, molecular size seems to be more important than polarity since the interaction with all zeolites is stronger for carbon dioxide (i.e., 3.90 Å) [69, 70] than for carbon monoxide (i.e., 3.69 Å) [69, 70]. We also observed bigger differences among the values obtained for SO_2 since the fitting of the bulkier mole-
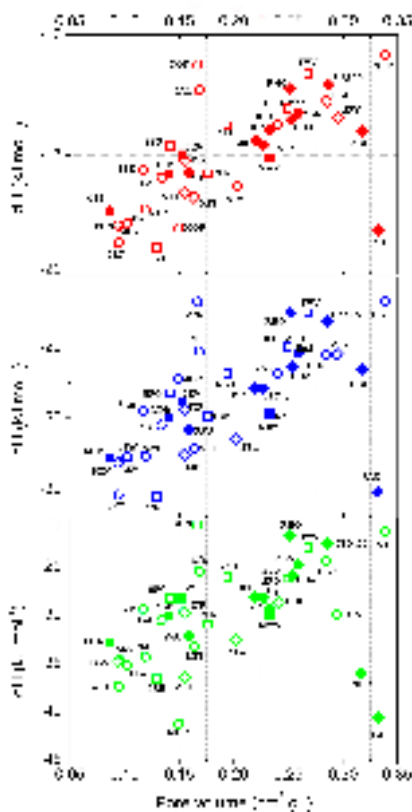
Figure 3. Computed isosteric heats of adsorption of carbon monoxide (red), carbon dioxide (blue), and sulfur dioxide (green) as a function of the pore volume of the structures at 298 K. Open symbols show the results obtained for channel-type zeolites and closed symbol for the interconnected cage-type zeolites. The directionality of the pore space is represented by circles (1D), squares (2D) or diamonds (3D).

cules is more dependent on the pore system. In a similar way, differences between the heats of adsorption of structures with similar topology and pore volume are larger for sulfur dioxide than for the other two molecules. As a general rule, zeolitic frameworks with high pore volumes ex-

hibit low heats of adsorption for all three studied gases. Some structures such as MOR, AFY, and TER escape from this trend. To understand this anomalous behaviour we computed the average occupation profiles of the gases inside the structures.

For instance, the isosteric heats of adsorption of SO_2 and CO in MOR (1D channel-type zeolite) are higher than expected; the corresponding average occupation profiles depicted in Figure 4 show that this is linked to the confinement effect of these gases at low coverage in the side pockets of MOR, being the preferential sites of adsorption [17]. SO_2 and CO commensurate better than CO_2 in the pockets for a combined effect of geometry and polarity, thus the occupation density of the side pockets is larger for SO_2 followed by CO and CO_2 . The average occupation profiles obtained for AFY (Figure 4) also revealed the existence of specific adsorption sites for sulfur dioxide and carbon monoxide, while carbon dioxide is only adsorbed in the big-straight channels of the host where the interaction with the structure is weaker.

The different behaviour of the heat of adsorption is due to the preferential sites of adsorption in which bulkier molecules fit better due to a mere size entropy effect (i.e., confinement) [27]. In TER, a 2D channel-type structure, sulfur dioxide shows the highest occupation density of the sites, followed by carbon dioxide and carbon monoxide (Figure A1. 5 in Apendix
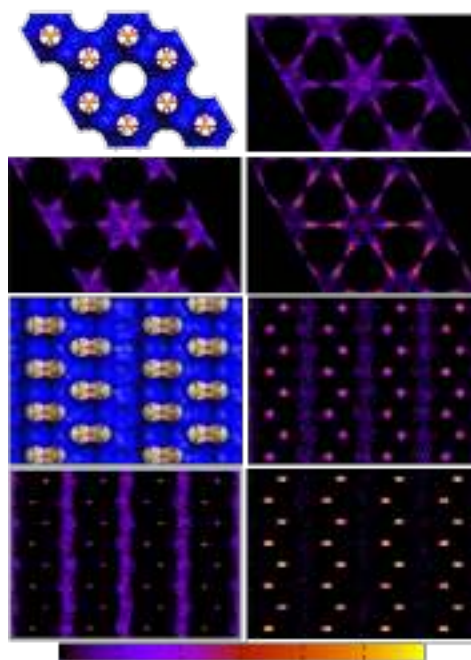
Figure 4. Average occupation profiles obtained in AFY (top), and MOR (bottom) for one molecule of carbon monoxide (top right), carbon dioxide (bottom left), and sulfur dioxide (bottom right). The figure shows the projection of the center of mass of the molecules over x-y (AFY) and y-z (MOR) planes. The color graduation indicates the occupational density (from black to yellow). To guide the view we add a representation of the structures. The atomic structures are represented by the oxygen and silica atoms in red and yellow respectively. Grid surfaces where the accessible part appears in blue and the non-accessible part is colored in gray are also depicted.

1). In zeolite TER, the intersections between the channels are the preferential adsorption sites, as opposed to other zeolites of the same group (SFG and NES) where molecules are preferentially adsorbed in the wide channels (Figure A1. 6 and A1. 7

in Apendix 1). The aforementioned effect can also explain the differences in the heats of adsorption obtained for the three gases in LTL and DON (1D channel-type) or those found in MEL, MFI, ITR, and SZR (3D channel-type). As shown in the average occupation profiles obtained for MEL (Figure 5) sulfur dioxide is preferentially adsorbed in the main straight interconnecting channels, whereas the molecules of carbon dioxide and carbon monoxide can also be found in the intersections of the channels. For MFI the three gases follow the same trend as in MEL (Figure A1. 8 in Apendix 1), while the preferential adsorption sites in ITR and SZR are the intersecting channels and the big straight channels respectively (Figure A1. 9 and A1. 10 in Apendix 1).

A number of investigated structures have SO_2 and CO_2 preferential adsorption sites that are neither side pockets, straight channels nor intersecting channels. For example, the preferential sites of adsorption in the 2D cage-type structures MWW and KFI are the windows that communicate cages (Figure A1. 11 in Apendix 1). As a result, the heats of adsorption of SO_2 and CO_2 in KFI are higher than expected from general trends, since the gases are not adsorbed in the big cages but in a small cavity created by the windows between cages (Figure 5). Similarly, the preferential adsorption sites for SBE (Figure 5) and FAU (Figure A1. 12 in the Apendix 1) are the windows connecting big cages. Despite these two structures displaying
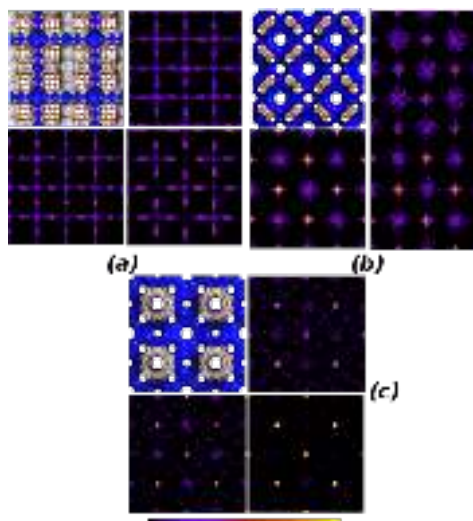
Figure 5. Average occupation profiles obtained for one molecule of carbon monoxide (top right), carbon dioxide (bottom left), and sulfur dioxide (bottom right) in (a) MEL, (b) KFI and (c) SBE zeolites. The figures show the projections of the center of mass of the molecules over the x-y plane. The color graduation indicates the occupational density (from black to yellow). To guide the view we add a representation of the structure (top left). The atomic structure is represented by the oxygen and silica atoms in red and yellow respectively. A grid surface is also depicted (where the accessible part is colored in blue and the non-accessible part is colored in gray).

among the highest pore volumes analyzed in this work, they also exhibit the highest values of heat of adsorption. This is contrary to the general trend: the larger the pore volume the lower the heat of adsorption. On the other hand, we did not observe a direct correlation between the topology of the zeolites and the isosteric heats of adsorption. An observation that a local structure feature can dominate ad-

sorption properties such as heat of adsorption and the Henry coefficient was recently used to develop an efficient screening approach for carbon capture materials [71–74].

The selectivity of the zeolites at low pressure for gas component i over j at a given temperature can be estimated using the ratio between the Henry coefficient of each gas (K_{Hi}/K_{Hj}). The dependence of the selectivity at low coverage on the pore volume of the structure for SO_2 over CO_2 and CO_2 over CO at 298 K is shown in Figure 6a and 7a, respectively. The trends are similar to those obtained for the heats of adsorption, with higher selectivities obtained for the structures showing the lowest pore volumes. Again, MOR and AFY follow an anomalous trend of selectivity, with values for SO_2/CO_2 and CO_2/CO larger and lower, respectively, than those of other structures with similar pore volumes. Also, those structures where bulky molecules fit better (MEL, MWW, SBE and FAU) exhibit higher selectivity of sulfur dioxide over carbon dioxide. In the case of CO_2/CO selectivity, it follows the trend: 3D > 2D > 1D for structures with similar pore volumes due to the appearance of preferential sites of adsorption at the intersections of the channels. In addition, the fact that the occupation density of the preferential adsorption sites is higher in FAU than in SBE is the reason that leads to higher values of selectivity for the former than for the latter.

In summary: the highest values of heat
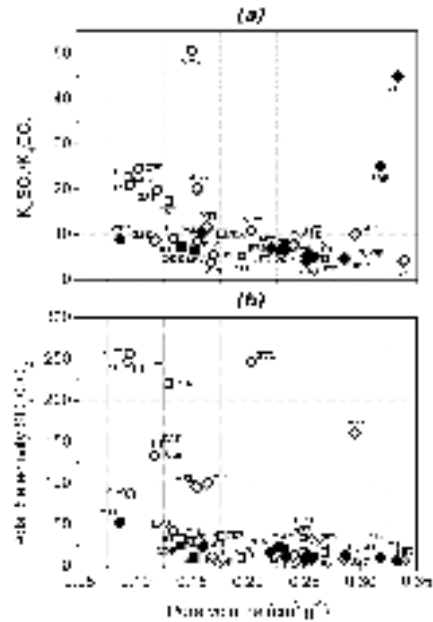
Figure 6. (a) Computed Henry coefficients of sulfur dioxide over carbon dioxide at room temperature and (b) adsorption selectivity of sulfur dioxide over carbon dioxide, from the ternary mixture (SO_2, CO_2, and CO with ratio 20 : 40 : 40) at room pressure and temperature. Both as a function of the pore volume of the structures. Open symbols show the results obtained for channel-type zeolites and closed symbols to the interconnected cage-type zeolites. The directionality of the pore space is represented by circles (1D), squares (2D), or diamonds (3D).

of adsorption for carbon monoxide were found for JRY, FER, and FAU. These three structures also exhibit the strongest interaction with carbon dioxide. FER and MTF are the structures with higher selectivity of carbon dioxide over carbon monoxide. MOR and FAU are the structures with higher heats of adsorption for sulfur dioxide, and therefore with higher selectivity of sulfur dioxide over carbon dioxide.
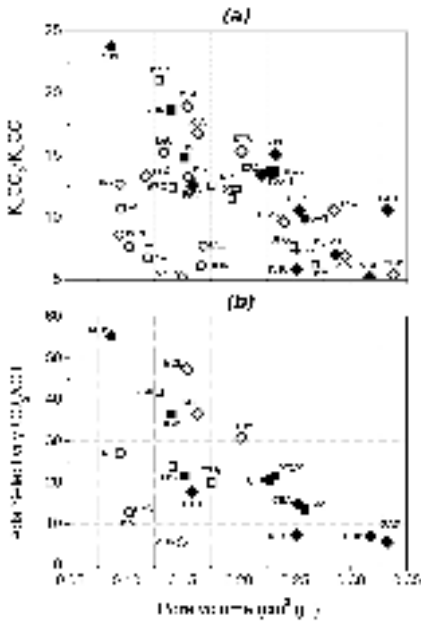
Figure 7. (a) Computed Henry coefficients of carbon dioxide over carbon monoxide at room temperature and (b) adsorption selectivity of carbon dioxide over carbon monoxide, from the binary equimolar mixture at room pressure and temperature. Both as a function of the pore volume of the structures. Open symbols show the results obtained for channel-type zeolites and closed symbols to the interconnected cage-type zeolites. The directionality of the pore space is represented by circles (1D), squares (2D), or diamonds (3D).

2.3.3 Adsorption selectivity from the ternary mixture

In a multicomponent system the adsorption selectivity of a component i over a component j (S_{ij}) is defined as $(x_i/y_j)/(x_j/y_i)$ where $x_{i,j}$ are the molar fractions in the adsorbed phase and $y_{i,j}$ the molar fractions in the bulk phase. Figure 6b shows the adsorption selectivities of

sulfur dioxide over carbon dioxide computed from the mixture 20% SO_2, 40% CO_2, and 40% CO at room temperature and atmospheric pressure. Table A1. 6 in the Apendix 1 collects the computed loading for each component in terms of mol of adsorbate per kilogram of structure, and the obtained values for the selectivity for each structure.

For the ternary mixture the highest adsorption was obtained for sulfur dioxide, the gas in the lowest proportion in the bulk, regardless of the zeolite structure. The adsorption of carbon dioxide is drastically reduced by the presence of sulfur dioxide, in agreement with the studies of Ding and Yazaydin [2], whereas the adsorption of carbon monoxide is almost negligible.

The SO_2/CO_2 selectivity is higher for the structures with lower pore volume, in a similar way already described for the heats of adsorption and the selectivity estimated at low coverage. Due to their low pore volumes, a few structures such as JRY, PON and ITW (1D channel-type), FER (2D channel-type), or STW (3D channels-type) show extremely high SO_2/CO_2 selectivities. In these structures the loading of carbon dioxide is extremely low, and the confinement effect of SO_2 (main component in the adsorbed phase) also enhances the SO_2/CO_2 selectivity. The packing effect of the gases gradually disappears in structures with higher pore volumes, leading to lower values of selectivity, with the ex-

ception of AFY (structure with high pore volume showing high selectivity). The heat of adsorption of sulfur dioxide in this zeolite was higher than in other structures with similar pore volume. This stronger interaction of SO_2 with the structure also implies higher loading of sulfur dioxide. The high heat of adsorption in combination with the size entropy effect previously described [27] explains the high selectivity for AFY. Due to the large pore volume of this structure this selectivity could be enhanced with a slight increase of the pressure.

At this stage it is important to highlight that some of the aforementioned different heats of adsorption at low coverage are not observed at higher coverages. As the preferential sites of adsorption at low coverage are filled and the gas loading rises (increasing pressure), molecules are adsorbed in other sites where the gas-host interaction is weaker. A good example of this behaviour is found in FAU, which exhibits an extremely high heat of adsorption for sulfur dioxide at zero loading. The preferential adsorption sites at low coverage for FAU are the windows that interconnect the big cages. The strength of the interaction is very high at the windows but not at the big cages. At higher loadings most molecules tend to be adsorbed in the latter and it is for this reason that the loading of sulfur dioxide and carbon dioxide at room pressure in the ternary mixtures is low and therefore the selectivity is also very low.

The CO_2/CO selectivity for the ternary mixture under the studied conditions (ca. 20% SO_2, 40% CO_2, and 40% CO at room temperature and atmospheric pressure) cannot be obtained since the adsorption of carbon dioxide is drastically reduced by the presence of sulfur dioxide and the adsorption of carbon monoxide is almost negligible. For a good understanding of the competition of carbon dioxide and carbon monoxide, we performed adsorption isotherms for the equimolar binary mixture at room temperature and atmospheric pressure using the most representative structures of each group.

2.3.4 Adsorption selectivity from CO_2/CO binary mixtures

Figure 7b shows the SO_2/CO adsorption selectivity for equimolar binary mixtures in several zeolites at atmospheric pressure and room temperature. Table A1. 7 in the Apendix 1 summarizes the loading of each gas in each structure as well as the adsorption selectivity. As predicted from the low coverage regime (Figure 7b), CO_2 is selectively adsorbed over CO in all the structures, which is attributed to the bigger size of CO_2 that allows a better fit in the structures. Comparatively, carbon dioxide loading in the studied structures is lower than that of sulfur dioxide under the same conditions of pressure and temperature in the ternary mixture. Differences in the adsorbed amount between carbon monox-

ide from the binary mixture and sulfur dioxide from the ternary were about 1-3 mol kg^{-1} lower in channel-type zeolites and 0.5-2 mol kg^{-1} in interconnected cage-type.

As in the case of the ternary mixtures, the selectivity is higher for the zeolites displaying low pore volumes. In addition, for a given pore volume it follows the trend: 3D > 2D > 1D due to the effect of the channel intersection previously explained. In the binary CO_2/CO mixture, the adsorption selectivity of all the structures shows the same trend described for the Henry coefficient selectivities. Unlike sulfur dioxide, the weaker interaction of CO_2 and CO with the structures reduces the loading, thus just low-medium coverage is reached under the given conditions of pressure and temperature. Therefore the behaviour is similar to that shown with the Henry coefficients. Only FAU showed lower adsorption selectivity than that expected from the Henry coefficients. This is due to the high pore volume of the zeolite and the lowgas loading, avoiding the competition between both gases for the preferential sites of adsorption of the structure.

2.3.5 Self-diffusion and permselectivity from the ternary mixture

Table 2 shows the averaged self-diffusion coefficients, calculated for sulfur dioxide and carbon dioxide from the slope of the mean square displacement of the adsorbed

Table 2. Average self-diffusion coefficients (10^{-8} m^{2}s^{-1}) for sulfur dioxide and carbon dioxide from the ternary mixture at fixed temperature (298 K), volume, and number of molecules. The number of molecules was taken from previous GCMC simulations of the ternary mixture at room pressure and temperature.

Zeolite	SO$_2$	CO$_2$	Zeolite	SO$_2$	CO$_2$
ASV	0.047	0.061	MFI	0.042	0.035
DON	0.672	0.916	ITR	0.126	0.117
ITW	0.007	0.007	SBT	0.545	0.654
JRY	0.011	0.010	STW	0.004	0.002
LAU	0.005	0.004	SZR	0.013	0.029
LTL	0.049	0.081	ITQ-3	0.004	0.002
MOR	0.037	0.111	MTF	0.003	0.005
NAT	0.028	0.024	SAS	0.031	0.025
PON	0.002	0.000	DDR	0.010	0.004
AFR	0.069	0.117	LEV	0.005	0.002
FER	0.029	0.057	MWW	0.149	0.157
IWV	0.122	0.179	CHA	0.016	0.011
NES	0.146	0.192	ERI	0.007	0.003
SFO	0.066	0.129	FAU	1.080	1.430
SFG	0.067	0.074	ITQ-29	0.035	0.021
TER	0.073	0.074	KFI	0.001	0.002
AFY	0.028	0.055	PAU	0.003	0.004
BEC	0.417	0.484	RHO	0.005	0.002
BOG	0.175	0.237	SBE	0.241	1.030
MEL	0.038	0.034			

molecules from he ternary mixture as described above. This parameter was used to discard the zeolites in which the diffusion of sulfur dioxide and carbon dioxide is very low. Thus only zeolites with self-diffusivity values between 10^{-10} and 10^{-8} m^2 s^{-1} were selected to analyze permselectivity. Permselectivity for SO_2 over CO_2 in these structures is depicted in Figure 8, defined as the product of the adsorption selectivity and the diffusion selectivity.

In agreement with the results previously described, permselectivity is higher in structures with lower pore volume, showing JRY and NAT as the best structures for the separation of SO_2 from gas mixtures containing CO_2 and CO. It is interesting to highlight that there are some
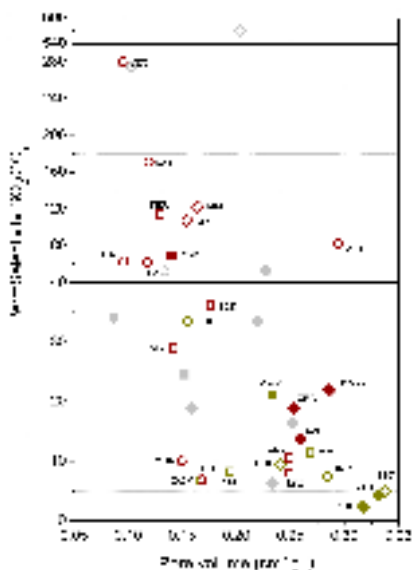
Figure 8. Permselectivity of sulfur dioxide over carbon dioxide from the ternary mixture (SO_2, CO_2, and CO with a ratio of 20:40:40) at room pressure and temperature, as a function of the pore volume of the structures. Open symbols show the results obtained for channel-type zeolites and closed symbols to the interconnected cage-type zeolites. The directionality of the pore space is represented by circles (1D), squares (2D), or diamonds (3D). Zeolites with self-diffusion coefficients in orders between 10^{-8} and 10^{-9} m^2 s^{-1} are colored in green, those around 10^{-10} m^2 s^{-1} in red, and the rest in grey.

structures with low pore volume in which the packing effect made them to have extremely high adsorption selectivity. The synergy between the adsorption and diffusion of a mixture in zeolites for separation processes has been recently proven using both simulations and experiments [75]. Therefore, zeolites such as ITW, PON, and STW, which were initially considered good candidates based on their adsorption

selectivity, are further discarded due to the poor diffusion. On the other hand AFY, zeolite with high pore volume and high storage capacity, also has reasonable diffusion and shows high permselectivity. Therefore, this structure raises as a good candidate for the selective adsorption of sulfur dioxide over carbon dioxide, perhaps working at slightly higher pressures in order to improve its adsorption selectivity.

2.4 CONCLUSIONS

We employed a combination of experiments and molecular simulations to study adsorption and diffusion processes of sulfur dioxide, carbon dioxide, and carbon monoxide in zeolites. Our work shows that out of the three molecules, sulfur dioxide has the strongest interaction with the frameworks due to its largest size and polarity. We screened zeolite structures taking into account not only low coverage adsorption properties but also the adsorption capacity, selectivity, and so forth at the temperature and/or pressure relevant to the separation process. This study outperforms previous studies and demonstrates that the prediction of materials for separation uses should be based on both adsorption and diffusion performance.

For the selective adsorption of SO_2 over CO_2 and CO at atmospheric pressure and room temperature, zeolitic structures with channel-type pore topology and low pore volumes, such as JRY or NAT, are the most adequate. However, to sepa-

rate carbon dioxide from carbon monoxide as a second step of this removal process, higher pressures (or lower temperatures) would be necessary to improve the selectivity and adsorption capacity. On the other hand, structures with high pore volumes, such as AFY, FAU or SBE, could exhibit better storage capacity also working at higher pressure.

We reemphasize that each of the studied structures performs better under different conditions, and pose different opportunities for applications in adsorption, diffusion, and separation. Our study provides an interesting perspective to obtain useful information on their optimum working conditions in terms of pressure and temperature to achieve high gas adsorption capacities and SO_2 selectivity. This knowledge could be used for further enhancement of a variety of adsorption-separation processes.

2.5   Bibliography

[1]   Gauci, V.; Dise, N.; Blake, S. *Geophysical Research Letters* **2005**, *32*, L12804.

[2]   Ding, L. F.; Yazaydin, A. O. *Journal of Physical Chemistry C* **2012**, *116*, 22987–22991.

[3]   Yu, J.; Ma, Y.; Balbuena, P. B. *Langmuir* **2012**, *28*, 8064–8071.

[4]   Rao, A. B.; Rubin, E. S. *Environmental Science & Technology* **2002**, *36*, 4467–4475.

[5]   Singh, D.; Croiset, E.; Douglas, P. L.; Douglas, M. A. *Energy Conversion and Management* **2003**, *44*, 3073–3091.

[6]   Iyer, M. V.; Gupta, H.; Sakadjian, B. B.; Fan, L.-S. *Industrial & Engineering Chemistry Research* **2004**, *43*, 3939–3947.

[7]   Hartman, M.; Trnka, O. *AIChE Journal* **1993**, *39*, 615–624.

[8]   Park, J. Y.; Tomicic, I.; Round, G. F.; Chang, J. S. *Journal of Physics D: Applied Physics* **1999**, *32*, 1006–1011.

[9]   Oikawa, K.; Yongsirib, C.; Takeda, K.; Harimotoa, T. *Environmental Progress* **2003**, *22*, 67–73.

[10]   Srivastava, R. K.; Jozewicz, W.; Singer, C. *Environmental Progress* **2001**, *20*, 219–228.

[11]   Okay, V. C.; Short, W. L. *Inde. Eng. Process Des. Develop.* **1973**, *12*, 291–294.

[12]   Paik, S. C.; Kim, H.; Chung, J. S. *Catalysis Today* **1997**, *38*, 193–198.

[13]   Kim, H.; Won Park, D.; Chul Woo, H.; Shik Chung, J. *Applied Catalysis B: Environmental* **1998**, *19*, 233–243.

[14]   Lachet, V.; de Bruin, T.; Ungerer, P.; Coquelet, C.; Valtz, A.; Hasanov, V.; Lockwood, F.; Richon, D. *Energy Procedia* **2009**, *1*, 1641–1647.

[15]   El Ahmar, E.; Creton, B.; Valtz, A.; Coquelet, C.; Lachet, V.; Richon, D.; Ungerer, P. *Fluid Phase Equilibria* **2011**, *304*, 21–34.

[16]   Himeno, S.; Tomita, T.; Suzuki, K.; Nakayama, K.; Yajima, K.; Yoshida, S. *Industrial & Engineering Chemistry Research* **2007**, *46*, 6989–6997.

[17]   Garcia-Perez, E.; Parra, J. B.; Ania, C. O.; Garcia-Sanchez, A.; Van Baten, J. M.; Krishna, R.; Dubbeldam, D.; Calero, S. *Adsorption* **2007**, *13*, 469–476.

[18]   Krishna, R.; van Baten, J. M.; Garcia-Perez, E.; Calero, S. *Chemical Physics Letters* **2006**, *429*, 219–224.

[19]   Krishna, R.; van Baten, J. M.; Garcia-Perez, E.; Calero, S. *Industrial & Engineering Chemistry Research* **2007**, *46*, 2974–2986.

[20]   Romero, M. D.; Ovejero, G.; Rodríguez, A.; Gómez, J. M. *Microporous and Mesoporous Materials* **2005**, *81*, 313–320.

[21]   García Martínez, J. Sńtesis y caracterización de zeolitas y materiales compuestos zeolita/carbń. Aplicaciones para la eliminaciń de SO_2. Ph.D. thesis, 2000.

[22]   Choudhary, V. R.; Mayadevi, S.; Singh, A. P. *Journal of the Chemical Society-Faraday Transactions* **1995**, *91*, 2935–2944.

[23]   Choudhary, V. R.; Mayadevi, S. *Zeolites* **1996**, *17*, 501–507.

[24]   Dunne, J. A.; Mariwala, R.; Rao, M.; Sircar, S.; Gorte, R. J.; Myers, A. L. *Langmuir* **1996**, *12*, 5888–5895.

[25]   Dunne, J. A.; Rao, M.; Sircar, S.; Gorte, R. J.; Myers, A. L. *Langmuir* **1996**, *12*, 5896–5904.

[26]   Talu, O.; Sun, M. S.; Shah, D. B. *AIChE Journal* **1998**, *44*, 681–694.

[27]   Krishna, R.; Smit, B.; Calero, S. *Chemical Society Reviews* **2002**, *31*, 185–194.

[28]   Schenk, M.; Calero, S.; Maesen, T. L. M.; van Benthem, L. L.; Verbeek, M. G.; Smit, B. *Angewandte Chemie-International Edition* **2002**, *41*, 2499–2502.

[29]   Altshuler, G. N.; Shkurenko, G. Y. *Bulletin of the Academy of Sciences of the USSR Division of Chemical Science* **1990**, *39*, 1331.

[30]   Anerousis, J. P. *Chemical Engineering* **1976**, *83*, 128.

[31]   Zhang, X. Y.; Shen, Q.; He, C.; Ma, C. Y.; Cheng, J.; Hao, Z. P. *Catalysis Communications* **2012**, *18*, 151–155.

[32] Bernal, M. P.; Coronas, J.; Menendez, M.; Santamaria, J. *AIChE Journal* **2004**, *50*, 127–135.

[33] Delgado, J. A.; Uguina, M. A.; Gomez, J. M.; Ortega, L. *Separation and Purification Technology* **2006**, *48*, 223–228.

[34] Baerlocher, C.; McCusker, L. B.; Olson, D. *Atlas of Zeolite Framework types*, 6th ed.; Elsevier: London, 2007.

[35] Duren, T.; Sarkisov, L.; Yaghi, O. M.; Snurr, R. Q. *Langmuir* **2004**, *20*, 2683–2689.

[36] Duren, T.; Snurr, R. Q. *Journal of Physical Chemistry B* **2004**, *108*, 15703–15708.

[37] Dubbeldam, D.; Calero, S.; Ellis, D. E.; Snurr, R. Q. *RASPA, version 1.0*; 2008.

[38] Garcia-Sanchez, A.; Ania, C. O.; Parra, J. B.; Dubbeldam, D.; Vlugt, T. J. H.; Krishna, R.; Calero, S. *Journal of Physical Chemistry C* **2009**, *113*, 8814–8820.

[39] Calero, S.; Martin-Calvo, A.; Hamad, S.; Garcia-Perez, E. *Chemical Communications* **2011**, *47*, 508–510.

[40] Martin-Calvo, A.; Lahoz-Martin, F. D.; Calero, S. *Journal of Physical Chemistry C* **2012**, *116*, 6655–6663.

[41] Gutierrez-Sevillano, J. J.; Dubbeldam, D.; Rey, F.; Valencia, S.; Palomino, M.; Martin-Calvo, A.; Calero, S. *Journal of Physical Chemistry C* **2010**, *114*, 14907–14914.

[42] Frenkel, D.; Smit, B. *Understanding Molecular Simulations: From Algorithms to Applications*, second edi ed.; C. Academic Press: San Diego, CA, 2002.

[43] Li, J.-R.; Kuppler, R. J.; Zhou, H.-C. *Chemical Society reviews* **2009**, *38*, 1477–1504.

[44] National Institute of Standards and Technology. http://www.nist.gov/index.html.

[45] Allen, M. P.; Tildesley, D. J. *Computer Simulation of Liquids*; Oxford Clarendon Press: Oxford, 1987.

[46] Vega, C.; Garzon, B.; MacDowell, L. G.; Padilla, P.; Calero, S.; Lago, S. *J. Phys.-Condes. Matter* **1996**, *8*, 9643.

[47] Willems, T. F.; Rycroft, C. H.; Kazi, M.; Meza, J. C.; Haranczyk, M. *Microporous and Mesoporous Materials* **2012**, *149*, 134–141.

[48] Zeo++. www.carboncapturematerials.org/Zeo++.

[49] Foster, M. D.; Rivin, I.; Treacy, M. M. J.; Delgado Friedrichs, O. *Microporous and Mesoporous Materials* **2006**, *90*, 32–38.

[50] Wessels, T.; Baerlocher, C.; McCusker, L. B.; Creyghton, E. J. *Journal of the American Chemical Society* **1999**, *121*, 6242–6247.

[51] Artioli, G.; Stahl, K. *Zeolites* **1993**, *13*, 249–255.

[52] Newsam, J. M. *Journal of Physical Chemistry* **1989**, *93*, 7689–7694.

[53] Gramlich, V. Untersuchung und Verfeinerung pseudosymmetrischer Strukturen. Ph.D. thesis, 1971.

[54] Morris, R. E.; Weigel, S. J.; Henson, N. J.; Bull, L. M.; Janicke, M. T.; Chmelka, B. F.; Cheetham, A. K. *Journal of the American Chemical Society* **1994**, *116*, 11849–11855.

[55] Pluth, J. J.; Smith, J. V. *American Mineralogist* **1990**, *75*, 501–507.

[56] Fyfe, C. A.; Gies, H.; Kokotailo, G. T.; Pasztor, C.; Strobl, H.; Cox, D. E. *Journal of the American Chemical Society* **1989**, *111*, 2470–2474.

[57] van Koningsveld, H.; van Bekkum, H.; Jansen, J. C. *Acta Crystallographica Section B-Structural Science* **1987**, *43*, 127–132.

[58] Camblor, M. A.; Corma, A.; Lightfoot, P.; Villaescusa, L. A.; Wright, P. A. *Angewandte Chemie-International Edition* **1997**, *36*, 2659–2661.

[59] Gies, H. *Z. Kristallogr.* **1986**, *175*, 93–104.

[60] Merlino, S.; Galli, E.; Alberti, A. *Tschermaks Min. Petr. Mitt* **1975**, *22*, 117–129.

[61] Calligaris, M.; Nardin, G.; Randaccio, L. *Zeolites* **1983**, *3*, 205–208.

[62] Gard, J. A.; Tait, J. M. *Proc. 3rd Int. Conf. Molecular Sieves* **1973**, 94–99.

[63] Hriljac, J.; Eddy, M.; Cheetham, A.; Donohue, J.; Ray, G. *Journal of Solid State Chemistry* **1993**, *106*, 66–72.

[64] Corma, A.; Rey, F.; Rius, J.; Sabater, M. J.; Valencia, S. *Nature* **2004**, *431*, 287–290.

[65] Parise, J. B.; Shannon, R. D.; Prince, E.; Cox, D. E. *Zeitschrift Fur Kristallographie* **1983**, *165*, 175–190.

[66] Gordon, E. K.; Samson, S.; Kamb, W. B. *Science* **1966**, *154*, 1004–1007.

[67] McCusker, L. B.; Baerlocher, C. *J. Solid State Chem.* **1984**, 812–822.

[68] Deng, S. G.; Lin, Y. S. *Industrial & Engineering Chemistry Research* **1995**, *34*, 4063–4070.

[69] Joseph, O. H.; Charles, F. C.; Byron, R. B. *Molecular theory of gases and liquids*; John Wiley & Sons, Inc., New York, 1954.

[70] Sircar, S. *Industrial & Engineering Chemistry Research* **2006**, *45*, 5435–5448.

[71] Kim, J.; Abouelnasr, M.; Lin, L.-C.; Smit, B. *Journal of the American Chemical Society* **2013**, *135*, 7545–7552.

[72] Lin, L.-C.; Berger, A. H.; Martin, R. L.; Kim, J.; Swisher, J. A.; Jariwala, K.; Rycroft, C. H.; Bhown, A. S.; Deem, M.; Haranczyk, M.; Smit, B. *Nature Materials* **2012**, *11*, 633–641.

[73] Martin, R. L.; Willems, T. F.; Lin, L. C.; Kim, J.; Swisher, J. A.; Smit, B.; Haranczyk, M. *Chemphyschem* **2012**, *13*, 3595–3597.

[74] Kim, J.; Lin, L.-C.; Swisher, J. A.; Haranczyk, M.; Smit, B. *Journal of the American Chemical Society* **2012**, *134*, 18940–18943.

[75] Titze, T.; Chmelik, C.; Kärger, J.; van Baten, J. M.; Krishna, R. *The Journal of Physical Chemistry C* **2014**, *118*, 2660–2665.

Zeolites for the Selective Adsorption of Sulfur Hexafluoride

Ismael Matito-Martos, Juan Álvarez-Ossorio, Juan José Gutierrez-Sevillano, Manuel Doblaré , Ana Martín-Calvo, and Sofía Calero

Molecular simulations have been used to investigate at the molecular level the suitability of zeolites with different topology on the adsorption, diffusion and separation of a nitrogen-sulfur hexafluoride mixture containing the latter at low concentration. This mixture represents the best alternative for the sulfur hexafluoride in industry since it reduces the use of this powerful greenhouse gas. A variety of zeolites are tested with the aim to identify the best structure for the recycling of sulfur hexafluoride in order to avoid its emission to the atmosphere and to overcome the experimental difficulties of its handling. Even though all zeolites show preferential adsorption of sulfur hexafluoride, we identified local structural features that reduce the affinity for sulfur hexafluoride in zeolites such as MOR and EON, providing exclusive adsorption sites for nitrogen. Structures such as ASV and FER were initially considered as good candidates based on their adsorption features. However, they were further discarded based on their diffusion properties. Regarding operation conditions for separation, the range of pressure that spans from $3x10^2$ to $3x10^3$ kPa was identified as the optimal to obtain the highest adsorption loading and the largest SF_6/N_2 selectivity. Based on these findings, zeolites BEC, ITR, IWW, and SFG were selected as the most promising materials for this particular separation.
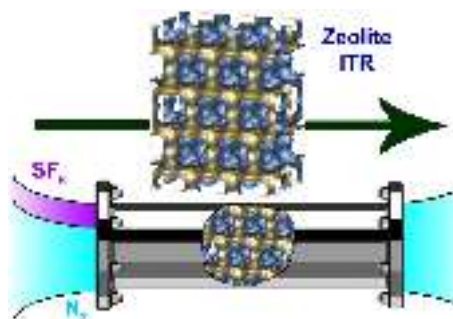
3.1 INTRODUCTION

Sulfur hexafluoride (SF_6) is an inorganic, colorless, odorless, nonflammable, and nontoxic gas with an octahedral structure in which a central sulfur atom is surrounded by six fluorine atoms. Besides its low toxicity, this gas also exhibits a high dielectric strength, arc-quenching properties, and high thermal and chemical stability. It is mainly used in the electrical industry as insulating gas for transmission and distribution of electrical energy [1, 2]. Sulfur hexafluoride is also used in aluminum and magnesium foundries, semiconductor manufacturing, inert solvent for supercritical fluid chemical reactions, and for medical applications such as ophthalmologic surgeries as inert gas [3] and as a contrast agent for ultrasound imaging to examine the vascularity of tumors [4]. As a result of its different uses, the global concentration of this gas has increased from less than 1 ppt in 1975 to about 7-8 ppt nowadays [5, 6]. From the environmental point of view sulfur hexafluoride is an efficient infrared absorber and a potent greenhouse gas with a global warming power about 23.900 times larger than this of CO_2 [7, 8]. Even with low concentration of SF_6 in the atmosphere the overall contribution to global warming is estimated to be about 0.2%, as a result of its high chemical stability and the fact that its atmospheric degradation is very slow. Sulfur hexafluoride is inert in the troposphere and the stratosphere and has

an estimated atmospheric lifetime of 800-3200 years [9]. Therefore its contribution to global warming is expected to be cumulative and quasipermanent. The worldwide goal is to reduce the absolute amount of sulfur hexafluoride as a consequence of its longterm effects on the environment. This gas was included in the Kyoto Protocol, which goal is to contain global emissions of the main anthropogenic gases. Additionally, in Europe, sulfur hexafluoride falls under the F-Gas directive which bans or controls its use for several applications. Hence, efficient methods are under development for handling and recovering sulfur hexafluoride after industrial usage, or to find an alternative gas for insulation of electrical equipment.

Among the methods for the treatment of sulfur hexafluoride, decomposition by plasma, electrical discharge, or spark are quite efficient methods but many undesirable wastes are produced as well [10, 11]. Some techniques based on catalytic decomposition are able to achieve ratios of decomposition similar to the formers but with fewer wastes [5, 12, 13]. Sulfur hexafluoride is also easy to recover due to its relatively high boiling point [14] (204.9 K at atmospheric pressure) that makes possible an effective liquefaction. However, for mixtures containing nitrogen and low concentration of SF_6 the compression pressure needed for its recovery raises from 2 MPa at room temperature to 20 MPa for contents lower than 10% of SF_6 in the mixture [15]. This increment of pressure

makes difficult the application of lique-faction procedures [16–18] though this is an interesting mixture as supposes a way to reduce the amount of SF_6 used while keeping all its properties [14]. As an alternative recovery method or as a way to increase the concentration of SF_6 in mixtures, adsorption in porous materials is an interesting option. The general idea is to capture the molecules of sulfur hexafluoride and exhaust the other component, nitrogen in this case, to the atmosphere using porous materials as molecular sieves.

There are some studies in the literature that report experimental and theoretical adsorption of sulfur hexafluoride in different porous materials such as zeolites [15, 19, 20], metal organic frameworks [21–23], carbon nanotubes [24, 25], or pillared clays [26, 27]. Besides, zeolites have been proved to be good candidates as molecular sieves [28, 29]. These materials exhibit a large variety of pore sizes and shapes as well as other interesting properties [30–32] (i.e. ordered structure, high surface area or thermal stability) to capture, separate or to purify mixtures containing small gases [33, 34]. Zeolites are aluminosilicates consisting of tetrahedral units with four oxygen atoms bonded to a central atom (T) that can be silicon, aluminum, or other four-fold coordinated metal. The tetrahedral basic units are connected via oxygen atoms, generating 3D structures with cages and/or channels giving a huge variety of possibilities difficult to screen experimentally. Addition-

ally, the strong restriction over the uses of SF_6 hinders even more their handling making a challenge to identify the most adequate material for the processes of interest (separation and/or capture).

We analyze the suitability of 41 zeolites for the adsorption of sulphur hexafluoride and its separation from a mixture containing nitrogen. This study is carried out using molecular simulations that overcome the serious limitations faced by experimentalists when dealing with this specific gas. As an additional contribution, we provide a reliable model for sulphur hexafluoride that reproduces the properties of this gas in the bulk as well as the few experimental studies on its adsorption in zeolites. The combination of geometric criteria with adsorption properties, structural features, and diffusion of themolecules inside the pores is an important strength of this work, offering consistent identification of the optimal structures as well as information about the most efficient operation conditions for this particular separation. The knowledge gained here will enable the scientific and industrial community to set the basis for the identification, design, and synthesis of structures with optimal performance on the separation of this particular - and difficult to handle - type of mixtures.

The information given in this paper is organized as follows. In Section 2 we describe the models for adsorbates and adsorbents, as well as the simulation techniques. In Section 3 we discuss the results

obtained from the force field parameterization of sulfur hexafluoride as well as the adsorption and diffusion obtained for the two molecules in each zeolite. Finally, in Section 4 we summarize some concluding remarks.

3.2 METHODS

Van der Waals interactions were described by 12-6 Lennard-Jones potential using a cutoff distance of 12 Å, where the interactions were truncated and shifted without tail corrections. Electrostatic interactions were considered by using Coulombic potentials and Ewald summations with a cutoff distance of 12 Å. These simulation conditions are commonly used to study the adsorption in confined systems [29, 33, 35]. For the molecule of nitrogen, we used a previous rigid model developed by Martin-Calvo *et al.* [36]. The symmetric structure of sulfur hexafluoride is also rigid with a bond length of 1.565 Å between the central sulfur atom and the fluorine atoms, while no charges were used. Lennard-Jones parameters for sulfur hexafluoride were obtained by fitting to the experimental Vapor-Liquid Equilibrium (VLE) curve [37]. Adsorbate-adsorbate van der Waals interactions are taken into account by Lorentz-Berthelot mixing rules [38].

We selected 41 zeolites with different geometry and topology from the International Zeolite Association (IZA) [39], considering the frameworks as rigid. The ef-

fect of zeolite flexibility in adsorption is usually small but it could play a role in the diffusivities. However, one should be cautious before using flexibility since diffusion values when flexibility is included strongly depend on the model used [40]. On the other hand we are not focusing here on the quantitative values for diffusivities but on removal of those zeolites in which the diffusion of sulfur hexafluoride is not fast enough. This selection is based not only in Molecular Dynamics simulations but also in the information of the pore limiting diameter provided by the IZA Structure Commission. In the absence of experimental data for comparison we are of the opinion that the use of rigid models in zeolites that are not suffering structural changes could lead to more reliable conclusions than the use of flexible models.

Adsorbate-adsorbent interactions were defined by those of the oxygen atoms of the framework (Ozeo) with the atoms of the adsorbed molecules. We used newly reported parameters to reproduce the interactions between the molecules of nitrogen and zeolites [41], while we provide parameters for sulfur hexafluoride. The set of charges of the frameworks was taken from Garcia-Sanchez *et al.* [42]. Details of the interaction parameters and models used are compiled in Table 1.

The selected structures were classified according to their channel system dimensionality (1-3 dimensional) and the ratio of the maximum diameter of a sphere that can be included and diffuse inside the

Table 1. Lennard-Jones parameters and partial charges of of the adsorbates and the adsorbents.

Atom 1	Atom 2	ε/k_B(K)	σ(Å)	Charge (e^-)
Adsorbed molecules				
F(SF$_6$)	F(SF$_6$)	73.130	2.843	—
S(SF$_6$)	S(SF$_6$)	—	—	—
N(N$_2$)	N(N$_2$)	38.298	3.306	-0.405
Site(N$_2$)	Site(N$_2$)	—	—	0.810
Zeolite				
O(Zeo)	O(Zeo)	—	—	-0.393
Si(Zeo)	Si(Zeo)	—	—	0.786
Zeolite – adsorbed molecules				
F(SF$_6$)	O(zeo)	80.304	2.962	—
S(SF$_6$)	O(zeo)	—	—	—
N(N$_2$)	O(zeo)	60.580	3.261	—
Site(N$_2$)	O(zeo)	—	—	—

zeolite [39]. Taking into account this ratio, each material was classified as either a channel or interconnected cage system, where an interconnected cage system is recognized by ratios up to 1.5, and channel system otherwise. We selected structures within each of these six classes to obtain representative sets: 1D channels (ASV, DON, CFI, ITW, JRY, LAU, LTL, MOR, PON), 2D channels (AFR, EON, FER, IWV, NES, SFO, SFG, TER), 3D channels (AFY, BEC, BOG, MEL, MFI, ITR, SBT, STW), 1D interconnected cages (ITE, MTF, SAS), 2D interconnected cages (DDR, LEV, MWW), 3D interconnected cages (CHA, EMT, ERI, FAU, LTA, KFI, OBW, PAU, RHO, SBE). Figure 1 shows the energy grid surface of representative structures of each group. Some characteristics of the zeolites, such as their unit cell lengths, pore volume, and surface area can be found in Table A2.1 in the Apendix 2.

Simulations were performed using RASPA [43]. We carried out Gibbs-ensemble Monte Carlo simulations to compute the VLE curve of sulfur hexafluoride [44]. During the simulations, the parameters were fitted to reproduce the experimental curve [37]. This is the first and the most important step for the performance of adsorption studies in porous systems [35, 42]. Monte Carlo simulations in the Canonical ensemble (CMC) were performed to compute isosteric heats of adsorption using the Widom test particle method [44]. These simulations were carried out in the limit of zero loading with only one molecule in the system and provide energies and entropies of adsorption at low loading. Adsorption isotherms were computed using Monte Carlo simulations in the Grand Canonical ensemble (GCMC), with fixed temperature, volume, and chemical potential. Chemical potential is associated to fugacity, and fugacity is directly related to pressure by the fugacity
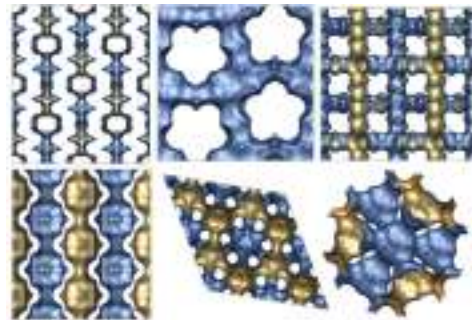
Figure 1. Energy grid surface of representative zeolites. Channels (top): 1D, 2D, and 3D - MOR, SFG, and MFI, respectively; interconnected cages (bottom): 1D, 2D, and 3D - SAS, DDR, and FAU, respectively. The accessible surface is colored in brown while the inaccessible surface is depicted in blue.

coefficient through the Peng-Robinson equation of state. Based on the type of gas and operating conditions, pressure can be equated to fugacity (coefficient = 1). To compare simulated and experimental adsorption isotherms, absolute adsorption has been converted to excess adsorption [39, 45]. To study diffusion properties of sulfur hexafluoride in the structures, self-diffusion in each zeolite was calculated through the slope of the Mean Square Displacements (MSD), obtained by Molecular Dynamics (MD) simulations in the canonical ensemble. MD simulations started from equilibrium conditions with two molecules in the system previously achieved using a short CMC simulation. In the MD, successive configurations of the system were generated by integrating Newton's laws of motion using the velocity-Verlet's algorithm. A Nosé–Hoover thermostat was used with a time scale on which the system thermostat evolves of 0.15 ps. Simulations run for 45.000 ps using an integration time step of $\tau = 5x10^4$ ps.

Sodalites and other cavities that are inaccessible from the main channel need to be blocked [46, 47]. To identify inaccessible cavities we use Monte Carlo and Molecular Dynamics simulations. The first method identifies energetic preferential adsorption sites and the second informs about the diffusion of these molecules. The sites on each structure from which the molecules were unable to escape after 0.15 ns were properly blocked. Blocking can be achieved by placing additional hard-

sphere particles inside the pockets that prevent adsorbates from accessing these pockets, or just using a list of geometric volume shape/sizes (e.g. spheres using an appropriate radius) that are automatically considered an overlap in Monte Carlo, either computed in advance or on-the-fly [48]. In RASPA, the blocking is implemented using a list of geometric descriptions of the inaccessible volumes. Some other properties of the structures such as surface area and pore volume were further computed for later analysis. Additional information about these methods can be found elsewhere [44].

3.3 RESULTS AND DISCUSSION

To reproduce the experimental VLE curve of a given molecules is of capital importance in adsorption studies [49]. As a first approach we compute this curve using the force field parameters of sulfur hexafluoride proposed by Pawley *et al.* [50], Pradip and Yashonath [51], and Dellis and Samios [52]. The critical parameters were predicted for all the models using the density scaling law and the law of rectilinear diameters [53–56] and are compiled in Table 2. We compare the results obtained using these three sets of parameters with experimental data from the National Instiute of Standards and Technology (NIST) [37]. This comparison is shown in Figure. 2. The first two models provide similar curves and good agreement with the experiments up to 240 K. However, the

Table 2. Critical parameters calculated for sulfur hexafluoride.

	T_C (K)	D_C (kg m^{-3})	P_C (MPa)
Experimental [37]	318.73	743.81	3.755
This work	314.83	743.541	3.529
Pawley *et al.* [50]	284.21	765.149	3.712
Pradip and Yashonath [51]	282.89	816.992	3.448
Dellis and Samios [52]	299.975	766.534	4.033
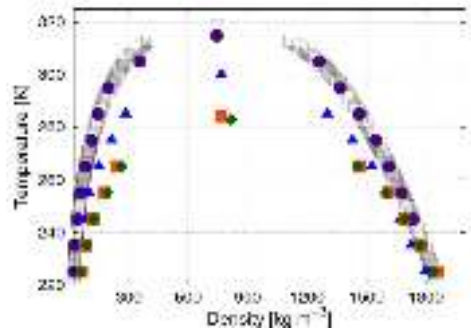
Figure 2. Vapor-liquid equilibrium curve of sulfur hexafluoride. Comparison of experiments (empty squares) [37] with the simulation values obtained using the force field parameters proposed by Dellis and Samios (blue triangles) [52], Pradip and Yashonath (green diamonds) [51], Pawley *et al.* (orange squares) [50], and the new set of parameters (purple circles).

curves obtained by simulation using these models deviate at higher temperatures, both in the liquid and in the vapor branches. The VLE curve obtained using the parameters proposed by Dellis and Samios [52] shows better agreement with the experiment in the vapor branch, but only for temperatures below 260 K. The agreement with experiments in the liquid branch is also reasonable up to this point. The three previous models highly underestimate the critical temperature (5-11%) and overestimate the critical density (3-

10%). Taking into account these results, we refitted the parameters given by Dellis and Samios [52] to reproduce the experimental curve and the critical parameters, obtaining a new set that is listed in Table 1. The values obtained with the new set of parameters are depicted as circles in Figure 2 and compiled in Table 2.

The parameters that we have developed to describe adsorbate-adsorbent interactions are also included in Table 1. These parameters were developed by fitting to the experimental adsorption isotherm of sulfur hexafluoride in MFI zeolite at 308 K and further validated for a range of temperature that spans from 277 K to 353 K. It should be mentioned that available experimental data of sulfur hexafluoride adsorption in nanoporous materials are rather scarce due to the difficulties of handling. Simulated and experimental adsorption isotherms of sulfur hexafluoride in MFI are shown in Figure 3. The figure shows the excellent agreement obtained for the calculated sulfur hexafluoride adsorption isotherms in MFI (277 K, 308 K, and 353 K) and available experimental data from Dunne *et al.* [57] (304.94 K) and from Sun *et al.* [19] (276.95 K, 307.95 K, and 352.75 K).

To validate the adsorbate-adsorbent interaction parameters, the isosteric heat of adsorption (Q_{st}) in the limit of zero coverage in MFI was computed at 305 K and compared with the experimental values from Cao and Sircar [20], Dunne *et al.* [57], and MacDougall *et al.* [58]. The

calculated heat of adsorption (34.47 kJ mol^{-1}) is in very good agreement with that obtained by Dunne *et al.* (34.40 kJ mol^{-1}) [57] and slightly overestimates the value given by MacDougall *et al.* (33.05 kJ mol^{-1}) [58]. Larger discrepancies are found with the heat of adsorption reported by Cao and Sircar (above 39 kJ mol^{-1}) [20]. These discrepancies can be attributed to the fact that the former studies measured the heats of adsorption for crystal samples whereas the latter used samples with binders.

The isosteric heats of adsorption of nitrogen and sulfur hexafluoride were computed for all zeolites to evaluate the strength of the interaction of the two molecules with the structures. Direct comparison (shown in Figure 4) can be used as a rough estimation of the affinity of the different zeolites for one component over the other. As expected from the difference in size of the two molecules (the kinetic diameters of SF$_6$ and N$_2$ are 5.128 Å, and 3.64-3.80 Å, respectively), the heat of adsorption obtained for sulfur hexafluoride in all zeolites is higher in absolute number than that obtained for nitrogen. The energy due to the size of the molecule predominates over Columbic energy considering that we use a non-charged model for sulfur hexafluoride, while nitrogen has a molecular quadrupole moment of 1.17 D Å (reproducing the experimental value) [36]. Only ITW and JRY do not follow the general trend exhibiting lower values of heat of adsorption for sulfur hexafluoride than for nitrogen. This is not depicted in the figure because the ratio between heats of adsorption is lower than 1. The low values of heat of adsorption for sulfur hexafluoride in ITW (-4.43 kJ mol^{-1}) and JRY (-10.02 kJ mol^{-1}) zeolites indicate that sulfur

Figure 3. Comparison of simulated (closed symbols) and experimental (open symbols) adsorption isotherms of sulfur hexafluoride in MFI at 277 K (blue), 308 K (green), and 353 K (purple) from Sun *et al.* [19]; and at 304.94 K (green diamonds) from Dunne *et al.* [57].

Figure 4. Isosteric heats of adsorption of sulfur hexafluoride and nitrogen in a variety of zeolites at 298 K. Open symbols show the results obtained for channel-type zeolites and closed symbols for the interconnected-type zeolites. The directionally of the pore space is represented by circles (1D), down triangles (2D), and squares (3D).

hexafluoride is not adsorbed in these ze-
olites. Therefore, since the aim of this
work is to find structures for the selective
capture of sulfur hexafluoride we discard
these two structures from further analy-
sis.

ASV and FER show the highest heat
of adsorption for both sulfur hexafluoride
(above -45 kJ mol^{-1}) and nitrogen (about
-18 kJ mol^{-1}), affecting the selective ad-
sorption. On the other hand, in EON, MOR
and SBE the ratio between heats of adsorp-
tion (SF$_6$/N$_2$) seems to be the lowest. The
heats of adsorption of sulfur hexafluoride
and nitrogen as a function of the pore vol-
ume of the zeolites are depicted in Figure
A2.1 and A2.2 in the Appendix 2. As a gen-
eral rule, we find that the lower the pore
volume of the zeolites the highest the heat
of adsorption, both for sulfur hexafluoride
and nitrogen.

For a better understanding of the ad-
sorption selectivity at low loading, the ra-
tio between the heats of adsorption of both
gases (sulfur hexafluoride over nitrogen)
as a function of the pore volume of each
zeolite is also depicted in Figure 5. This
figure confirms that AFY, EON, MOR and
SBE are the worst candidates for the sep-
aration if we base the analysis only on
the adsorption properties at low loading.
The strength of the SF$_6$-zeolite interaction
is less than twice the N$_2$-zeolite interac-
tion in these four zeolites since some local
structure features dominate the adsorp-
tion behavior [59]. To shed light on this
behavior we computed average occupation
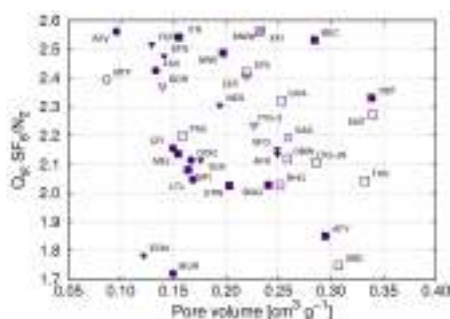
Figure 5. Ratio of the isosteric heats of
adsorption of sulfur hexafluoride and ni-
trogen at 298 K as a function of the pore
volume of the structures. Open symbols
show the results obtained for channel-
type zeolites and closed symbols for the
interconnected-type zeolites. The directionality
of the pore space is represented by circles
(1D), down triangles (2D), and squares (3D).

profiles of the gases inside the pores of the
zeolites (Figures A2.3, A2.4, A2.6, and
A2.7 in the Apendix 2).

Zeolite MOR consists of parallel chan-
nels with small side-pockets that are
preferential sites of adsorption for small
molecules such as CO$_2$, CO or N$_2$ [29]. The
average occupation profile (Figure A2.3 in
the Apendix 2) reveals that the molecules
of nitrogen tend to adsorb preferentially
in these pockets while sulfur hexafluoride
is only adsorbed in the main straight chan-
nels as the size of the gate ring prevents
them to enter the pockets (limiting diam-
eter 3.4 *x* 4.8 Å) [39]. The confinement
of the molecules of nitrogen in the side-
pockets explains the large values obtained
for the heat of adsorption in comparison
with those of sulfur hexafluoride (adsorbed
in the big main channels). This explana-

tion could be extended to EON too since this structure also has side-pockets where only nitrogen is able to enter, while sulfur hexafluoride is adsorbed in the main channels (Figure A2. 4 in the Apendix 2). Additionally, in this structure, triangular cages connecting side-pockets are found, but are not accessible for molecules with a diameter larger than 3.6 Å, excluding therefore both molecules (Figure A2. 5 in the Apendix 2). In SBE the main channels where the molecules can go through are located in the x and y axes, but there are secondary channels in the z-axis. The gate to enter these channels is a 8-member ring window with a limiting diameter of 4.0 Å. Therefore, the access is blocked for sulfur hexafluoride while nitrogen can go inside this channels, being the molecule-zeolite interaction stronger than in the main channels (Figure A2. 6 in the Apendix 2). We observe the same behavior in the AFY zeolite. This structure consists of a main wide channel along the z-axis (6.1 Å) that is interconnected by secondary narrow channels along the other two axes through 8-member ring opening windows with a limiting diameter of 4 Å where only nitrogen can fit (Figure A2. 7 in the Apendix 2). Suitable blocks were applied in our simulations to avoid the access of molecules to parts of the structures where they are unable to enter experimentally.

The structures in which the interaction of sulfur hexafluoride with the zeolite is more than two and a half times stronger than the interaction of nitro-

gen with the zeolite are highlighted as good candidates for the separation process regarding adsorption properties at low loading. These structures are: ASV, FER, ITR, IWW, MWW, KFI, BEC, and SFG. In further discussion we also take into account diffusion and adsorption properties at medium and high coverage and we will compare our findings with these preliminary results.

It is well known that molecular transport inside the pores plays a key role in many applications of nanoporous materials and synergies between molecular adsorption and diffusion in zeolites for separation processes has been established using both simulations and experiments [60]. Some zeolites considered as good candidates based on their adsorption properties could be further discarded due to poor diffusion of the molecules. Therefore we carried out additional MD simulations to analyze the mean square displacement (MSD) of sulfur hexafluoride (the bulkiest molecule under study) in each zeolite at low loading (2 molecules per simulation cell). Figure 6 shows the MSD obtained in ASV, BEC, FER, and ITR zeolites. For ASV and FER, the slope of the MSD at long times, where the molecules reach the diffusional regime, is almost flat, indicating that sulfur hexafluoride diffusion is not allowed in these zeolites. Consequently, we discarded these structures despite the fact that they showed high values of heat of adsorption for sulfur hexafluoride. BEC and ITR were also pointed out as good candi-
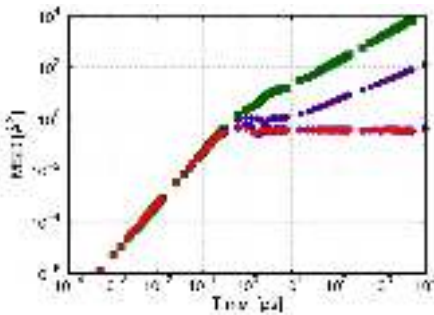
Figure 6. Mean square displacement (MSD) of sulfur hexafluoride in ASV (blue circles), FER (red down triangles), BEC (green squares), and ITR (purple diamonds) zeolites. Simulations were computed at room temperature with two molecules per simulation cell.

shows a non-flat slope from MSD of sulfur hexafluoride in these two zeolites implying that the diffusion of sulfur hexafluoride is permitted in their 3D system. Self-diffusion coefficients for all the zeolites are included in Table A2. 2 in the Apendix 2 .

The final set of available zeolites after discarding those in which diffusion of SF_6 is inhibited is: AFR, AFY, BEC, BOG, CFI, DON, EMT, EON, FAU, ITR, IWW, LTL, MEL, MFI, MOR, NES, OBW, SBE, SBT, SFG, SFO, STW, and TER. We computed adsorption isotherms in these structures for binary mixtures containing sulfur hexafluoride (10%) and nitrogen (90%) at room temperature. Figure 7 shows the

dates for the separation process based on the computed heats of adsorption. Figure 6
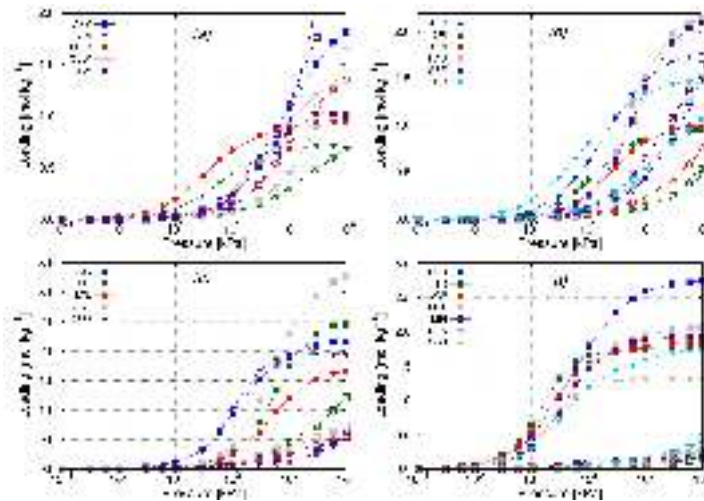
Figure 7. Computed adsorption isotherms from the binary mixture SF_6/N_2 (0.1:0.9) at room temperature in (a) AFY, EON, MOR, OBW, and STW; (b) AFR, CFI, DON, FAU, SBE, and TER; (c) BOG, EMT, LTL, SBT, and SFO; and (d) BEC, ITR, IWW, MEL, MFI, NES, and SFG zeolites. Isotherms of SF_6 are depicted as full symbols and lines and those of N_2 as empty symbols and dotted lines. The directionality of the pore space is represented by circles (1D), down triangles (2D), and squares (3D).

adsorption isotherms of the mixture classified in four groups according to the general trend of adsorption.

Figure 7a shows the values obtained for AFY, EON, MOR, OBW, and STW. In these zeolites the adsorption of sulfur hexafluoride starts at 10 kPa, almost simultaneously than nitrogen adsorption. However loadings of sulfur hexafluoride are larger up to 10^3 kPa. At higher values of pressure we observe an increase in the adsorption of nitrogen that keeps the loading of sulfur hexafluoride almost independent of pressure. The effect is less visible in AFY because this zeolite has the largest pore volume of this group and the competition for available space in the zeolite is not so strong. We already pointed out AFY, EON, and MOR as poor candidates for the separation processes based on the heats of adsorption and due to the existence of sites and channels only accessible for small molecules. These sites or channels allow nitrogen to be adsorbed at low pressure (10 kPa) without competition with sulfur hexafluoride. Furthermore, at higher pressure nitrogen is also able to compete and even displace sulfur hexafluoride from the accessible pore volume for both molecules. In this group of zeolites we found saturation loadings of 0.5-2 mol kg^{-1} for sulfur hexafluoride, but the selectivity is expected to be low since the loading of nitrogen is similar or larger than the loading for sulfur hexafluoride at high pressure.

Figure 7b depicts the adsorption isotherms obtained for AFR, CFI, DON, FAU, SBE, and TER zeolites. The adsorption of sulfur hexafluoride starts between 10 and 10^2 kPa, while nitrogen enters the structures at 10^2 kPa. Above 10^3 kPa we observe a displacement of the molecules of SF_6 by the molecules of nitrogen, but the loading of sulfur hexafluoride remains about 0.5 mol kg^{-1} higher than the loading of nitrogen at 10^4 kPa. The isotherms calculated for BOG, EMT, LTL, SBT, and SBO zeolites are shown in Figure 7c. The adsorption performance of sulfur hexafluoride in this group of zeolites is similar to that observed in Figure 7b, but the adsorption of adsorption nitrogen is now lower. Therefore, loadings of both molecules at the highest pressure of study (10^4 kPa) differ in about 1-2 mol kg^{-1}. We found saturation loadings for sulfur hexafluoride between 1-2 mol kg^{-1} (Figure 7b) and 1.5-3.5 mol kg^{-1} (Figure 7c) and selectivity in favor of this molecule is expected to be larger in the latter group.

The isotherms from the last group of zeolites are depicted in Figure 7d (BEC, ITR, IWW, MEL, MFI, NES, and SFG). The main characteristic of this group is the very low adsorption of nitrogen in the range of pressure under study (10^{-1}-10^4 kPa). Sulfur hexafluoride enters the structures at 1 kPa. At this value of pressure the adsorption of nitrogen is lower than 0.5 mol kg^{-1} in all zeolites. Therefore zeolites of this group could be good candidates for selective capture of sulfur hexafluoride, as we pointed out before based on heat of

adsorption for ITR, IWW, BEC y SFG.

For a deeper understanding of the selective behavior of the studied zeolites we calculated adsorption selectivities of SF_6 over N_2 according to the expression $(x_{SF_6}/y_{N_2})/(x_{N_2}/y_{SF_6})$ where x is the molar fraction in the adsorbed phase and y the molar fraction in the bulk phase. Figure 8 shows the values of selectivity obtained from the mixture (0.1 : 0.9) at room temperature in a range of pressure that spans from 0.1 to 10^4 kPa. As a general rule, selectivity remains constant up to 10 kPa, where the loadings of both molecules are still very low. Above 10 kPa, the slope of the selectivity is still flat in most zeolites

and only increases for SFO, ITR, IWW and SFG whereas the adsorption of nitrogen reduces the selectivity at high pressure (10^2-10^3 kPa).

Using the same classification that we made for adsorption isotherms, zeolites shown in Figure 8a exhibit the lowest selectivities. EON and MOR have high selectivity at low pressure, but the loading of sulfur hexafluoride is almost negligible (less than 0.25 mol kg^{-1} at 10 kPa). The selectivity drops drastically after this pressure, where the adsorption of sulfur hexafluoride is still very low. Increasing pressure up to 10^3 kPa the loading of sulfur
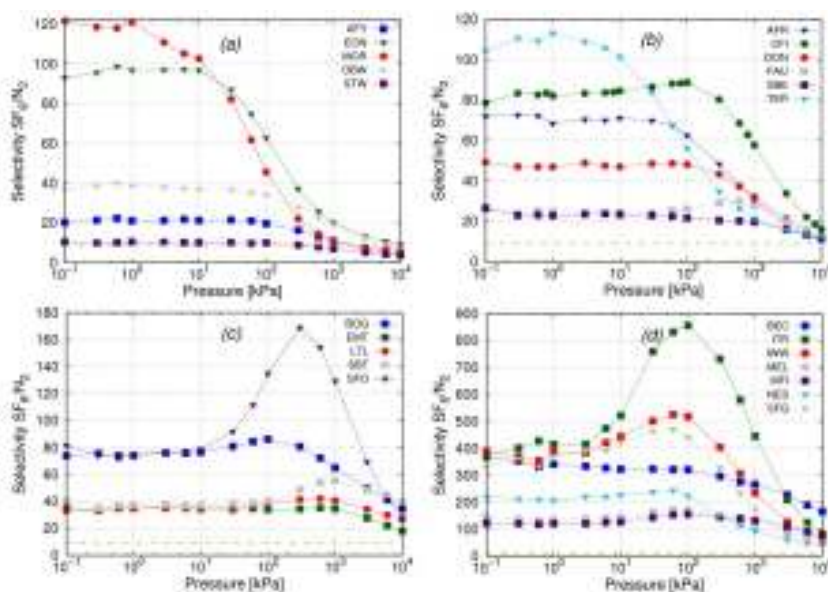
Figure 8. Adsorption selectivity SF_6/N_2 from the binary mixture SF_6/N_2 (0.1:0.9) at room temperature in (a) AFY, EON, MOR, OBW, and STW; (b) AFR, CFI, DON, FAU, SBE, and TER; (c) BOG, EMT, LTL, SBT, and SFO; and (d) BEC, ITR, IWW, MEL, MFI, NES, and SFG zeolites. The directionality of the pore space is represented by circles (1D), down triangles (2D), and squares (3D). The inversion in the selective behavior is represented by an orange dotted line.

hexafluoride in these zeolites reaches about 1 mol kg^{-1} but at this pressure they do not show preferential adsorption for sulfur hexafluoride. In Figure 8b it can be seen that the selectivity in favor of sulfur hexafluoride is constant up to 10^2-10^3 kPa but with larger values than those depicted in Figure 8a as a result of the lower adsorption of nitrogen. As shown in the previous figure, at the highest pressure the selectivity is reduced due to the displacement of the molecules of SF_6 by those of N_2.

In Figure 8c there are two zeolites (BOG and SFO) exhibiting twice the selectivity than the rest of the group in the range of pressure that spans from 10 to 10^2 kPa. Above the latter value of pressure the selectivity in SFO increases again and then drops (at 300 kPa) with more than 1.5 mol kg^{-1} for SF_6 while nitrogen requires higher pressure to enter the zeolite. Finally the low adsorption of nitrogen observed for zeolites depicted in Figure 7d (less than 0.5 mol kg^{-1}) makes these structures the best candidates to achieve the largest selectivities in favor of sulfur hexafluoride (Figure 8d).

As can be seen in Figure 8, the largest selectivity in favor of sulfur hexafluoride is obtained at 10^2-10^3 kPa. Therefore in Figure 9 we depict the selectivity obtained for the zeolites at $3x10^2$ kPa as a function of zeolite pore volume, and loading of sulfur hexafluoride. We selected this pressure using a criterion that combines both high selectivity and loading of the molecule of
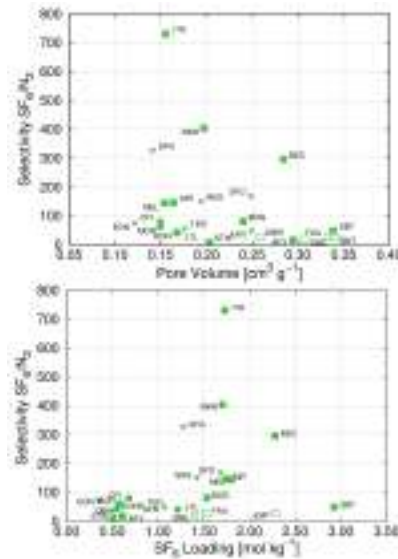
Figure 9. Adsorption selectivity SF_6/N_2 from the binary mixture SF_6/N_2 (0.1:0.9) at room temperature as a function of (top) zeolite pore volume and (bottom) loading of sulfur hexafluoride. Open symbols show the results obtained for channel-type zeolites and closed symbols for the interconnected-type, being the directionality of the pore space represented by circles (1D), down triangles (2D), and squares (3D). Selectivity is calculated at the pressure with higher selectivity and loading of SF_6 for each structure.

interest (SF_6). As an exception, we focused on $3x10^3$ kPa for EMT, LTL, SBT, FAU, and SBE and 3-6$x10^1$ kPa for TER, EON, and MOR (see Table A2. 3 in the Apendix 2). The zeolite with the largest selectivity in favor of sulfur hexafluoride is ITR, followed by IWW, SFG and BEC. The high selectivity of this structure can be attributed to the topology. ITR consists of straight channels along the x-axis interconnected by zig-zag channels. The size of these channels (5.12 Å) is very close to the kinetic di-

ameter of SF_6 and therefore this molecule is commensurate with the pore leading to saturation at 10^2 kPa when nitrogen is not yet adsorbed. A similar explanation could be used for SFG, but its lower pore volume lowers the saturation loading of SF_6 and consequently its selectivity. The adsorption of SF_6 in these zeolites is about 1-2.5 mol kg^{-1}, BEC being the zeolite with the largest saturation capacity in this group. This is due to the high pore volume that makes this zeolite the best candidate for storage. SBT zeolite could also be used in a second stage as a storage material with a pore volume of 0.35 cm^3 g^{-1}, but its selectivity is very low compared to that of the other remarked zeolites.

Although to find a relationship between the framework topology of the zeolites and the selectivity of sulfur hexafluoride is not straight forward, we observed that the separation of the mixture SF_6/N_2 is more efficient using zeolites with intersecting channels accessible to the two molecules. These accessible channels should cross forming intersections of a minimum of 6.3 Å and a maximum of 7.1 Å in diameter. These patterns were exhibited by the 2-dimensional structures ITR and SFG and the 3-dimensional structures BEC and IWW.

3.4 CONCLUSIONS

We used molecular simulations to evaluate the suitability of zeolites as molecular sieves to separate sulfur hexafluoride from nitrogen. The prediction of zeolites for this separation was based on the adsorption and diffusion performance. At low loading the largest molecule, i.e. sulfur hexafluoride, exhibits the strongest interaction with all selected zeolites. The adsorption of nitrogen increases with the pressure being $3x10^2 - 3x10^3$ kPa, the best range for selective adsorption of sulfur hexafluoride over nitrogen. At these values of pressure sulfur hexafluoride reaches saturation while nitrogen is starting to be adsorbed. Isosteric heats of adsorption confirm the preferential adsorption of sulfur hexafluoride at low loading. Our results show that local structure features dominate the strength of adsorption in zeolites such as MOR, EON, SBE, and AFY, providing exclusive adsorption sites for nitrogen that reduce the affinity for sulfur hexafluoride. Therefore, the selectivity over sulfur hexafluoride in these structures is the lowest of the studied zeolites. Based only on the heats of adsorption we pointed out zeolites ASV, FER, ITR, IWW, MWW, KFI, BEC, and SFG as good candidates for the separation processes. However, zeolites ASV, FER, MWW, and KFI were discarded due to the slow diffusion of sulfur hexafluoride in their pores. Based on the combination of good performance on adsorption and diffusion we point out zeolites BEC, ITR, IWW, and SFG as the most efficient candidates for the selective capture of sulfur hexafluoride from this particular mixture.

3.5 Bibliography

[1] Christophorou, L. G.; Van Brunt, R. J. *IEEE Transactions on Dielectrics and Electrical Insulation* **1995**, *2*, 952–1003.

[2] Builes, S.; Roussel, T.; Vega, L. F. *AIChE Journal* **2011**, *57*, 962–974.

[3] De Alba, F. *J. Am. Med. Assoc.* **2010**, *303*, 1204.

[4] Lassau, N.; Chami, L.; Benatsou, B.; Peronneau, P.; Roche, A. *European radiology* **2007**, *17 Suppl 6*, 89–98.

[5] Zhang, J.; Zhou, J. Z.; Liu, Q.; Qian, G.; Xu, Z. P. *Environmental science & technology* **2013**, *47*, 6493–6499.

[6] Rigby, M. et al. *Atmospheric Chemistry and Physics* **2010**, *10*, 10305–10320.

[7] Cha, I.; Lee, S.; Lee, J. D.; Lee, G.-W.; Seo, Y. *Environmental Science & Technology* **2010**, *44*, 6117–6122.

[8] Houghton, J. T.; Meira Filho, L. G.; Callander, B. A.; Harris, N.; Kattenberg, A.; Maskell, K. In *Intergovernmental Panel on Climate Change (IPCC)*; Press, C. U., Ed.; Cambridge University Press: Cambridge, U. K., 1996; pp 23–28.

[9] Maiss, M.; Brenninkmeijer, C. A. M. *Environmental Science & Technology* **1998**, *32*, 3077–3086.

[10] Tsai, C.-H.; Shao, J.-M. *Journal of Hazardous Materials* **2008**, *157*, 201–206.

[11] Radoiu, M.; Hussain, S. *Journal of Hazardous Materials* **2009**, *164*, 39–45.

[12] Song, X.; Liu, X.; Ye, Z.; He, J.; Zhang, R.; Hou, H. *Journal of Hazardous Materials* **2009**, *168*, 493–500.

[13] Yamada, Y.; Tamura, H.; Takeda, D. *The Journal of Chemical Physics* **2011**, *134*, 104302.

[14] Christophorou, L.; Olthoff, J.; Green, D. *Gases for Electrical Insulation and Arc Interruption: Possible Present and Future Alternatives to Pure SF6*; Boulder, CO, NIST Tech. Note 1425, 1997; p 48.

[15] Toyoda, M.; Murase, H.; Imai, T.; Naotsuka, H.; Kobayashi, A.; Takano, K.; Ohkuma, K. **2003**, *18*, 442–448.

[16] Yamamoto, O.; Takuma, T.; Kinouchi, M. *Electrical Insulation Magazine, IEEE* **2002**, *18*, 32–37.

[17] Hama, H.; Yoshimura, M.; Inami, K.; Hamano, S. *Gaseous Dielectrics VIII*; Springer US, 1998; Chapter 48, pp 353–359.

[18] Inami, K.; Maeda, Y.; Habuchi, Y.; Yoshimura, M.; Hamano, S.; Hama, H. *Electrical Engineering in Japan* **2001**, *137*, 25–31.

[19] Sun, M. S.; Shah, D. B.; Xu, H. H.; Talu, O. *The Journal of Physical Chemistry B* **1998**, *102*, 1466–1473.

[20] Cao, D. V.; Sircar, S. *Adsorption* **2001**, *7*, 73–80.

[21] Senkovska, I.; Barea, E.; Navarro, J. A. R.; Kaskel, S. *Microporous and Mesoporous Materials* **2012**, *156*, 115–120.

[22] Chowdhury, P.; Bikkina, C.; Gumma, S. *The Journal of Physical Chemistry C* **2009**, *113*, 6616–6621.

[23] Chowdhury, P.; Bikkina, C.; Meister, D.; Dreisbach, F.; Gumma, S. *Microporous and Mesoporous Materials* **2009**, *117*, 406–413.

[24] Chiang, Y. C.; Wu, P. Y. *Journal of Hazardous Materials* **2010**, *178*, 729–738.

[25] Furmaniak, S.; Terzyk, A. P.; Gauden, P. A.; Kowalczyk, P. *Microporous and Mesoporous Materials* **2012**, *154*, 51–55.

[26] Jagiełło, J.; Bandosz, T. J.; Schwarz, J. A. *Langmuir* **1997**, *13*, 1010–1015.

[27] Bandosz, T. J.; Jagiełło, J.; Schwarz, J. A. *Journal of Chemical & Engineering Data* **1996**, *41*, 880–884.

[28] Himeno, S.; Tomita, T.; Suzuki, K.; Nakayama, K.; Yajima, K.; Yoshida, S. *Industrial & Engineering Chemistry Research* **2007**, *46*, 6989–6997.

[29] Garcia-Perez, E.; Parra, J. B.; Ania, C. O.; Garcia-Sanchez, A.; Van Baten, J. M.; Krishna, R.; Dubbeldam, D.; Calero, S. *Adsorption* **2007**, *13*, 469–476.

[30] Romero, M. D.; Ovejero, G.; Rodríguez, A.; Gómez, J. M. *Microporous and Mesoporous Materials* **2005**, *81*, 313–320.

[31] Altshuler, G. N.; Shkurenko, G. Y. *Bulletin of the Academy of Sciences of the USSR Division of Chemical Science* **1990**, *39*, 1331.

[32] Anerousis, J. P. *Chemical Engineering* **1976**, *83*, 128.

[33] Matito-Martos, I.; Martin-Calvo, A.; Gutiérrez-Sevillano, J. J.; Haranczyk, M.; Doblare, M.; Parra, J. B.; Ania, C. O.; Calero, S. *Phys. Chem. Chem. Phys.* **2014**, *16*, 19884–19893.

[34] Bernal, M. P.; Coronas, J.; Menendez, M.; Santamaria, J. *AIChE Journal* **2004**, *50*, 127–135.

[35] Calero, S.; Martin-Calvo, A.; Hamad, S.; Garcia-Perez, E. *Chemical Communications* **2011**, *47*, 508–510.

[36] Martin-Calvo, A.; Garcia-Perez, E.; Garcia-Sanchez, A.; Bueno-Perez, R.; Hamad, S.; Calero, S. *Physical Chemistry Chemical Physics* **2011**, *13*, 11165–11174.

[37] National Institute of Standards and Technology. http://www.nist.gov/index.html.

[38] Allen, M. P.; Tildesley, D. J. *Computer Simulation of Liquids*; Oxford Clarendon Press: Oxford, 1987.

[39] Baerlocher, C.; McCusker, L. B.; Olson, D. *Atlas of Zeolite Framework types*, 6th ed.; Elsevier: London, 2007.

[40] Garcia-Sanchez, A.; Dubbeldam, D.; Calero, S. *Journal of Physical Chemistry C* **2010**, *114*, 15068–15074.

[41] Martin-Calvo, A.; Gutierrez-Sevillano, J. J.; Parra, J. B.; Ania, C. O.; Calero, S.; Gutiérrez-Sevillano, J. J.; Parra, J. B.; Ania, C. O.; Calero, S. *Phys. Chem. Chem. Phys.* **2015**, *17*, 24048–24055.

[42] Garcia-Sanchez, A.; Ania, C. O.; Parra, J. B.; Dubbeldam, D.; Vlugt, T. J. H.; Krishna, R.; Calero, S. *Journal of Physical Chemistry C* **2009**, *113*, 8814–8820.

[43] Dubbeldam, D.; Calero, S.; Ellis, D. E.; Snurr, R. Q. *Molecular Simulation* **2016**, *42*, 81–101.

[44] Frenkel, D.; Smit, B. *Understanding Molecular Simulations: From Algorithms to Applications*, second edi ed.; C. Academic Press: San Diego, CA, 2002.

[45] Duren, T.; Sarkisov, L.; Yaghi, O. M.; Snurr, R. Q.

Langmuir **2004**, *20*, 2683–2689.

[46] Calero, S.; Dubbeldam, D.; Krishna, R.; Smit, B.; Vlugt, T. J. H.; Denayer, J. F. M.; Martens, J. A.; Maesen, T. L. M. *Journal of the American Chemical Society* **2004**, *126*, 11377–11386.

[47] Krishna, R.; van Baten, J. M. *Langmuir* **2010**, *26*, 2975–2978.

[48] Kim, J.; Martin, R. L.; Rubel, O.; Haranczyk, M.; Smit, B. *Journal of Chemical Theory and Computation* **2012**, *8*, 1684–1693.

[49] Martin-Calvo, A.; Lahoz-Martin, F. D.; Calero, S. *Journal of Physical Chemistry C* **2012**, *116*, 6655–6663.

[50] Pawley, G. S. *Molecular Physics* **1981**, *43*, 1321–1330.

[51] Ghorai, P. K.; Yashonath, S. *Journal of Chemical Physics* **2004**, *120*, 5315–5321.

[52] Dellis, D.; Samios, J. *Fluid Phase Equilibria* **2010**, *291*, 81–89.

[53] Rowlinson, J. S.; Swinton, F. L. *Liquids and Liquid Mixtures*; Butterworths: London, 1982.

[54] Rowlinson, J.; Widom, B. *Molecular Theory of Capillarity*; Oxford University Press: New Yoek, 1989.

[55] Atkins, P. W. *Physical Chemistry*; Oxford Higher Education: New York, 1990.

[56] Martin, M. G.; Siepmann, J. I. *The Journal of Physical Chemistry B* **1998**, *102*, 2569–2577.

[57] Dunne, J. A.; Mariwala, R.; Rao, M.; Sircar, S.; Gorte, R. J.; Myers, A. L. *Langmuir* **1996**, *12*, 5888–5895.

[58] MacDougall, H., Ruthven; Brandani, S. *Adsorption* **1999**, *5*, 369–372.

[59] Martin, R. L.; Willems, T. F.; Lin, L. C.; Kim, J.; Swisher, J. A.; Smit, B.; Haranczyk, M. *Chemphyschem* **2012**, *13*, 3595–3597.

[60] Titze, T.; Chmelik, C.; Kärger, J.; van Baten, J. M.; Krishna, R. *The Journal of Physical Chemistry C* **2014**, *118*, 2660–2665.

Adsorption Equilibrium of Nitrogen Dioxide in Porous Materials

Ismael Matito-Martos, Ahmadreza Rahbari, Ana Martín-Calvo, David Dubbeldam, Thijs J. H. Vlugt, and Sofía Calero

The effect of confinement on the equilibrium reactive system containing nitrogen dioxide and dinitrogen tetroxide is studied by molecular simulation and the reactive Monte Carlo (RxMC) approach. The bulk-phase reaction was successfully reproduced and five all-silica zeolites (i.e. FAU, FER, MFI, MOR, and TON) with different topologies were selected to study their adoption behavior. Dinitrogen tetroxide showed a stronger affinity than nitrogen dioxide in all the zeolites due to size effects, but exclusive adsorption sites in MOR allowed the adsorption of nitrogen dioxide with no competition at these sites. From the study of the adsorption isotherms and isobars of the reacting mixture, confinement enhanced the formation of dimers over the full range of pressure and temperature, finding the largest deviations from bulk fractions at low temperature and high pressure. The channel size and shape of the zeolite have a noticeable influence on the dinitrogen tetroxide formation, being more important in MFI, closely followed by TON and MOR, and finally FER and FAU. Preferential adsorption sites in MOR lead to an unusually strong selective adsorption towards nitrogen dioxide, demonstrating that the topological structure has a crucial influence on the composition of the mixture and must be carefully considered in systems containing nitrogen dioxide.
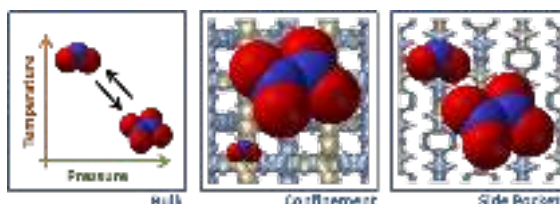
4.1 INTRODUCTION

Nitrogen oxides (NO_x) refer to a mixture of compounds containing nitrogen and oxygen. However, this term usually refers to NO, NO_2, and N_2O, due to their larger relative amounts and the fact that the others are unstable and do not appear in the atmosphere [1, 2]. Dinitrogen oxide (N_2O) is a non-toxic gas that mainly comes from the natural microbial denitrification of organic matter [3]. Conversely, the source of nitrogen monoxide (NO) and nitrogen dioxide (NO_2) is mainly anthropogenic, being produced in combustion processes, especially at high temperature. Internal combustion engines are their most important sources [4] along with thermal power stations [5]. In these processes, excess air used to complete the combustion leads to formation of NO_x in the combustion products. In addition, nitrogen oxides are intermediates in some chemical processes such as the fabrication of nitric acid, paints, nitration of organic chemicals, manufacture of explosives, or as rocket fuels [1]. NO and NO_2 have a high reactivity with the oxygen from air, being of capital importance in atmospheric chemistry. These gases are the main precursors of tropospheric ozone and other secondary pollutants when they react with oxide volatile organic compounds in the presence of sunlight. They are also responsible for acid rain when combined with water vapor [6, 7]. The release of NO_x from combustion also favors photochemical reactions resulting in the well-known photochemical smog. Additionally, nitrogen oxides are toxic to human inhalation.

The important effects on the environment and human health, along with increasing pollution, leads to the establishment of more restrictive levels of emissions and the need for the appropriate methods to reduce and control the emissions of nitrogen oxides. In order to achieve this aim, there are two main approaches. One focuses on the combustion process itself trying to reduce the amount of NO_x produced. This type of solution achieves ratios of decomposition below 50% in most cases [8]. The second strategy is based on post-combustion solutions focused on the capture and removal of NO_x after being produced from the combustion products. Among different methods, selective catalytic reduction (SCR) is one of the solutions with higher decomposition ratios while no wastes are produced [8, 9]. The capture and removal of NO and NO_2 is not only an interesting subject in itself but also has importance in carbon dioxide capture and storage processes (CCS). Traces of NO_x and other gases such as sulphur oxides (SO_x) strongly influence the capture and removal of CO_2 [10–13]. As an alternative technology for the removal of NO_x and other pollutants with a better efficiency than SCR processes, adsorption in porous materials is an interesting option. With this method, wastes are not produced and the energy requirements are low [13–16]. The key point for the capture and removal of targeted pollutants is the identification

of suitable materials and operation conditions. Zeolites have proved to be efficient molecular sieves for the capture, separation, and purification of mixtures containing small gas molecules [13, 17, 18]. These materials exhibit many interesting properties such as a large variety of pore sizes and shapes or high thermal stabilities [19]. Zeolites consist of basic tetrahedral units, in which a central T-atom (usually silicon) is bonded to four oxygen atoms. The basic units are connected generating 3D structures with a huge variety of topologies (i.e. cages and/or channels with different directionality) whose effect on the adsorption performance is difficult to screen experimentally. The large amount of available zeolite topologies [20] gives to molecular simulations capital importance as a powerful tool to evaluate the performance of porous material and gases at a molecular level with low cost associated [21–23].

Simulating systems containing nitrogen monoxide and nitrogen dioxide becomes challenging as these gases co-exist as an equilibrium mixture of their monomer and dimer, depending on the temperature and pressure conditions. The properties of the equilibrium mixtures NO/N_2O_2 and NO_2/N_2O_4 have been extensively studied experimentally and theoretically [24–36]. For both equilibrium reactions, association is favored at higher values of pressure and low temperature, following Le Chatelier's principle for endothermic dissociation reactions. In the case of the NO/N_2O_2 equilibrium mixture,

the fraction of the dimer in the gas phase is very small (less than 3% at temperatures below 180 K and room pressure), and therefore its contribution can be neglected at temperatures above room temperature [25, 26]. The NO_2/N_2O_4 reaction was studied by James and Marshal in the liquid and solid states, reporting equilibrium constants from 77 to 295 K with N_2O_4 fractions larger than 0.99 at temperatures between 250-295 K (strong association in the liquid phase) [33]. The gas phase reaction was studied by Chao *et al.* [32], Yoshino *et al.* [30], Verhoek *et al.* [31], and Harris and Kenneth [37], among others. These studies show a NO_2 mole fraction in the vapor phase of around 0.9 at 373.15 K and complete dissociation at 413.15 K. The mole fraction of dinitrogen tetroxide rapidly decreases as the pressure decreases or temperature increases. However, dimerization can also occur in the gas phase [32]. Thus, a priori, dimers must be considered when considering systems containing NO_2 under operation conditions near room pressure and temperature. On the other hand, the properties of gases and liquids adsorbed in narrow pores highly differ from those in the bulk phase. In this regard, the reactive Monte Carlo (RxMC) method, independently developed by Johnson *et al.* [38] and Smith and Triska [39] for modelling chemical reactions at equilibrium, has been already applied to reactive equilibrium studies [40], including (a) simple bulk phase reactions [41–44], (b) combined chemical and phase equilib-

ria [38, 45], and (c) reactions in confined systems [41, 46–48], among others. In this method, a chemical reaction in a system of interacting molecules is modeled as a Monte Carlo trial move. In one of the initial studies in the literature that used the RxMC method to determine the composition of a given reaction in a confined geometry, Borówko and Zagórski examined the conversion of a LJ dimerisation reaction within a model pore [46]. Independently, Turner *et al.* simulated the equilibrium conversion of the ammonia synthesis reaction and the NO dimerisation reaction within a model carbon pore [41]. In these studies, the conversion of the reactions in the pore deviated significantly from the bulk-phase composition, and a strong effect of the pore width was found. Mullen and Maginn recently modeled the xylene isomer mixture in a carbon nanotube, finding a strong dependence between the dominant xylene isomer and the nanotube diameter [49]. The role of the pore structure was more deeply studied by Hansen *et al.* in zeolites for the propene metathesis reaction system [47, 48]. They also found significant increases in the pore phase conversion compared to the bulk-phase as well as a strong influence of the zeolite topology, temperature and pressure on the pore-phase composition.

Here, we study the effect of confinement on the equilibrium mixture nitrogen dioxide/dinitrogen tetroxide (NO_2/N_2O_4), at different operation conditions of pressure and temperature. We provide insights to understand at a molecular level how the pore structure of the materials modifies the mixture composition by selecting five pure silica zeolites with different topologies: one with cages separated by windows (FAU) and four with intersecting channels and different channel size and directionality (MOR, TON, FER, and MFI). The information given in this paper is organized as follows. Simulation techniques and models for adsorbates and frameworks are detailed in the next section. In Section 3, we discuss the results obtained from the study of the adsorption performance of both species as pure component and binary mixtures, looking at the structural features that differentiate the selected materials. Finally, we provide some concluding remarks in the last section.

4.2 METHODS

We use the reactive Monte Carlo method (RxMC) to simulate the equilibrium properties of the reactive system containing nitrogen dioxide and dinitrogen tetroxide, both in the bulk-phase and confined in the FAU, FER, TON, MFI, and MOR zeolites. The RxMC samples the forward and reverse reaction steps in addition to the conventional MC trial moves. The method requires only the input of the full isolated molecule partition functions [38] for the reactants and products (or Gibbs-free energies of formation of isolated molecules) [39], along with the usual ensemble constants and intermolecular interaction po-

tentials.

The ideal gas partition function for a general case of a non-linear polyatomic molecule is defined as [50]

$$q(V,T) = \left(\frac{2\pi M k_B T}{h^2}\right)^{3/2} V \cdot \frac{\pi^{1/2}}{\sigma} \left(\frac{T^3}{\Theta_{rot,A}\Theta_{rot,B}\Theta_{rot,C}}\right)^{1/2}$$
$$\times \left(\prod_{j=1}^{3n-6} \frac{1}{1-exp\left(-\Theta_{vib,j}/T\right)}\right) \cdot g_{e1} exp(D_0/k_B T) \quad (4.1)$$

$\Theta_{rot,A}$, $\Theta_{rot,B}$, and $\Theta_{rot,C}$, are the characteristic rotational constants of the molecule. M denotes the mass of the molecule, $\Theta_{vib,j}$, is the characteristic vibrational temperature corresponding to the normal mode j, D_0 is the atomization energy at 0 K, σ is the rotational symmetry number or external symmetry number of the molecule [50]. Since only the temperature dependent part of the partition function is needed, dividing eqn (3.1) by volume, we obtain

$$\hat{q}(T) = \frac{q(V,T)}{V} = \left(\frac{2\pi M k_B T}{h^2}\right)^{3/2} \cdot \frac{\pi^{1/2}}{\sigma} \left(\frac{T^3}{\Theta_{rot,A}\Theta_{rot,B}\Theta_{rot,C}}\right)^{1/2}$$
$$\times \left(\prod_{j=1}^{3n-6} \frac{1}{1-exp\left(-\Theta_{vib,j}/T\right)}\right) \cdot g_{e1} exp(D_0/k_B T) \quad (4.2)$$

This expression can be rearranged and defined in terms of $\hat{q}_0(T)$, an ideal gas partition function (excluding the volume term) in which the ground state energy is zero:

$$\hat{q}(T) = \hat{q}_0(T) exp(D_0/k_B T) \quad (4.3)$$

In order to compute the ideal gas partition function, rotational and vibrational constants can be obtained either from ab initio quantum calculations or from the experimental data available in the literature, or alternatively from the JANAF thermochemical tables [47, 50–54]. The ideal gas partition functions of nitrogen dioxide and dinitrogen tetroxide used in this study are obtained based on frequency analysis on optimized molecular geometries in Gaussian09 at the mp2 level of theory with the 6-311+G(2d,2p) basis set [55]. Ideal gas partition functions obtained from ab initio calculations are then compared with the ones obtained based on the experimental vibrational and rotational frequencies of nitrogen oxide and nitrogen tetroxide [56–61]. JANAF thermochemical tables are also used to obtain the ideal gas partition functions [50, 62]. The atomization energy of a molecule D_0 can be determined from the heats of formation at 0 K [47] and is summarized in Table 1. The temperature dependent parts of the ideal gas partition functions ($\hat{q}_0(T)$) obtained from all three methods are in excellent agreement and are summarized in Table 2. More details about the RxMC method can be found elsewhere [39–41, 51].

Table 1. Atomization energies of nitrogen oxide and dinitrogen tetroxide determined based on the heats of formation at 0 K from JANAF tables [63].

	$D_0[kJmol^{-1}]$
NO$_2$	928.47
N$_2$O$_4$	1910.10

Table 2. Computed temperature dependent part of the ideal gas partition functions (zero ground state energy), as defined in eqn (3.2) and (3.3), based on quantum computations using Gaussian09 (mp2/6-311+G(2d,2p)), experimental values from literature and JANAF tables.

	$\hat{q}_0(T)$ NO$_2$ [Å^{-3}]			$\hat{q}_0(T)$ N$_2$O$_4$ [Å^{-3}]		
T (K)	Gaussian	Literature	JANAF	Gaussian	Literature	JANAF
273.1	1.08×10^6	1.06×10^6	1.06×10^6	1.44×10^8	1.33×10^8	1.61×10^8
298.2	1.41×10^6	1.39×10^6	1.39×10^6	2.38×10^8	2.18×10^8	2.61×10^8
318.1	1.73×10^6	1.71×10^6	1.71×10^6	3.49×10^8	3.18×10^8	3.77×10^8
359.6	2.54×10^6	2.52×10^6	2.51×10^6	7.47×10^8	6.70×10^8	7.86×10^8
374.7	2.89×10^6	2.87×10^6	2.87×10^6	9.73×10^8	8.69×10^8	1.01×10^9
404.0	3.69×10^6	3.66×10^6	3.66×10^6	1.60×10^9	1.42×10^9	1.64×10^8

To check the correct reproduction of the single-phase bulk composition of the NO$_2$/N$_2$O$_4$ reaction system, simulations in the isobaric-isothermal ensemble have been carried out in combination with reaction sampling (RxMC). The simulations started with 200 NO$_2$ and 100 N$_2$O$_4$ molecules in the system and different conditions of temperature (from 273 to 400 K) and pressure (from 10^1 to 5×10^2 kPa). The Monte Carlo trials performed during the simulations were translation, rotation, reinsertions, volume changes, and reaction sampling [64]. The results were obtained after running 25.000 equilibration and 250.000 production cycles. The number of Monte Carlo steps per cycle equals the total number of molecules initially in the system. The performance of the NO$_2$/N$_2$O$_4$ equilibrium mixture under confinement in porous materials is evaluated by Monte Carlo simulations in the grand-canonical ensemble (GCMC) with and without combination with reaction sampling (RxMC). The extension of the RxMC to the confined

system is well established, and this essentially only adds a classical external field to the system [38, 40, 41, 48, 54]. The energy levels of molecules are hardly affected by inter-molecular interactions or this external field at all. A full explanation of the RxMC method and its applications can be found in the new edition of Allen and Tildesley [65].

In GCMC simulations the temperature and volume are fixed and the bulk-phase reservoir, represented by a fixed chemical potential, is in chemical equilibrium with the pore phase. The chemical potential directly relates to fugacity and fugacity to pressure by means of the fugacity coefficient through the Peng-Robinson equation of state [64]. For low pressures (ideal gas behavior), the fugacity equals the pressure. The number of cycles used are 50.000 and 500.000 for equilibration and production, respectively. The MC trial moves employed were translation, rotation, reinsertion, swap from the reservoir, and identity change for mixtures. The reaction sam-

pling move was also used in these simulations including the RxMC approach. As in the work of Hansen *et al.* [47], the RxMC method in the constant pressure Gibbs ensemble (GE-NPT) was also employed along with the reactive GCMC approach to ensure that in our system both approaches for modelling chemical equilibrium led to the same results. The GE-NPT simulations started with 350-500 NO_2 molecules in the bulk-phase box and an empty pore phase (zeolite). We used the same number of cycles as in GCMC simulations. The same MC trials are also used, but eliminating identity changes and using transfer trials between simulation boxes (bulk and pore phase, respectively). All simulations are performed using the simulation code RASPA [66, 67].

The guest-host and guest-guest interactions are described by electrostatic and van der Waals interactions. Electrostatic interactions are considered by using Coulombic potentials and the Ewald summation method [64]. van der Waals interactions are described by 12-6 Lennard-Jones potentials. A cutoff distance of 14 Å is used, where the interactions are truncated and shifted with tail corrections applied. The nitrogen oxide monomer (NO_2) and dimer (N_2O_4) are modeled according to previous rigid models developed by Bourasseau et al [29]. Regarding the framework atoms, we use partial charges and Lennard-Jones parameters from the TraPPE-zeo forcefield [68]. Cross interactions are calculated by the

Lorentz-Berthelot mixing rules [69]. Partial charges and Lennard-Jones parameters used in this work are collected in Table 3.

Five pure-silica zeolites with different geometries and topologies are selected, considering them as rigid frameworks. Despite the well-known fact that the effect of zeolite flexibility could play a role in the diffusion of the molecules in the structure, this effect is usually small in adsorption studies [70]. Besides, the diffusion results achieved using flexibility strongly depend on the model used [71]. A representation of the grid surface energy of the selected materials can be seen in Figure 1. MOR, TON, FER, and MFI are zeolites with a structure consisting of interconnected channels with different directionality. The crystallographic positions of the atoms of zeolite MOR are taken from the work of Gramlich [72]. This zeolite is formed by parallel channels in the z-axis with additional adsorption sites in the y-axis. The so-called side pockets are accessible from the main channels only for small molecules [17]. TON zeolite, whose atomic positions are taken from Marler [73], also has a 1D system of channels, but without

Table 3. Lennard-Jones parameters and partial charges of of the adsorbates and the adsorbents.

Atom	ε/k_B(K)	σ(Å)	Charge (e^-)
N(NO_2)	50.36	3.24	0.146
O(NO_2)	62.51	2.93	-0.073
N(N_2O_4)	50.36	3.24	0.588
O(N_2O_4)	62.51	2.93	-0.294
Si(Zeo)	22.00	2.30	1.500
O(Zeo)	53.00	3.30	0.750
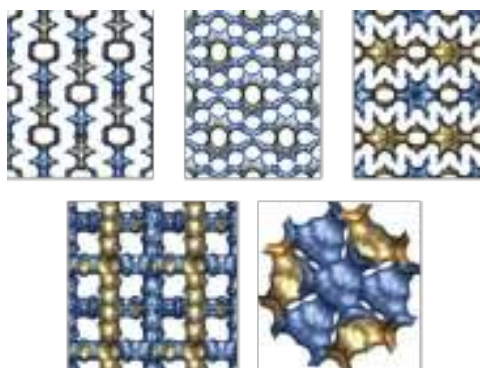
Figure 1. Energy grid surface of zeolites MOR, TON, and FER (top) and MFI and FAU (down). The accessible surface is colored in brown and the inaccessible surface in blue.

pockets associated. The channels in MOR are made of 12-member rings, while TON has 10-member rings, resulting in limiting diameters of about 6.5 Å and 5 Å, respectively. FER shows a 2-dimensional intersected system of channels of 4.7 Å (10-member rings in the z-axis) and 3.4 Å (8-member rings in the y-axis) [74]. The 10-member rings also configure the main channels of MFI zeolite (x-axis), which are intersected by zig-zag secondary channels leading to a 3-dimensional system with limiting diameters of around 4.5-4.7 Å [75]. The last zeolite under study, FAU, has a cubic cell with two types of interconnected cages [76]. The biggest cages, α-cages, are accessible through a 12-member ring window. The smallest, β-cages or sodalites, are connected by 6-member ring windows but are not accessible for most of the molecules due to the narrow windows that connect them with the α-cages (4-member rings). To comply with the experimental

conditions, cavities that are not accessible for the molecules under study need to be blocked [77, 78]. As in a previous work, we use Monte Carlo and Molecular Dynamics simulations to identify these inaccessible cavities [79]. The first, identifies energetic preferential adsorption sites, while the second informs about the diffusion of the molecules. These sites from which the molecules are unable to escape after 0.15 ns were appropriately blocked. In RASPA, the blockage is implemented using a list of geometric descriptions of the inaccessible volumes that are automatically considered as an overlap in MC simulations. Using this methodology, the sodalites in FAU and the y-axis channels in FER were identified and blocked due to narrow access windows that do not allow diffusion of both molecules under study, considering FER zeolite as the 1-dimensional framework for them. A summary of some other interesting properties of the structures, such as surface area, pore size distributions, and pore volume are computed for later analysis (Table A3. 1 and Figure A3. 1 in the Apendix 3).

4.3 RESULTS AND DISCUSSION

4.3.1 Bulk-phase reaction

To validate the molecular models taken from the literature and the partition functions calculated in this work, we carried out RxMC simulations in the isothermal-isobaric (NPT) ensemble for

the bulk phase dimmer destruction reaction ($N_2O_4 \longleftrightarrow NO_2$). The equilibrium constant for the reaction is defined in this work as eqn (3.4).

$$K_{P[atm]} = \frac{P_{NO_2}{}^2}{P_{N_2O_4}} = \frac{\left(P_{Total}X_{NO_2}\right)^2}{P_{Total}X_{N_2O_4}} \qquad (4.4)$$

K_P is the equilibrium constant, P_{Total} is the system total pressure, and $P_{i,j}$ and $X_{i,j}$ are the partial pressures and the mole fractions of each species respectively. Equilibrium constants for the reaction over a temperature range of 273-404 K, are shown in Table 4, comparing the experimental, calculated, and simulated results. The original experimental values were obtained by Wourtzel [35], Bodenstein and Boës [34], and Verhoek and Daniels [31]. The values listed in the table were recalculated by Giauque and Kemp [36]. Calculated constants were obtained by Chao *et al.* from the derivation of thermodynamic functions [32] and our results were obtained in this work at 1 atm of total pressure. The obtained equilibrium constants

Table 4. Comparison of experimental and calculated equilibrium constants for the N_2O_4-NO_2 system. Our data were obtained at 1 atm.

	$K_P[atm]$		
T (K)	**Exp [36]**	**Calc. [32]**	**This Work**
273.10	0.018	0.018	0.019
298.10	0.136	0.146	0.162
318.10	0.628	0.621	0.688
359.60	7.499	7.487	8.239
374.68	16.180	16.111	17.484
403.93	59.430	60.354	63.485

are in agreement with data from other authors for the full range of temperatures. Figure 2 shows the equilibrium mole fraction of N_2O_4 over the studied range of temperatures at pressures from 0.1 to 5 atm. The reference data from the figure were obtained from Chao *et al.* [32] for 0.1 and 1 atm and extrapolated to 0.5 and 5 atm using the reported equilibrium constants. In the figure, the simulated results also describe very well the N_2O_4 equilibrium mole fractions in the full range of temperature and pressure. As expected from experimental evidence, high temperatures favor the destruction of the N_2O_4 dimer molecules. Focusing on the results obtained at ambient pressure, the N_2O_4 mole fraction remains above 0.6 up to room temperature. At higher temperatures, the mole fraction strongly decreases up to less than 0.1 at around 360K,
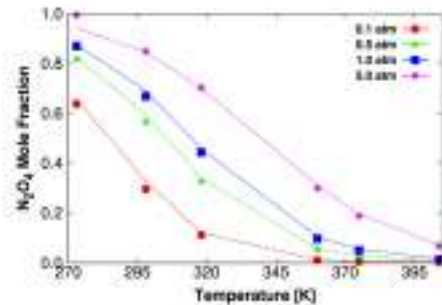
Figure 2. Mole fraction of N_2O_4 for the bulk phase reaction dimerization over a temperature range of 273-404 K and a pressure range of 0.1-5 atm. Solid symbols depict the results obtained in this work from RxMC simulations in the NPT ensemble and the dashed line shows calculated data from Chao *et al.* [32] for direct comparison.

being almost negligible above 370 K. The increase in pressure has the reverse effect, increasing the fraction of the dimer at a fixed temperature. For example, at room temperature the N_2O_4 fraction is increased from *ca.* 0.3 to *ca.* 0.8 from 0.1 to 5 atm, respectively. Information from Figure 2 is summarized in Table A3. 2 in the Apendix 3 . Having validated the equilibrium compositions in the bulk phase using our simulations, we study the equilibrium reaction in the pore phase.

4.3.2   Pure component and equimolar binary mixture adsorption isotherms from GCMC simulations

Pure component adsorption isotherms and the equimolar binary mixture of NO_2 and N_2O_4 at room temperature are shown in Figure 3. The reaction trial move is switched off here. We compute

these isotherms in hypothetical pure and equimolar mixture compositions to analyze the adsorption performance of each molecule as a previous stage for further discussion of the equilibrium mixtures and reaction themselves. The pure component adsorption isotherms in Figure 3a show that NO_2 starts to adsorb in the zeolites at 10 kPa, with loadings at an ambient pressure of around 0.5-1 mol kg^{-1}. The lowest loading at this pressure was found for FAU, the zeolite with the largest pore diameter and cavities (see Table A3. 1 and Figure A3. 2 in the Apendix 3) in which the NO_2 molecules are less strongly bound due to energy effects [80–82]. Saturation loadings are not reached at the highest pressure under study (10^3 kPa), showing the uptakes ordered as a function of the available pore volume of the zeolites: *ca.* 1.5 mol kg^{-1} (FER and TON), *ca.* 2.5 mol kg^{-1} (MOR and MFI), and *ca.* 3.5 mol kg^{-1} (FAU). Dinitrogen tetroxide adsorption in
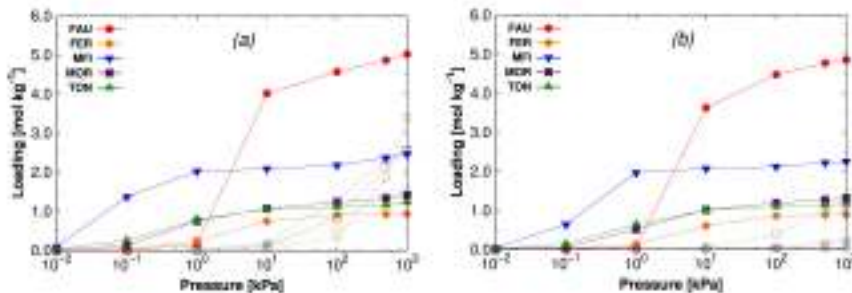
Figure 3. Calculated pure components (a) and binary equimolar mixture (b) adsorption isotherms of NO_2 (empty symbols) and N_2O_4 (full symbols) at room temperature in FAU (red circles), FER (orange diamonds), MFI (blue down triangles), MOR (purple squares), and TON (green triangles). Reaction trial moves are switched off here.

MFI takes place at $10^{-2} - 10^{-1}$ kPa, three orders of magnitude of pressure lower than the monomer, and saturation loading (*ca.* 2 mol kg^{-1}) is reached at 1 kPa. In the rest of zeolites adsorption initiates at 10^{-1}-10^0 kPa and saturation is almost reached at 10-10^2 kPa, with loadings of *ca.* 1-1.5 mol kg^{-1} (FER, TON and MOR) and 5 mol kg^{-1} (FAU). As for NO$_2$, the saturation loadings are ordered as a function of the total pore volume (FAU > MFI > TON > FER), with MOR as an exception. Figure 4 shows the NO$_2$ and N$_2$O$_4$ average occupation profiles (AOP) in zeolite MOR (more detailed views of the distribution of these molecules can be found in Figure A3. 2 and A3. 3 in the Apendix 3). As observed from the figure, while the monomer is absorbed both in the main straight channels and the side pockets, the adsorption of the dimer only takes place in the channels. Part of its pore volume (side pockets) is not acces-
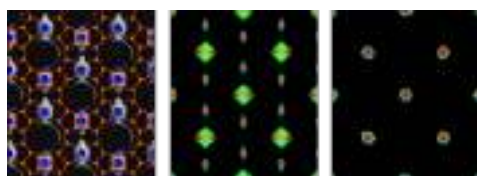
Figure 4. Average occupation profiles of NO$_2$ (center) and N$_2$O$_4$ (right) in zeolite MOR at 5 x 10^2 kPa and room temperature. The figure shows the projection of the center of mass of the molecules over the x-y plane. The color gradation (from black to red) indicates the occupation density. To guide the view, a representation of the structure is added (left) where the oxygen atoms are depicted in red and the silica atoms in yellow. A grid surface is also represented where the accessible part is colored in blue and the non-accessible part in gray.

ible for N$_2$O$_4$, explaining why the saturation loading of the dimer in MOR is lower compared to MFI (with a similar pore volume), being closer to the saturation values of TON, which has a similar topology but without side pockets and a lower pore volume than MOR. Adsorption isotherms from the equimolar binary mixture are shown in Figure 3b. The adsorption of N$_2$O$_4$ is almost unaffected by the presence of NO$_2$. Some reduction in loading can be observed at low-medium pressure caused by the fact that the feeder gas stream now contains 50% of each species, but this effect disappears at saturation, with similar loadings as that in the pure component isotherms. In contrast, the adsorption of NO$_2$ is strongly influenced by the presence of dimers. When N$_2$O$_4$ is present in the system, the adsorption of NO$_2$ drastically decreases to almost negligible values. This behavior occurs in all zeolites except for MOR. In this zeolite, the loading of monomers is reduced about 1 mol kg^{-1}, but with similar N$_2$O$_4$ saturation loading, meaning no NO$_2$ favorable competition for the adsorption sites in the main channels of the structure. As expected from the distribution of molecules as pure components inside this zeolite, the remaining NO$_2$ adsorption in the equimolar mixture takes places only in the side pockets, where there is no competition with N$_2$O$_4$ (see AOP in Figure A3. 2 and A3. 3 in the Apendix 3). The presence of these adsorption sites makes a difference in the adsorption performance compared to other

structures with very similar topology such as TON or FER, in which the adsorption of monomers is completely displaced from the channels with no alternative adsorption sites.

4.3.3   Bulk-equilibrium binary mixtures

The effect of confinement in the equilibrium mixture containing NO_2 and N_2O_4 is also studied. Adsorption isotherms over an extended range of pressures (10^{-1}-10^3 kPa) are obtained at room temperature. Isobars at 10^2 and $5x10^2$ kPa at temperatures spanning from 260 K and 420 K are also calculated.

Adsorption isotherms. Adsorption results from reactive grand-canonical Monte Carlo simulations for the NO_2/N_2O_4 equilibrium mixture at room temperature are shown in Figure 5. Figure 5a shows the NO_2 and N_2O_4 adsorption

isotherms from equilibrium binary mixtures and Figure 5b shows the adsorbed mole fraction of N_2O_4 on the zeolites. The composition of the bulk phase at equilibrium was obtained from NPT reactive MC simulations and used to fix the GCMC bulk-phase composition (also depicted in Figure 5b to guide the discussion). Additionally, results obtained using reactive GCMC are compared to those obtained from reactive constant pressure Gibbs ensemble simulations in Figure A3.4 in the Appendix 3. We compare the results obtained from different methodologies to ensure that the two of them lead to the same results. The agreement using the two approaches allow us to use reactive GCMC simulations for the rest of the study taking advantage of its lower computational cost in comparison with GE-NPT in which both phases need to be simulated at the same time for each simulation [47].
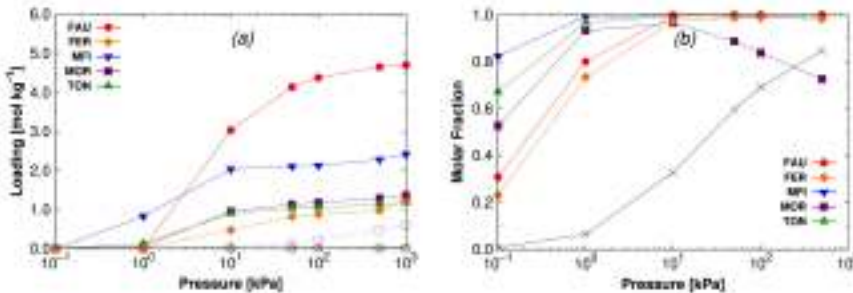
Figure 5. Calculated binary mixture adsorption isotherms (a), and mole fractions (b) of NO_2 (open symbols) and N_2O_4 (closed symbols) at room temperature in FAU (red circles), FER (orange diamonds), MFI (blue down triangles), MOR (purple squares), and TON (green triangles). To clear the figure and guide the eye in (b), only the N_2O_4 mole fractions are plotted (the sum of both mole fractions is equal to 1) and the bulk mole fractions (obtained from NPT reactive simulations) are also added in black. Reaction move is switched on here.

In Figure 5a we see a similar behavior as for that observed from the equimolar binary mixture, with some minor differences. At a pressure below $3x10^1$ kPa, the mole fraction of N_2O_4 in the bulk is lower than that of NO_2 and the adsorption of N_2O_4 is softly reduced compared to the equimolar binary mixture. The starting adsorption of dimers is displaced one order of magnitude in pressure (from 10^{-1} to 1 kPa) in FER, TOR, and MOR while the loading in MFI is reduced 1 mol kg^{-1} at the same pressure. The adsorption in FAU initiates at the same pressure (1 kPa) but the loading at 10 kPa is also reduced by about 1 mol kg^{-1}. At values of pressure above $3x10^1$ kPa, the ratio between themole fractions of NO_2 and N_2O_4 is reversed and the mole fraction of N_2O_4 becomes larger than that of NO_2. Saturation loadings are reached in all the zeolites above 10^2 kPa, as described in the binary equimolar mixture. The adsorption of NO_2 at low pressure is almost negligible despite its larger proportions in the bulk phase, and at high pressure the low NO_2 fraction in the bulk phase reduces the number of molecules adsorbed in the side pockets of MOR, the only structure in which there is competition with N_2O_4 in equimolar conditions.

The mole fractions of dinitrogen tetroxide as a function of pressure depicted in Figure 5b corroborate the fact that confinement goes in favor of dimerization in the full range of pressure. Results at a very low pressure (10^{-1} kPa) should be ignored since the lodgings are almost negligible for the two adsorbates. In MFI, an important loading is reached at 1 kPa (*ca.* 1 mol kg^{-1}) the NO_2 adsorbed fraction being almost negligible. From this pressure, the N_2O_4 adsorbed fraction reaches almost 1.0 as NO_2 adsorption is avoided by N_2O_4 molecules in most zeolites. In relation to the influence of zeolite topology on the equilibrium composition of the reaction mixture, MFI shows the strongest influence. This zeolite has one of the narrowest system of channels under study and interconnections where molecules tend to be preferentially absorbed. TON and MOR are the next two structures with the highest N_2O_4 adsorbed fractions at low pressure, being 1D structures with slightly bigger channels than MFI. FAU is the zeolite where both species commensurate the worst. Its high available pore volume and its topology consisting of big cages weaken the confinement of the gas molecules. Finally, the performance of FER can be attributed to the fact that the secondary system of channels of this zeolite is not accessible to the studied molecules and the available pore volume is the smallest among the studied zeolites. Therefore, this structure has the lowest N_2O_4 adsorption at low and high pressure. Focusing on MOR, the adsorption behavior considering the mole fractions of both components as a function of pressure is particularly interesting. At low pressures, the adsorbed fraction of dimers is larger than the bulk mole fraction, as is the case for the other zeolites. However, once the monomers start

entering the side pockets, the trend is inverted. Figure 5b shows that the adsorbed mole fraction of dimers is lower than that of the bulk fraction at a pressure above 10^2 kPa. This is due to the adsorption of NO_2 molecules in the side pockets of this zeolite, where there is no competition with dimermolecules in spite of its progressive reduction in the bulk phase.

The adsorption selectivity of N_2O_4 over NO_2 is shown in Figure 6. We defined the adsorption selectivity of component i over component j (S_{ij}) as $(x_i/y_j)/(x_j/y_i)$ where $x_{i,j}$ are the mole fractions in the adsorbed phase and $y_{i,j}$ the mole fractions in the bulk phase [83]. The figure shows that the selectivity up to 10 kPa (before saturation of the pore space) follows the same order as that described in Figure 5b (MFI > TON > MFI > FAU
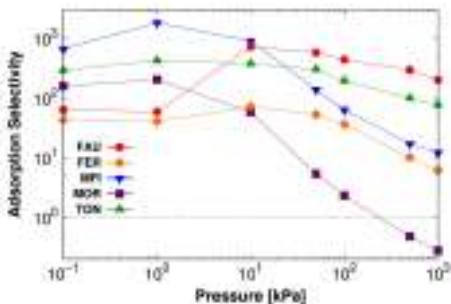
Figure 6. Adsorption selectivity N_2O_4/NO_2 from the binary equilibrium mixture at room temperature in FAU (red circles), FER (orange diamonds), MFI (blue down triangles), MOR (purple squares), and TON (green triangles). Dotted line in the figure denotes an inversion in the selectivity from a N_2O_4 selective behavior to a NO_2 selective behavior. Reaction move is switched on here.

> FER). This means this is strongly related to the order in which N_2O_4 is adsorbed in the zeolites. At 10 kPa FAU shows a high increase in both loading and selectivity showing the best performance at high pressure. Around 10^1-10^2 kPa, N_2O_4 reaches saturation and the loading does not increase despite its bulk fraction increasing for increasing values of pressure, resulting in a reduction of the selectivity but not a significant modification of the adsorbed amount of each component, as can be seen in Figure 5a. This reduction is particularly important in MOR, the selectivity being inverted towards NO_2 above 10^2 kPa because the main channels are already saturated with N_2O_4 and the amount of NO_2 adsorbed in the side pockets still increases while the NO_2 bulk fraction decreases.

Summarizing, the confinement favors the formation of dimers at any pressure at room temperature, increasing its mole fraction regardless of the bulk phase concentration. However, structural features have to be taken into account carefully as they are able to invert this behavior. This happens in zeolite MOR, where there are sites only accessible for NO_2 which makes them very sensitive to the existence of this species in the gas mixture in contraposition with the rest of the zeolites in which NO_2 can be ignored.

Adsorption isobars. The effect of temperature in the confined equilibrium mixture is analyzed in Figure 7 at temperatures ranging from 260-400 K. Figure
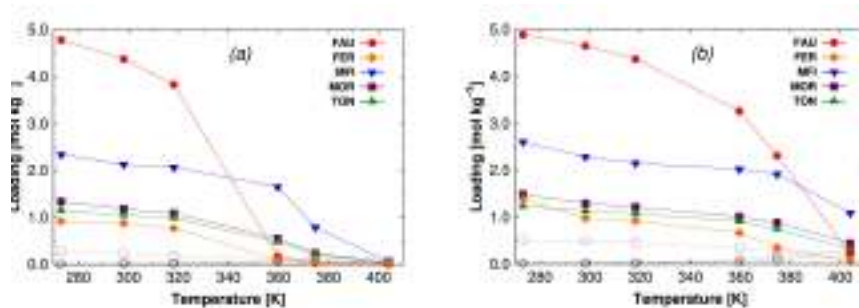
Figure 7. Calculated binary mixture adsorption isobars of NO_2 (empty symbols) and N_2O_4 (full symbols) at 10^2 (a) and $5x10^2$ kPa (b) in FAU (red circles), FER (orange diamonds), MFI (blue down triangles), MOR (purple squares), and TON (green triangles). Reaction move is switched on here.

7a depicts NO_2 and N_2O_4 adsorbed isobars at room pressure. Dinitrogen tetroxide shows saturation loadings in almost all zeolites below 320 K, with a reduction above this temperature due to a combined effect between the increment in the movement of the particles and the decrease of the N_2O_4 bulk fraction. This reduction is more remarkable in FAU as this zeolite has the highest pore volume and diameter, and N_2O_4 does not fit as tightly as in the other zeolites. Around 370 K only MFI keeps a loading of about a half of its total capacity, while at the highest temperature the loading is almost negligible in all zeolites. The adsorption of NO_2 is very low in all zeolites, even in MOR in which also the side pockets are poorly occupied at temperatures below 320 K (less than 0.5 mol kg^{-1}). No increase in the NO_2 adsorbed amount can be seen when the NO_2 bulk fraction increases with temperature, probably due to a very low pressure preventing NO_2 adsorption. Adsorption isobars at

$5x10^2$ kPa are depicted in Figuere 7b. At this pressure, the decrease in the adsorbed amount of N_2O_4 at a temperature above 320 K is lesser than that at room pressure, and slightly higher loadings appear at a high temperature. The pressure increase does not affect the NO_2 adsorption at low temperatures in most zeolites due to the low mole fraction in the bulk composition. MOR is the exception since the adsorption of NO_2 in the side pockets is increased by the pressure increase at low temperatures. In this zeolite, the NO_2 isobar shows a linear behavior as a result of the balanced effect that the temperature exerts on the adsorption performance of this compound. On the one hand, for increasing temperature the bulk fraction of the monomer increases. On the other hand, is the entropic effect and so the adsorption is reduced at higher values of temperature. In the other zeolites, the increment of NO_2 in the bulk fraction with temperature is also responsible of the small rise in its

loading at the highest temperature, in contraposition with the decrease of the dimer adsorption.

The adsorbed dinitrogen tetroxide mole fraction from the equilibrium mixture as a function of temperature is depicted in Figure 8. To see the effect of confinement in the mole fraction and to guide the discussion, the bulk fraction obtained from NPT reactive simulations is also depicted in the figure. At ambient pressure (Figure 8a), the adsorption of N_2O_4 prevails over NO_2 in the full range of temperature, showing a larger fraction of adsorbed dinitrogen tetroxide than that in the bulk. Below 320 K, N_2O_4 fractions near 1 can be observed in all zeolites except MOR, in which they are near 0.8 due to the adsorption of NO_2 in the side pockets. Above this temperature, the reduction in the N_2O_4 loading (Figure 7a) is responsible for the reduction of the N_2O_4 adsorbed fraction. For increasing pressure to $5x10^2$ kPa, the reduction of N_2O_4 adsorption at 320 K is

not so remarkable as that at room pressure because of a stronger N_2O_4 adsorption. The behavior at low pressure is similar for most zeolites, but in this case, MOR shows a reduction in the N_2O_4 adsorbed fraction compared to the bulk. Despite the fact that the adsorption of monomers in MOR takes place at two different pressures in this study, the adsorption is lower at ambient pressure, as this is a low value of pressure for NO_2 to be appropriately adsorbed. At ambient pressure, the adsorbed amount of dimer is larger than expected compared to the bulk phase, with a mole fraction about 20% reduced with respect to other zeolites up to 320 K. In contrast, at the highest value of pressure the adsorbed mole fraction of N_2O_4 is lower than that in the bulk phase up to 320 K, confirming that MOR is very sensitive to the presence of NO_2, whose initial bulk fraction is lower than 0.10-0.25 between 280-320 K. For increasing temperature, the increase of the mono-
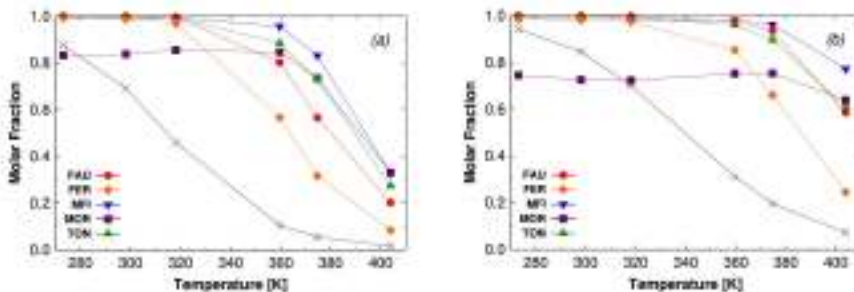
Figure 8. Calculated binary mixture N_2O_4 adsorbed mole fractions at at 10^2 (a) and $5x10^2$ kPa (b) in FAU (red circles), FER (orange diamonds), MFI (blue down triangles), MOR (purple squares), and TON (green triangles). To guide the view, the N_2O_4 bulk mole fraction, obtained from NPT reactive simulations, is also added in black. Reaction move is switched on here.

-mer mole fraction in combination with the reduction of the total loading adsorbed, reduces and finally eliminates this effect, making this structure more selective to N_2O_4.

4.4 CONCLUSIONS

We use molecular simulations to study the effect of the confinement of equilibrium mixtures containing nitrogen dioxide and dinitrogen tetroxide. Models taken from the literature and partition functions calculated in this work were validated by reproducing previously published equilibrium constants and mole fractions of the components in the bulk phase. We verified that the increase of temperature favors the destruction of N_2O_4, while pressure has the opposite effect. The study of the pure component and equimolar mixtures at room temperature shows that the interaction with all zeolites is stronger for N_2O_4 than for NO_2, being absorbed by 2-3 orders of magnitude in pressure before and reaching saturation loadings at room pressure. Saturation is not reached in the range of pressure under study for NO_2 in any of the zeolites, and its adsorption was drastically reduced to almost negligible values when introducing N_2O_4 in the system. However, MOR retains a remarkable NO_2 loading due to the existence of special adsorption sites for this molecule where N_2O_4 did not fit. When analyzing the adsorption isotherms and isobars of the reacting mixture in the zeolites, con-

finement was proved to be responsible for the formation of dimers in the full range of pressure and temperature. Increased density of the adsorbates in the pore phase compared to the bulk, as well the N_2O_4 selective behavior of the zeolites, are responsible for the N_2O_4 formation. The largest deviations from bulk concentrations were found at low temperatures and high pressures, as the effect of confinement weakens at high temperatures and low pressures due to a decrease in the difference in the adsorption strength of both molecules. Among the studied zeolites, MFI exerts the most noticeable influence in the equilibrium composition since it is a zeolite with one of the narrowest system of channels accessible to the molecules, closely followed by TON and MOR. On the other hand, the low available pore volume of FER and the wide size of the cages in FAU, reduce the effect of confinement in these two zeolites. In addition, the selective adsorption sites for NO_2 molecules in MOR strongly modified the general behavior, allowing a high adsorption selectivity towards NO_2 at low temperatures and high pressure. These findings demonstrate that the topological structure of confined systems, such as zeolites, has a crucial influence on the composition of the mixture. The general behavior, N_2O_4 formation in this case, can be modified under certain conditions of pressure and temperature by special structural features such as side-pockets in MOR, as Kim *et al.* have already observed for CO_2/CH_4 separation

[84]. These features must be carefully considered and highlight the need for paying special attention when managing NO_2 adsorption and removal from computational screenings and experimental studies.

4.5   Bibliography

[1]   Mollenhauer, K.; Tschöke, H. *Handbook of Diesel Engines*, 1st ed.; Springer Berlin Heidelberg: New Delhi, 2010; p 636.

[2]   Omidvarborna, H.; Kumar, A.; Kim, D. S. *Fuel Processing Technology* **2015**, *140*, 113–118.

[3]   Sloss, L. In *Nitrogen Oxides Control Technology Fact Book*; Corporation, N. D., Ed.; 1992; p 675.

[4]   Son, B.; Yang, W.; Breysse, P.; Chung, T.; Lee, Y. *Environmental Research* **2004**, *94*, 291–296.

[5]   Das, A. K.; Wilde, J. D.; Heynderickx, G. J.; Marin, G. B. *Aiche Journal* **2001**, *47*, 2831–2844.

[6]   Zhang, X.; Hayward, D. O.; Lee, C.; Mingos, D. M. P. *Applied Catalysis B-Environmental* **2001**, *33*, 137–148.

[7]   Sanchez-Escribano, V.; Montanari, T.; Busca, G. *Applied Catalysis B: Environmental* **2005**, *58*, 19–23.

[8]   Forzatti, P.; Lietti, L. *Heterogeneous Chemistry Reviews* **1996**, *3*, 33–51.

[9]   Shelef, M. *Chemical Reviews* **1995**, *95*, 209–225.

[10]   de Visser, E.; Hendriks, C.; Barrio, M.; Mølnvik, M. J.; de Koeijer, G.; Liljemark, S.; Le Gallo, Y. *International Journal of Greenhouse Gas Control* **2008**, *2*, 478–484.

[11]   Ding, L. F.; Yazaydin, A. O. *Journal of Physical Chemistry C* **2012**, *116*, 22987–22991.

[12]   Yu, J.; Ma, Y.; Balbuena, P. B. *Langmuir* **2012**, *28*, 8064–8071.

[13]   Matito-Martos, I.; Rahbari, A.; Martin-Calvo, A.; Dubbeldam, D.; Vlugt, T. J. H.; Calero, S. *Physical Chemistry Chemical Physics* **2018**, *20*, 4189–4199.

[14]   Deng, H.; Yi, H.; Tang, X.; Yu, Q.; Ning, P.; Yang, L. *Chemical Engineering Journal* **2012**, *188*, 77–85.

[15]   Wang, Y.; Huang, Z.; Liu, Z.; Liu, Q. *Carbon* **2004**, *42*, 445–448.

[16]   Liu, Y.; Bisson, T. M.; Yang, H.; Xu, Z. *Fuel Processing Technology* **2010**, *91*, 1175–1197.

[17]   Garcia-Perez, E.; Parra, J. B.; Ania, C. O.; Garcia-Sanchez, A.; Van Baten, J. M.; Krishna, R.; Dubbeldam, D.; Calero, S. *Adsorption* **2007**, *13*, 469–476.

[18]   Bernal, M. P.; Coronas, J.; Menendez, M.; Santamaria, J. *AIChE Journal* **2004**, *50*, 127–135.

[19]   Anerousis, J. P. *Chemical Engineering* **1976**, *83*, 128.

[20]   Baerlocher, C.; McCusker, L. B.; Olson, D. *Atlas of Zeolite Framework types*, 6th ed.; Elsevier: London, 2007.

[21]   Sun, W.; Lin, L.; Peng, C.; Smit, B. *AIChE Journal* **2014**, *60*, 2314–2323.

[22]   Lin, L.-C.; Berger, A. H.; Martin, R. L.; Kim, J.; Swisher, J. A.; Jariwala, K.; Rycroft, C. H.; Bhown, A. S.; Deem, M.; Haranczyk, M.; Smit, B. *Nature Materials* **2012**, *11*, 633–641.

[23]   Smit, B.; Maesen, T. L. M. *Chemical Reviews* **2008**, *108*, 4125–4184.

[24]   Lachet, V.; Creton, B.; de Bruin, T.; Bourasseau, E.; Desbiens, N.; Wilhelmsen, Ø.; Hammer, M. *Fluid Phase Equilibria* **2012**, *322-323*, 66–78.

[25]   Smith, A. L.; Johnston, H. L. *J. Amer. Chem. Soc* **1952**, *74*, 4696–4698.

[26]   Guedes, H. Ph.D. thesis. PhD thesis, Universidade Nova de Lisboa, Portugal, 1988.

[27]   Glendening, E. D.; Halpern, A. M. *The Journal of chemical physics* **2007**, *127*, 164307.

[28]   Kohler, F. *Journal of Molecular Liquids* **1995**, *67*, 105–123.

[29]   Bourasseau, E.; Lachet, V.; Desbiens, N.; Maillet, J.-B.; Teuler, J.-M.; Ungerer, P. *The journal of physical chemistry. B* **2008**, *112*, 15783–15792.

[30]   Yoshino, K.; Esmond, J. R.; Parkinson, W. H. *Chemical Physics* **1997**, *221*, 169–174.

[31]   Verhoek, F. H.; Daniels, F. *Journal of the American Chemical Society* **1931**, *53*, 1250–1263.

[32]   Chao, J.; Wilhoit, R. C.; Zwolinski, B. J. *Thermochimica Acta* **1974**, *10*, 359–371.

[33]   James, D. W.; Marshall, R. C. *The Journal of Physical Chemistry* **1968**, *72*, 2963–2966.

[34]   Bodenstein, M.; Boës, F. *Z. Phys. Chem. A* **1922**, *100*, 75.

[35]   E. Wourtzel, *C. R. Acad. Sci. Paris* **1919**, *169*, 1397–1400.

[36]   Giauque, W. F.; Kemp, J. D. *The Journal of Chemical Physics* **1938**, *6*, 40–51.

[37]   Harris, L.; Churney, L. K. *The Journal of Chemical Physics* **1967**, *47*, 1703–1709.

[38]   Johnson, J. K.; Panagiotopoulos, A. Z.; Gubbins, K. E. *Molecular Physics* **1994**, *81*, 717–733.

[39]   Smith, W. R.; Triska, B. *The Journal of Chemical Physics* **1994**, *100*, 3019–3027.

[40]   Turner, C.; Brennan, J. K.; Lísal, M.; Smith, W. R.; Karl Johnson, J.; Gubbins, K. E. *Molecular Simulation* **2008**, *34*, 119–146.

[41]   Turner, H. C.; Johnson, K. J.; Gubbins, K. E. *Journal of Chemical Physics* **2001**, *114*, 1851–1859.

[42]   Pusztai, L.; Dominguez, H.; Pizio, O. A. *Revista Mexicana de Fisica* **2003**, *49*, 212–218.

[43]   Carrero-Mantilla, J.; Llano-Restrepo, M. *Fluid Phase Equilibria* **2006**, *242*, 189–203.

[44]   Dominguez, H.; Pizio, O. A. *Physica A: Statistical Mechanics and its Applications* **2002**, *316*, 65–76.

[45]   Lísal, M.; Smith, W. R.; Nezbeda, I. *AIChE J.* **2000**, *46*, 866–875.

[46]   Borówko, M.; Zagórski, R. *Journal of Chemical Physics* **2001**, *114*, 5397–5403.

[47] Hansen, N.; Jakobtorweihen, S.; Keil, F. J. *Journal of Chemical Physics* **2005**, *122*, 164705.

[48] Jakobtorweihen, S.; Hansen, N.; Keil, F. J. *Molecular Physics* **2005**, *103*, 471–489.

[49] Mullen, R. G.; Maginn, E. J. *Journal of Chemical Theory and Computation* **2017**, *13 (9)*, 4054–4062.

[50] McQuarrie, D. A.; Simon, J. D. *Physical Chemistry: a molecular approach*, 1st ed.; University Science Books: Sausalito: California, 1997; p 1360.

[51] Poursaeidesfahani, A.; Hens, R.; Rahbari, A.; Ramdin, M.; Dubbeldam, D.; Vlugt, T. J. H. *Journal of Chemical Theory and Computation* **2017**, *13 (9)*, 4452–4466.

[52] Balaji, S. P.; Gangarapu, S.; Ramdin, M.; Torres-Knoop, A.; Zuilhof, H.; Goetheer, E. L. V.; Dubbeldam, D.; Vlugt, T. J. H. *Journal of Chemical Theory and Computation* **2015**, *11*, 2661–2669.

[53] Stull, D. R.; Prophet, H. *JANAF thermochemical tables, No. NSRDS-NBS-37*; National Standard Reference Data System, 1971.

[54] Rosch, T.; Maginn, E. *Journal of Chemical Theory and Computation* **2011**, *7*, 269–279.

[55] Frisch, M. J. et al. *Gausian 09 Revision C.02*; Gaussian Inc.: Wallingford CT, 2016.

[56] Herzber, G. *Molecular spectra and molecular structure. Volume 3: Electronic spectra and electronic structure of polyatomic molecules*; Van Nostrand: New Jersey, 1966; p 745.

[57] Shimanouchi, T. *Journal of Physical and Chemical Reference Data* **1977**, *6*, 993–1102.

[58] Krainov, L. M. S. E. P.; Kovner, M. A. In *Vibrational spectra of polyatomic molecules*; Wiley„ Ed.; 1974; p 644.

[59] Domenech, J. L.; Andrews, A. M.; Belov, S. P.; Fraser, G. T.; Lafferty, W. J. *The Journal of Chemical Physics* **1994**, *100*, 6993.

[60] Jacox, M. E. *Vibrational and Electronic Energy Levels of Polyatomic Transient Molecules, Journal of Physical and Chemical Reference Data (Book 3)*; American Institute of Physics, 1994; p 461.

[61] Stirling, A.; PaÌApai, I.; Mink, J.; Salahub, D. R. *The Journal of Chemical Physics* **1994**, *100*, 2910.

[62] Chase, M. W. *Journal of Physical and Chemical Reference Data* **1996**, *25*, 551–601.

[63] Chase, M. W.; Curnutt, J.; Prophet, H.; McDonald, R.; Syverud, A. *J. Phys. Chem. Ref. Data* **1975**, *4*, 1–176.

[64] Frenkel, D.; Smit, B. *Understanding Molecular Simulations: From Algorithms to Applications*, second edi ed.; C.

Academic Press: San Diego, CA, 2002.

[65] Allen, M. P.; Tildesley, D. J. *Computer Simulation of Liquids*, second edi ed.; Oxford Clarendon Press: Oxford, 2017; p 640.

[66] Dubbeldam, D.; Calero, S.; Ellis, D. E.; Snurr, R. Q. *Molecular Simulation* **2016**, *42*, 81–101.

[67] Dubbeldam, D.; Torres-Knoop, A.; Walton, K. S. *Molecular Simulation* **2013**, *39*, 1253–1292.

[68] Bai, P.; Tsapatsis, M.; Siepmann, J. I. *The Journal of Physical Chemistry C* **2013**, *117*, 24375–24387.

[69] Allen, M. P.; Tildesley, D. J. *Computer Simulation of Liquids*; Oxford Clarendon Press: Oxford, 1987.

[70] Vlugt, T. J.; Schenk, M. *Journal of Physical Chemistry B* **2002**, *106*, 12757–12763.

[71] Garcia-Sanchez, A.; Dubbeldam, D.; Calero, S. *Journal of Physical Chemistry C* **2010**, *114*, 15068–15074.

[72] Gramlich, V. *Untersuchung und Verfeinerung pseudosymmetrischer Strukturen*. Ph.D. thesis, 1971.

[73] Marler, B. *Zeolites* **1987**, *7*, 393–397.

[74] Morris, R. E.; Weigel, S. J.; Henson, N. J.; Bull, L. M.; Janicke, M. T.; Chmelka, B. F.; Cheetham, A. K. *Journal of the American Chemical Society* **1994**, *116*, 11849–11855.

[75] van Koningsveld, H.; van Bekkum, H.; Jansen, J. C. *Acta Crystallographica Section B-Structural Science* **1987**, *43*, 127–132.

[76] Hriljac, J.; Eddy, M.; Cheetham, A.; Donohue, J.; Ray, G. *Journal of Solid State Chemistry* **1993**, *106*, 66–72.

[77] Calero, S.; Dubbeldam, D.; Krishna, R.; Smit, B.; Vlugt, T. J. H.; Denayer, J. F. M.; Martens, J. A.; Maesen, T. L. M. *Journal of the American Chemical Society* **2004**, *126*, 11377–11386.

[78] Krishna, R.; van Baten, J. M. *Langmuir* **2010**, *26*, 2975–2978.

[79] Matito-Martos, I.; Álvarez-Ossorio, J.; Gutiérrez-Sevillano, J. J.; Doblaré, M.; Martin-Calvo, a.; Calero, S. *Phys. Chem. Chem. Phys.* **2015**, *17*, 18121–18130.

[80] Krishna, R.; van Baten, J. M. *Physical chemistry chemical physics : PCCP* **2011**, *13*, 10593–10616.

[81] Krishna, R.; Smit, B.; Calero, S. *Chemical Society Reviews* **2002**, *31*, 185–194.

[82] Torres-Knoop, A.; Dubbeldam, D. *ChemPhysChem* **2015**, *16*, 2046–2067.

[83] Talbot, J. *AIChE Journal* **1997**, *43*, 2471–2478.

[84] Kim, J.; Abouelnasr, M.; Lin, L.-C.; Smit, B. *Journal of the American Chemical Society* **2013**, *135*, 7545–7552.

Discovery of an Optimal Porous Crystalline Material for the Capture of Chemical Warfare Agents

Ismael Matito-Martos, **Peyman Z. Moghadam, Aurelia Li, Valentina Colombo,**
Jorge A. R. Navarro, Sofía Calero, and David Fairen-Jimenez

Chemical warfare agents (CWAs) are regarded as a critical challenge in our society. Here, we use a high-throughput computational screening strategy backed up by experimental validation to identify and synthesize a promising porous material for CWA removal under humid conditions. Starting with a database of 2932 existing metal-organic framework (MOF) structures, we selected those possessing cavities big enough to adsorb well-known CWAs such as sarin, soman, and mustard gas as well as their nontoxic simulants. We used Widom method to reduce significantly the simulation time of water adsorption, allowing us to shortlist 156 hydrophobic MOFs where water will not compete with the CWAs to get adsorbed. We then moved to grand canonical Monte Carlo (GCMC) simulations to assess the removal capacity of CWAs. We selected the best candidates in terms of performance but also in terms of chemical stability and moved to synthesis and experimental breakthrough adsorption to probe the predicted, excellent performance. This computational-experimental work represents a fast and efficient approach to screen porous materials in applications that involve the presence of moisture.
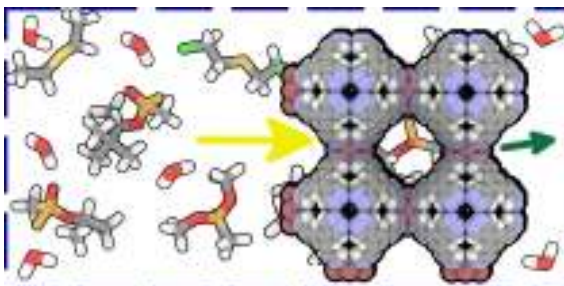
5.1 INTRODUCTION

Chemical warfare agents (CWAs) are highly toxic compounds designed to cause harm, death, temporary incapacitation or sensory irritation through their chemical actions. CWAs were used during World War I [1], and since then the threat has continuously evolved with the development of increasingly more toxic chemicals. Even though their use is strictly prohibited according to the Chemical Weapons Convention of 1993, protection against deliberate attacks using CWAs is still regarded as a critical challenge [2]. In particular, CWAs such as sarin and soman, two well-known nerve agents, and mustard gas, a vesicant compound, have received great attention due to its relatively easy accessibility [3]. Nowadays, efforts for the elimination of chemical weapons are continuously increasing, something that has been recognized with, for example, the prestigious Nobel Peace Prize to the Organization for the Prohibition of Chemical Weapons (OPCW) in 2013. Nevertheless, population exposure to nerve gas attacks has continued occurring; for example, chemical attacks in Syria reported in August 2013 [4].

In order to reduce the risk of exposure, the development of suitable capture methods for a wide range of chemical threats is highly necessary. Historically, activated carbons (ACs) have been used for CWAs and small toxic industrial chemicals (TICs) capture. One of the most important

drawbacks of ACs, however, is their low adsorption capacity [2, 5–7]. In addition, to afford a broad spectrum of applicability, ACs are generally impregnated with a variety of acidic and basic compounds that inherently react between them over time, reducing their efficacy [2]. An alternative that has arisen in the last years is the use of metal-organic frameworks (MOFs) for the capture of CWAs, a possibility that has been extensively explored both experimentally and using molecular simulation [8–14]. MOFs are porous crystalline materials built from metal or metal-based clusters linked by organic ligands to form a three-dimensional structure [15–18]. MOFs exhibit a considerable degree of tunability, not only due to the wide diversity of possible inorganic and organic components that can be included but also via postsynthetic modification of their structures [19]. Indeed, in a recent collaboration with the Cambridge Crystallographic Database Centre, we have identified 84.000 MOFs already synthesized, a number that will continue growing every year [20]. The high tunability of MOFs allows an oriented control and design of structural features such as pore size and geometry, surface area and surface chemistry, which results in unbeaten adsorptive and catalytic properties [21, 22], including the capture and/or decomposition of harmful volatile chemicals [8–13].

In spite of their potential, the main limitation for finding optimal MOFs for CWA and TIC capture relies in obvious health

and safety complications, and therefore experimental studies are rather scarce [2]. Often, testing CWAs is very expensive and not universally available, and therefore most of the studies are based on a surrogate chemical, commonly called simulant or analogue, that possesses most of the key features of the real agent [5]. In this regard, Bobbitt *et al.* recently reviewed the experimental and computational studies about the use of MOFs for detoxification applications of CWAs and TICs [14]. Zou *et al.* reported the synthesis of a MOF with an extremely high capacity for the capture of the nerve agent simulant methylphosphonic acid (MPA) [23]. More recently, Montoro *et al.* compared the suitability of a hydrophobic Zn pyrazolate-based MOF against the hydrophilic HKUST-1 to capture sarin and mustard simulants (diisopropylfluorophosphate and diethylsulfide, respectively). This work showed that, although the coordinatively unsaturated metal sites present in HKUST-1 result in an outstanding performance in dry conditions, their efficiency dropped in the presence of ambient moisture [3]. Following a similar approach, Padial *et al.* reported the suitability of a series of Ni pyrazolate-based MOFs for the capture of DES under the presence of moisture [24]. Plonka *et al.* reported Zr-MOFs as being effective adsorbents of CWAs from the air [7], whereas Mondloch *et al.* [25] and Moon *et al.* [26] used Zr-based NU-1000 for the catalytic destruction of soman. Importantly, in all these studies, competitive adsorp-

tion of water from atmosphere emerges as an unavoidable challenge that can significantly affect CWAs capture performance of MOFs and other porous materials. A potential solution to this challenge is the use of hydrophobic materials that selectively adsorb CWAs and TICs in competition with water [27]. By using hydrophobic MOFs, the pores can potentially remain empty, avoiding water adsorption, while maintaining their adsorption capability for CWAs.

Given the large number of existing MOFs [20], the use of molecular simulations has demonstrated to be an outstanding tool for high-throughput screening (HTS) of them [28, 29]. In particular for CWAs and TICs, computational work also avoids the experimental complications associated with toxic compounds. Recently, Ghosh *et al.* used grand canonical Monte Carlo (GCMC) simulations to predict water adsorption in a series of MOFs, using the pressure at which water condenses in the pores as an indicator of their hydrophobicity [11]. However, screening a large number of materials using this criterion is computationally too expensive and very time-consuming due to long water equilibration times in GCMC simulations, typically in the order of 1 month per pressure point in an adsorption isotherm [12]. We recently proposed an alternative method to use the more easily calculated water Henry's constants (K_H) as and efficient tool for calculating the hydrophobicity for porous materials and for HTS

of a large number of structures [12]. K_H describes the zero loading region of the isotherm (i.e., the Henry region), giving information about adsorbate-adsorbent interactions. K_H is usually obtained from the slope of the adsorption isotherm at low loadings but can be also quickly computed using the Widom insertion method [30]. This method provides reliable K_H values and, critically, is orders of magnitude faster (e.g., minutes vs months) than those calculated from GCMC adsorption isotherms.

In this work, we have explored the use of HTS to study the capture of three CWAs: sarin, soman, and mustard gas—also known as sulfur mustard or HD—in the presence of moisture. We have also extended the study to their simulants, commonly used in experiments: diisopropylfluorophosphate (DIFP), dimethyl methylphosphonate (DMMP) and diethylsulfide (DES). Figure 1 shows the atomic representation of the three CWAs and three simulants. Figure 2 shows a representation of the screening process followed in this work. We used Widom insertion to screen 1647 MOF structures to identify the most suitable materials for CWA capture. We also included water adsorption in order to discard those materials in which the presence of water would fill their porosity and reduce the CWAs capture under humid conditions. We further explored the storage capacity of 156 top-performing MOFs using GCMC simulations to highlight the best candidates for this
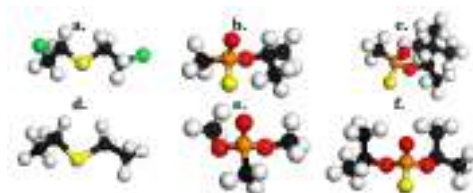
Figure 1. Atomic representation of the CWA molecules: a. mustard gas, b. sarin, and c. soman; and their respective simulants d. diethylsulfide (DES), e. dimethyl methylphosphonate (DMMP), and f. diisopropylfluorophosphate (DIFP). Carbon, oxygen, chlorine, fluorine, phosphorus, and hydrogen atoms are depicted in black, red, green, yellow, orange, and white, respectively.
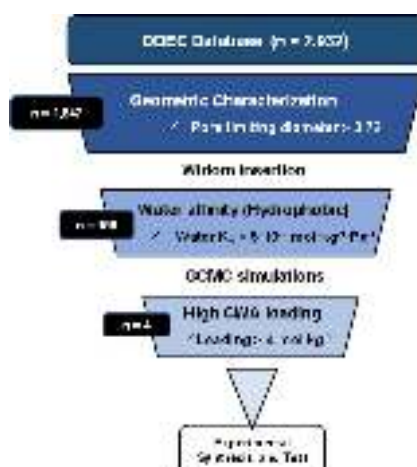
Figure 2. Schematic representation of the screening strategy followed in this work.

application and compared our results with experimental findings.

5.2 METHODS

Computational methods. The geometrical properties for all the MOFs were taken from the 2932 experimentally synthesized MOF structures reported by Chung *et*

al.[31]. The geometric characterization of each MOF structure was carried out for the largest cavity diameter (LCD), accessible pore volume (PV), and gravimetric surface area (GSA) using Zeo^{++} [32]. The reported GSAs were obtained using a probe atom of 3.72 Å diameter (corresponding to that of N_2) [33], and only included 1647 out of 2932 MOFs, those with pore regions accessible through windows large enough to admit N_2. This excludes MOFs where the chemicals under study do not access their pores.

All Monte Carlo simulations were performed using the code RASPA [34]. We first carried out Monte Carlo simulations in the canonical ensemble (CMC) using Widom test particle method [30] to evaluate helium void fraction as well as adsorbate-adsorbent interactions through Henry's constants (K_H) and isosteric heats of adsorption (Q_{st}). These simulations were carried out in the limit of zero loading with only one CWA molecule in the system. We used 40.000 production cycles for Widom insertion. Throughout this work, Q_{st} refers to the negative value of the enthalpy of adsorption, and therefore positive values are shown. GCMC simulations were performed to estimate adsorption loadings at room temperature. During each GCMC cycle, translation, rotation, insertions, deletions, and regrow moves are attempted, using 200.000 equilibration cycles and 200.000 production cycles. The number of Monte Carlo steps per cycle equals the total number of molecules in the system with a minimum of 20 steps. van der Waals interactions were described by 12-6 Lennard-Jones potential using a cutoff distance of 14 Å, where the interactions were truncated and analytical tail corrections were implemented. The force field parameters for water were taken from the TIP4P model [35]; TraPPE force field was used for DMMP, sarin, soman [36], and DES [37]. The parameters for mustard gas were taken from Müller *et al.* [38] and those for DIFP from Vishnyakov *et al.* [39]. Force field parameters for CWA and simulants are summarized in Tables A4. 1-5. The Lennard-Jones parameters for the framework atoms were adopted from the Dreiding force field (DFF) [40] with the exception of metallic atoms, that were taken from the Universal Force Field (UFF) [41]. All MOFs were treated as rigid in the simulations. Adsorbate-adsorbate and adsorbate-adsorbent van der Waals interactions were taken into account by Lorentz-Berthelot mixing rules [42]. Framework atomic charges were calculated by Nazarian *et al.* using plane-wave DFT calculations and DDEC charge partitioning method [43]. Electrostatic interactions were considered by using Coulombic potentials and Ewald summations.

Five-Dimensional Visualization Platform. All of the data obtained can be visualized online on our 5D interactive platform `http://aam.ceb.cam.ac.uk/mof-explorer/CWACapture`. Users can explore the data by plotting any one of

the 33 variables on the x, y, z, color, and size axes. Each data point corresponds to a structure, and the name is indicated when hovering the cursor over the point. Furthermore, both the data table and the graph can be filtered, allowing the users to focus on a subset of structures. A specific MOF can also be tracked through different plots by clicking on the corresponding data point.

UTEWOG Synthesis. $[Ni_3(BTP)_2]$ (UTEWOG) was synthesized according to Colombo *et al.* [44]. Thermogravimetric, diffuse reflectance and XRPD analyses were used to determine the identity and phase purity of the material. TGA was carried out under air, on a Shimadzu-TGA-50H/DSC equipment, at a heating rate of 293 K min^{-1}. XRPD data were collected on a Bruker D2-PHASER diffractometer using CuKα radiation (λ = 1.5418 Å). The compounds were manually grounded in an agate mortar, then deposited in the hollow of a zero background silicon sample holder and measured.

DES Adsorption Measurements. For the evaluation of the dynamic adsorption of DES vapor at RH 80% by $[Ni_3(BTP)_2]$ (Scheme A4. 1 in the Apendix 4). The $[Ni_3(BTP)_2]*7.5H_2O$ material (166 mg) in microcrystalline form was packed in a stainless steel column, 5 cm length and 5 mm inner diameter. Afterward, the material was activated at 523 K for 12 h under a 20 mL min^{-1} He flow. Afterward a constant flow of N_2 (4 mL min^{-1})

was bubbled in a flask containing DES at 303 K and then mixed with a N_2 flow (16 mL min^{-1}) bubbled in a flask containing distilled water at 303 K. Once, the composition of the gas mixture was stable it was flowed through the chromatographic column at room temperature. The DES content of the eluted gas flow was determined employing a flame ionization detector (FID) of a Varian 450-GC gas chromatograph.

The reversibility of the DES adsorption process was evaluated through TGA, XRPD, reflectance diffuse and temperature-programmed desorption using a heating ramp of 10 K min^{-1} and an Omnistar mass spectrometer.

5.3   RESULTS AND DISCUSSION

The CSD MOF subset contains *ca.* 84.000 structures as of April 2018, CSD version 5.39 [20]. However, since high quality partial charges are critical to getting meaningful adsorption isotherms for polar compounds, we focused on the materials provided by the DDEC database containing 2932 porous structures where the framework charges were accurately calculated [43]. Figure A4. 1 in the Apendix 4 shows a summary of the geometric characterization of each MOF structure: largest cavity diameter (LCD), pore volume (PV), and helium void fraction (HVF). Out of these 2932 structures, some of them exhibit too narrow pores to be useful in our study, and therefore we excluded 1275
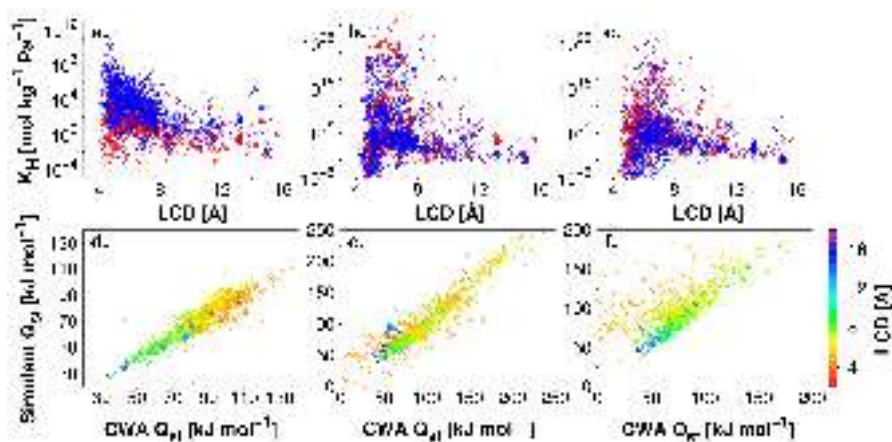
Figure 3. Henry's constants (K_H) as a function of the largest cavity diameter (LCD) of 1647 MOFs for a. mustard gas and DES, b. sarin and DMMP, and c. soman and DIFP. Blue and red data points represent the CWA and the simulant, respectively. d., e., f. Comparison of the heat of adsorption (Q_{st}) for each CWA and simulant. Color code represents the LCD of MOF structures. All simulations were performed at 298 K.

structures with pore limiting diameters (PLDs) lower than 3.72 Å [33]. Figure A4. 1 in the Apendix 4 shows the gravimetric surface area (GSA) histograms for the 1647 remaining MOFs.

To estimate efficiently the strength of the MOF-CWA interactions at low coverage, we used Widom insertion to obtain, for all 1647 MOFs, the K_H and isosteric heat of adsorption (Q_{st}) for the CWAs, their simulants and water-at room temperature. By using Widom insertion we were able to reduce significantly the computational time required, compared to standard GCMC simulations. Figure 3 delimits the relationship between K_H, Q_{st}, and the LCD of the studied MOFs for the three CWA and simulant molecules. For mustard and its simulant (Figure 3a), K_H span from *ca.* 10^{-4} to *ca.* 10^{12} mol kg^{-1} Pa^{-1} .

Both molecules show a similar trend, although the interaction is slightly stronger for the mustard gas compared to DES; this can be attributed to the fact that mustard gas is a bulkier molecule. In general, MOFs with LCDs around 5 Å show the highest K_H values, while the interactions decrease for materials with LCD values larger than 8 Å (e.g., $K_H < 10^4$ mol kg^{-1} Pa^{-1}). Figure 3d shows a comparison between the Q_{st} for mustard gas and DES, confirming the good correlation between their adsorption behaviors and the relationship with the LCD. Q_{st} ranges from 30 to 130 kJ mol^{-1}, with values lower than 80 kJ mol^{-1} for MOFs with LCDs larger than 8 Å, and the highest Q_{st} values are found in MOFs with cavities of around 5 Å. Figure 3b-e and c-f show the results for sarin and DMMP, and soman and DIFP, re-

spectively. We found larger K_H values for these molecules compared to mustard gas-going to extreme values as high as 10^{30} mol kg^{-1} Pa^{-1}. In terms of Q_{st}, the highest values are obtained for LCD around 5-6 Å, where Q_{st} ranges between 50 and 200 kJ mol^{-1} for soman and DIFP, and *ca.* 250 kJ mol^{-1} for sarin and DMP. Differences in shape and size of these two pairs of molecules are more evident, resulting in a slightly poorer correlation between the CWAs and their simulants compared to mustard gas-DES pair. This poor correlation is more evident for soman and DIFP specifically in MOFs with LCD values around 5-7 Å; see yellow and orange points in Figure 3f. We attribute this to DIFP's more linear and symmetrical geometry which enables fitting more tightly in structures with more confined LCDs, whereas the bulkier molecule soman faces larger energy penalties for accessing a similar range of pores. Figure A4.2 in the Apendix 4 shows the Q_{st} for the CWAs on each MOF as a function of GSA and LCD. The highest Q_{st} values are found in structures with quite low surface areas (< 1000 m^2 g^{-1}), whereas the strength of the interaction remains high in structures with surface areas up to 2000 m^2 g^{-1}. Mustard gas, soman, and sarin reach Q_{st} values up to 100, 160, and 200 kJ mol^{-1} in these MOFs.

In order to visualize and analyze the large amount of data obtained and to better uncover the structure–property relationships, we developed an online 5D interactive data-mining platform available at `http://aam.ceb.cam.ac.uk/mof-explorer/CWACapture`. This tool allows users to plot any of the figures presented in this manuscript by choosing among the 33 available variables, for example, MOFs geometric properties, CWA selectivity, water affinity, heat of adsorption, Henry's constants, etc., to be represented on any of the five axes, x, y, z, color, and size. Any of the figures presented here can be reproduced with this tool. In addition, each structure is identified with their CSD refcode, allowing users to track the same structure throughout different plots.

This preliminary HTS is useful to map the interactions between MOFs and CWAs/simulants and to understand the goodness of the simulants to substitute CWAs in experiments and simulations. However, as stated above, the suitability of MOFs to achieve an efficient removal of CWAs needs to be evaluated under humid conditions in the presence of water. To address this problem, we studied the water affinity of the 1647 MOFs through the estimation of Q_{st} and K_H, using Widom insertion method [30], avoiding highly time-consuming GCMC simulations. Figure A4.3 in the Apendix 4 shows the K_H and Q_{st} for water as a function of LCD. We included two benchmarks for comparison: the well-known hydrophobic MOF ZIF-8 [12], and the hydrophilic MOF HKUST-1 [45]. Figure 4 highlights the MOFs exhibiting K_H below the upper limit given by HKUST-1, assuming that MOFs with
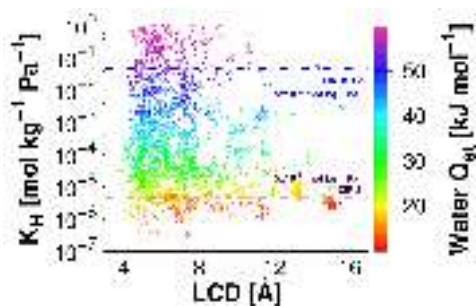
Figure 4. Henry's constants (K_H) for water as a function of the largest cavity diameter (LCD) in MOF structures with K_H lower than 1 mol kg^{-1} Pa^{-1} at 298 K. Purple and blue dashed lines depict water K_H in ZIF-8 and HKUST-1, respectively, as benchmarks for hydrophobicity and hydrophilicity in MOFs. Color code represents isosteric heat of adsorption (Q_{st}) for water.

higher K_H will be saturated with water at 80% relative humidity. From all the 1647 MOFs screened, we identified 156 hydrophobic structures (*ca.* 9.5% of all studied MOFs) with K_H and Q_{st} values lower than that of ZIF-8 (i.e., $5x10^{-6}$ mol kg^{-1} Pa^{-1} and 30 kJ mol^{-1}, respectively) [12, 46]. 937 MOFs (57.0%) were more hydrophilic than HKUST-1 (i.e., $K_H > 5x10^{-2}$ mol kg^{-1} Pa^{-1} and $Q_{st} > 40$ kJ mol^{-1}), whereas 554 MOFs (33.6%) exhibit an intermediate hydrophobic character between ZIF-8 and HKUST-1.

The selectivity of a CWA over water at low loadings can be estimated by the ratio of the K_H values of the two components– this is particularly true for hydrophobic MOFs (i.e., the MOFs we want, in principle, to focus on) since water will not be competing with the CWA molecule to get adsorbed. Figure 5 shows the selectivity for mustard gas, sarin and soman over water as a function of the gravimetric surface area, water Q_{st}, and LCD for the 1647 MOF structures studied here (for simulants see Figure A4. 4 in the Apendix 4). MOF selectivities go up to 10^6 independently of the surface area. Depending on
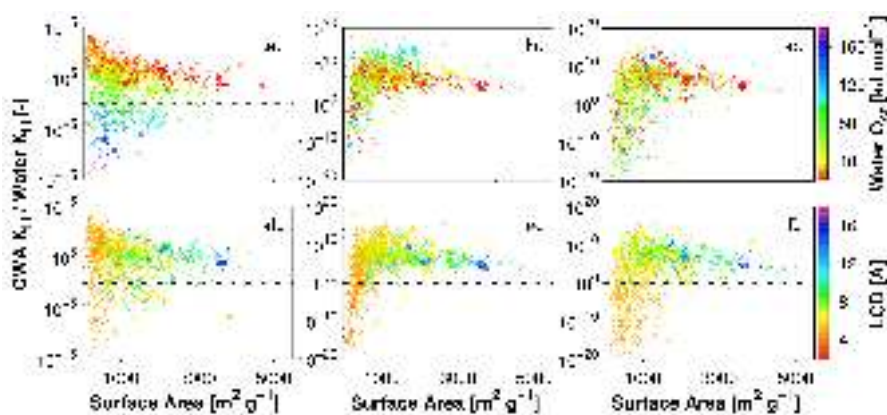
Figure 5. Selectivity of a., d. mustard gas, b., e. sarin, and c., f. soman over water based on the K_H ratio as a function of the surface area in 1647 MOF structures. The color code shows the isosteric heat of adsorption (Q_{st}) for water (a-c) and largest cavity diameter (d-f) for each MOF structure.

the CWA, the selectivity is governed by water affinity (mustard gas and DES, Figure 5a and d, and Figure A4. 4a and d, respectively), LCD (soman and DIFP, Figure 5b and e, and Figure A4. 4b and e, respectively) or both (sarin and DMMP, 5c and f and Figure A4. 4c and f, respectively). In the case of mustard-the more hydrophobic agent-structures with water Q_{st} values of less than 40 kJ mol^{-1} exhibit the highest selectivity values. For sarin and soman which contain strongly polar P = O bonds, the highest selectivities are obtained for materials with a higher affinity for water with Q_{st} values of $ca.$ 100 kJ mol^{-1} . In general, most of the non-CWA selective structures exhibit very low surface area (< 1000 m^2 g^{-1}), which may suggest that either the pores are too small for CWA molecules, or that the pores and interaction are optimal for water adsorption. Figure A4. 5 in the Apendix 4 shows the impact of CWA affinity on selectivity. In the case of soman, sarin, DIFP and DMMP their affinity is strongly correlated with the selectivity, whereas in the case of mustard and DES, their affinity does not seem to show any correlation. This confirms the importance of water affinity for these latter molecules. Importantly, the MOFs with the best performance in terms of high selectivity and high surface area are in good agreement with the 156 hydrophobic MOFs previously identified according to water K_H and Q_{st} criteria.

Although the high surface areas of top-performing MOFs in terms of selec-

tivity indicates that we are far away from Henry's regime during CWA adsorption, using this approach (i.e., evaluating selectivity using the ratio of K_H) is valid for hydrophobic materials since water will not be adsorbed. To confirm that, we ran computationally demanding GCMC simulation of water adsorption at 80% relative humidity (i.e., at 3280 Pa based on the vapor pressure predicted for the TIP4P water model) on the selected 156 hydrophobic MOFs identified from the water Widom screening (Figure A4. 6 in the Apendix 4). GCMC simulation confirms the extremely low water adsorption in the selected hydrophobic MOFs, with less than 0.1 mol kg^{-1} in almost all structures; it also confirms the goodness of the Widom approach and its applicability on fast preselection screening while ensuring minimized competitive water adsorption even at high humidity (RH = 80%). We continued with the GCMC simulation of mustard gas (at 13.8 Pa) [47–49] and nerve agents (at 0.6 Pa) [50, 51], according to the reported median lethal concentration-time product (LCt$_{50}$) at respiratory level for these molecules. Figure 6 shows the loading capacity of mustard gas, sarin, and soman as a function of the CWA/water Widom selectivity and surface area; Figure A4. 7 shows the loading capacity of mustard gas, sarin, and soman as a function of the LCD and Q_{st} . The 156 selected hydrophobic MOFs show very high selectivities, particularly for structures with surface areas below 1000 m^2 g^{-1} and high Q_{st} . As expected, adsorption
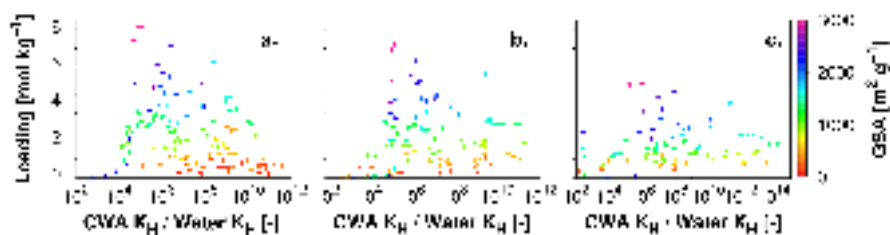
Figure 6. GCMC calculated loadings for a. mustard, b. sarin, and c. soman adsorption at 13.8 Pa (mustard) and 0.6 Pa (sarin and soman), as a function of selectivity over water based on Henry's constants (K_H/K_H). Each point represents one of the 156 hydrophobic MOFs studied at 298 K. The color code shows the surface area of each MOF.

loadings are strongly related to surface area, where the highest loadings, up to 8 mol kg^{-1}, are found in MOFs with surface areas larger than 2000 m^2 g^{-1} as illustrated by the dark blue and purple data points. Loading capacities are also highly dependent on LCD, which in turns directly influence CWA affinity (Figure A4. 7 in the Apendix 4). Larger LCDs (generally > 12 Å) and surface areas allow maximizing loading capacities, while smaller pores limit their performance in spite of the increase in CWA Q_{st} values and K_H selectivities.

To identify promising MOFs capable of capturing a wide range of CWAs, we compared the loading capacities for mustard gas and the nerve agents, represented in Figure 7a. Interestingly, we found an excellent correlation for the loadings of the different CWAs. This minimizes the experimental synthesis and characterization of MOFs, since identifying an optimal structure that is good for capturing one CWA means that it will be also optimal for the other two. At this point, we shortlisted the top eight structures with CWA

capacities higher than 4 mol kg^{-1} . We then took a number of considerations into account to propose candidates for experimental testing. In general, a combination of high surface area, high pore volume and ease of synthesis are important requirements for practical applications. Besides, water stability and surface hydrophobicity are crucial for capture and removal processes that involve moisture. From the eight shortlisted MOFs, we found four structures (CSD codes: BIBXUH [24], SOHGUS [52], Co26NDP, and UTEWOG [44]) with metal-pyrazolate coordinative bonds, that are known to impart high thermal and, in some cases, chemical stability in MOFs [53]. However, from a close look on their crystal structures, we found out that SOHGUS is a DMF-solvated form of CO-JHIT, Long's CoBDP (where BDP^{2-} = 1,4-benzenedipyrazolate) flexible MOF [52] – a well-known pyrazolate-flexible MOF that has been tested for methane storage [54]. However, we decided to reject this MOF since it is unstable, and decomposes in air after few minutes. Additionally, we discarded three structures (CSD codes:
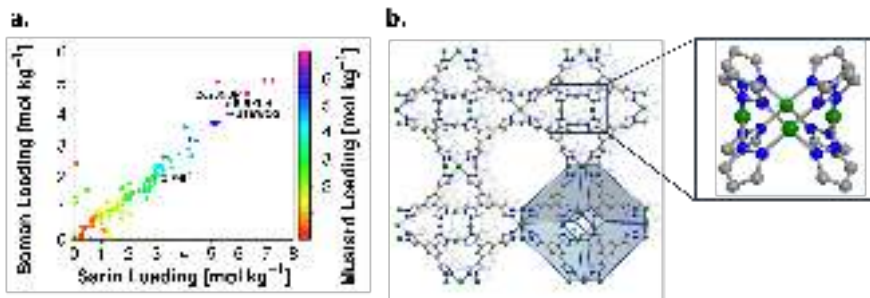
Figure 7. a. Comparison of the calculated mustard, sarin, and soman adsorption loading at 13.8 Pa (mustard) and 0.6 Pa (sarin and soman) in 156 hydrophobic MOFs at 298 K. b. Crystal structure of [Ni$_3$(BTP)$_2$] (CSD code: UTEWOG). The inset shows the tetranuclear cluster of Ni(II) atoms and exobidentate pyrazolate linkers. Carbon, gray; nitrogen, blue; nickel, green. Hydrogen atoms have been omitted for simplification.

HIGRIA, BICDAU, and IVETOT) that although present optimal performance, they are reported to collapse upon activation [31]. IRMOF-6 (CSD code: EDUTIG) was also discarded because of its low water stability [17]. All in all, we ended with three top MOF candidates (CSD codes: BIBXUH, Co26NDP, and UTEWOG); Figure 7b and Figures A4. 8-9 show the representation of UTEWOG, BIBXUH, and Co26NDP, respectively; Tables A4. 6-7 summarize their structural properties and CWA adsorption capacities (Co26NDP corresponds to core-mof-ddec-365 from the work from Nazarian *et al.*; no CSD code was provided in the paper, and is not found in the CSD, which strongly suggests it is a hypothetical structure). It is important to mention that accessibility of the pore space, thermal and chemical stability, as well as hydrophobicity, have been experimentally tested for most of the selected MOFs with very good results [24, 44], supporting our

choice among the huge number of MOFs available in the database.

In order to confirm the applicability of our computational screening approach, and from the practical point of view, we selected [Ni$_3$(BTP)$_2$] (CSD code: UTEWOG) for synthesis since it is regarded as one of the most thermally and chemically stable MOF materials [44]. In addition to its robustness, UTEWOG contains large pores (LCD = 14.6 Å and void fraction = 0.8), which means all CWAs can access its porous network. Predicted CWA uptakes in UTEWOG are sarin, 5.6 mol kg^{-1}; soman, 4.0 mol kg^{-1}; and Mustard: 6.3 mol kg^{-1}. The presence of low spin Ni(II) square planar metal centers in this system is a favorable feature in order to avoid water coordination to the activated material [55]; our simulations also predicted insignificant water uptake of *ca.* 0.019 mol kg^{-1} at 80% RH with a heat of adsorption of -14.2 kJ mol^{-1}. Compared with Q_{st} val-

ues for mustard -80.4 kJ mol^{-1}, sarin -82.3 kJ mol^{-1} and Soman -90.0 kJ mol^{-1}, this structure is highly CWA selective. Next, we measured the breakthrough curve for DES adsorption of [Ni$_3$(BTP)$_2$] at room temperature and 80% RH (Scheme A4. 1 in the Apendix 4) using a 20 mL min^{-1} flow of N$_2$ at RH 80% and 298 K containing 1 ppm of diethylsulfide (DES). Figure 8 shows that the DES reaches the saturation uptake in nearly 8 h, which is translated to an approximate uptake of 0.6 mol kg^{-1}. Moreover, the gas chromatography analysis indicates a significant drop of DES concentration in the eluted gas flow down to *ca.* 0.05 ppm. Consequently, it can be concluded that the DES relative pressure in equilibrium with the MOF material will be *ca.* 0.05 Pa with the adsorbed amount of DES agreeing reasonably well with the computational calculated values at the same range of pressure (0.617-1.193

Figure 8. Breakthrough curve of 20 mL min^{-1} flow of N$_2$ at RH 80% and 298 K containing 1 ppm of diethylsulfide (DES) passed through a chromatographic column packed with 150 mg of [Ni$_3$(BTP)$_2$](CSD code: UTEWOG).

mol kg^{-1} at a pressure between 0.01 and 0.1 Pa).

We finally tested the capacity of the MOF to retain its original adsorption performance. For this, we evaluated the reversibility of the DES adsorption process by means of thermogravimetric analysis (TGA), diffuse reflectance and temperature programed desorption (Figures A4. 10 and A4. 11 in the Apendix 4). The results indicate that DES is coadsorbed with moisture giving rise to a [Ni$_3$(BTP)$_2$]$*$4H$_2$O$*$0.5DES formulation as confirmed by TGA and temperature programed desorption. The higher affinity of the framework toward DES over moisture is confirmed by low temperature of the dehydration process (< 373 K), while DES desorption takes place at *ca.* 473 K. It should also be noted that neither the adsorbed water molecules nor the DES molecules gives rise to any modification of the metal coordination geometry as concluded from diffuse reflectance spectrum (Figure A4. 12 in the Apendix 4); showing an absorption at 450 nm characteristic of d-d transitions of low spin square planar Ni(II) pyrazolate systems [56]. This further suggests that physisorption in the MOF is solely responsible for the selective capture of DES over moisture.

5.4 CONCLUSIONS

In this work, we performed a high-throughput molecular simulation screening to explore the suitability of MOF structures for chemical warfare agent (CWA) protection: mustard, sarin, soman, and their commonly used simulants, and to identify an optimal material for further experimental test. We first selected 1647 out of 2932 MOFs structures provided in the DDEC database, with cavity diameter values larger enough to ensure accessibility of CWAs to the porous network. We then used the Widom insertion technique to evaluate efficiently the strength of the CWA-MOF interactions as a function of structural features such as pore size and surface area. We were able to demonstrate the good agreement between structure-property relationships for CWAs and their respective simulants, providing further support for the simulants use in experimental settings where the application of real CWAs is not possible. In particular, high CWA-MOF interactions were found in MOFs with reasonable high surface area (up to 2000 m^2 g^{-1}), whereas the highest K_H values were localized at between 5 and 6 Å. To minimize competitive water adsorption, we found 156 hydrophobic MOFs (*ca.* 10% of the studied MOFs) based on their water affinity using Widom insertion method. We then ran GCMC simulations for mustard, sarin, soman, and water at different pressures; we found negligible water loadings in the 156

hydrophobic MOFs at 80% of HR, supporting our fast screening approach based on Widom insertion. Out of 156 hydrophobic MOFs, we identified three optimal materials with adsorption capacities of > 4 mol kg^{-1} for sarin, soman and mustard gas. The identified MOFs not only minimize competitive water adsorption due to their hydrophobic nature, but also maximize CWA loading due to their large surface area (> 2000 m^2 g^{-1}) and LCD (> *ca.* 12 Å) values. Remarkably, this high-throughput computational selection is supported by experimental reports. We completed our hierarchical high-throughput materials discovery approach by successfully synthesizing and testing one of the top four structures identified from simulations: [Ni$_3$(BTP)$_2$], CSD code: UTEWOG; breakthrough experiments confirmed selective adsorption of DES from the humid stream. Indeed, the exceptional adsorption selectivity and stability in the presence of humidity provided by experimental results on [Ni$_3$(BTP)$_2$] is evident by the low temperature of the dehydration process and the absence of modifications on the metal coordination geometry showed in the diffuse reflectance spectrum. All in all, inspired by high-throughput computer simulations, our screening approach provides not only synthetic guidelines to make suitable materials for CWA capture but also demonstrates a rare case of materials discovery where a priori knowledge of predicted adsorption capacity leads to oriented designed and efficient identification

of new adsorbent materials.

5.5 Bibliography

[1] Haber, L. F. *The Poisonous Cloud: Chemical Warfare in the First World War*; Oxford University Press: London, 1986.

[2] Decoste, J. B.; Peterson, G. W. *Chemical Reviews* **2014**, *114*, 5695–5727.

[3] Montoro, C.; Linares, F.; Quartapelle Procopio, E.; Senkovska, I.; Kaskel, S.; Galli, S.; Masciocchi, N.; Barea, E.; Navarro, J. A. R. *Journal of the American Chemical Society* **2011**, *133*, 11888–11891.

[4] Enserink, M. *Science* **2013**, *341*, 1050 – 1051.

[5] Smith, B. M. *Chemical Society Reviews* **2008**, *37*, 470–478.

[6] Yang, Y. C.; Baker, J. A.; Ward, J. R. *Chemical Reviews* **1992**, *92*, 1729–1743.

[7] Plonka, A. M.; Wang, Q.; Gordon, W. O.; Balboa, A.; Troya, D.; Guo, W.; Sharp, C. H.; Senanayake, S. D.; Morris, J. R.; Hill, C. L.; Frenkel, A. I. *Journal of the American Chemical Society* **2017**, *139*, 599–602.

[8] Grant Glover, T.; Peterson, G. W.; Schindler, B. J.; Britt, D.; Yaghi, O. *Chemical Engineering Science* **2011**, *66*, 163–170.

[9] Britt, D.; Tranchemontagne, D.; Yaghi, O. M. *Proceedings of the National Academy of Sciences of the United States of America* **2008**, *105*, 11623–11627.

[10] Kim, K. C.; Moghadam, P. Z.; Fairen-Jimenez, D.; Snurr, R. Q. *Industrial & Engineering Chemistry Research* **2015**, *54*, 3257–3267.

[11] Ghosh, P.; Kim, K. C.; Snurr, R. Q. *Journal of Physical Chemistry C* **2014**, *118*, 1102–1110.

[12] Moghadam, P. Z.; Fairen-Jimenez, D.; Snurr, R. Q. *J. Mater. Chem. A* **2015**, *4*, 529–536.

[13] Galli, S.; Masciocchi, N.; Colombo, V.; Maspero, A.; Palmisano, G.; López-Garzón, F. J.; Domingo-Garcia, M.; Fernández-Morales, I.; Barea, E.; Navarro, J. A. R. *Chemistry of Materials* **2010**, *22*, 1664–1672.

[14] Bobbitt, N. S.; Mendonca, M. L.; Howarth, A. J.; Islamoglu, T.; Hupp, J. T.; Farha, O. K.; Snurr, R. Q. *Chem. Soc. Rev.* **2017**, *46*, 3357–3385.

[15] Zhou, H. C.; Long, J. R.; Yaghi, O. M. *Chemical Reviews* **2012**, *112*, 673–674.

[16] Kitagawa, S.; Kitaura, R.; Noro, S.-i. *Angewandte Chemie - International Edition* **2004**, *43*, 2334–2375.

[17] Eddaoudi, M.; Kim, J.; Rosi, N.; Yaghi, O. M. *Science* **2002**, *295*, 469–472.

[18] Furukawa, H.; Cordova, K. E.; O'Keeffe, M.; Yaghi, O. M. *Science* **2013**, *341*.

[19] Tanabe, K. K.; Cohen, S. M. *Chemical Society Reviews* **2011**, *40*, 498–519.

[20] Moghadam, P. Z.; Li, A.; Wiggin, S. B.; Tao, A.; Maloney, A. G. P.; Wood, P. A.; Ward, S. C.; Fairen-Jimenez, D. *Chemistry of Materials* **2017**, *29*, 2618–2625.

[21] Li, J.-R.; Kuppler, R. J.; Zhou, H.-C. *Chemical Society reviews* **2009**, *38*, 1477–1504.

[22] Britt, D.; Furukawa, H.; Wang, B.; Glover, T. G.; Yaghi, O. M. *Proceedings of the National Academy of Sciences of the United States of America* **2009**, *106*, 20637–20640.

[23] Zou, R.; Zhong, R.; Han, S.; Xu, H.; Burrell, A. K.; Henson, N.; Cape, J. L.; Hickmott, D. D.; Timofeeva, T. V.; Larson, T. E.; Zhao, Y. *Journal of the American Chemical Society* **2010**, *132*, 17996–17999.

[24] Padial, N. M.; Quartapelle Procopio, E.; Montoro, C.; López, E.; Oltra, J. E.; Colombo, V.; Maspero, A.; Masciocchi, N.; Galli, S.; Senkovska, I.; Kaskel, S.; Barea, E.; Navarro, J. A. R. *Angewandte Chemie - International Edition* **2013**, *52*, 8290–8294.

[25] Mondloch, J. E.; Katz, M. J.; Isley III, W. C.; Ghosh, P.; Liao, P.; Bury, W.; Wagner, G. W.; Hall, M. G.; DeCoste, J. B.; Peterson, G. W.; Snurr, R. Q.; Cramer, C. J.; Hupp, J. T.; Farha, O. K. *Nat Mater* **2015**, *14*, 512–516.

[26] Moon, S. Y.; Proussaloglou, E.; Peterson, G. W.; DeCoste, J. B.; Hall, M. G.; Howarth, A. J.; Hupp, J. T.; Farha, O. K. *Chemistry - A European Journal* **2016**, *22*, 14864–14868.

[27] Moghadam, P. Z.; Ivy, J. F.; Arvapally, R. K. K.; dos Santos, A. M.; Pearson, J. C.; Zhang, L.; Tyllianakis, E.; Ghosh, P.; Oswald, I. W. H.; Kaipa, U.; Wang, X.; Wilson, A.; Snurr, R. Q.; Omary, M. *Chem. Sci.* **2017**, *00*, 1–12.

[28] Colon, Y. J.; Snurr, R. Q. *Chemical Society Reviews* **2014**, *43*, 5735–5749.

[29] Moghadam, P. Z.; Islamoglu, T.; Goswami, S.; Exley, J.; Fantham, M.; Kaminski, C. F.; Snurr, R. Q.; Farha, O. K.; Fairen-Jimenez, D. *Nature Communications* **2018**, *9*, 1378.

[30] Widom, B. *The Journal of Chemical Physics* **1963**, *39*, 2808.

[31] Chung, Y. G.; Camp, J.; Haranczyk, M.; Sikora, B. J.; Bury, W.; Krungleviciute, V.; Yildirim, T.; Farha, O. K.; Sholl, D. S.; Snurr, R. Q. *Chemistry of Materials* **2014**, *26*, 6185–6192.

[32] Willems, T. F.; Rycroft, C. H.; Kazi, M.; Meza, J. C.; Haranczyk, M. *Microporous and Mesoporous Materials* **2012**, *149*, 134–141.

[33] Bae, Y. S.; Yazaydin, A. O.; Snurr, R. Q. *Langmuir* **2010**, *26*, 5475–5483.

[34] Dubbeldam, D.; Calero, S.; Ellis, D. E.; Snurr, R. Q. *Molecular Simulation* **2016**, *42*, 81–101.

[35] Jorgensen, W. L.; Chandrasekhar, J.; Madura, J. D.; Impey, R. W.; Klein, M. L. *The Journal of Chemical Physics* **1983**, *79*, 926.

[36] Sokkalingam, N.; Kamath, G.; Coscione, M.; Potoff, J. J. *The Journal of Physical Chemistry B* **2009**, *113*, 10292–10297.

[37] Stubbs, J. M.; Potoff, J. J.; Siepmann, J. I. *Journal of Physical Chemistry B* **2004**, *108*, 17596–17605.

[38] Müller, T. J.; Müller-Plathe, F. *Journal of Hazardous Materials* **2009**, *168*, 13–24.

[39] Vishnyakov, A.; Gor, G. Y.; Lee, M. T.; Neimark, A. V. *Journal of Physical Chemistry A* **2011**, *115*, 5201–5209.

[40] Mayo, S. L.; Olafson, B. D.; Goddard, W. A. I. *Journal of Physical chemistry* **1990**, *101*, 8897–8909.

[41] Rappe, A. K.; Casewit, C. J.; Colwell, K. S.; Goddard, W. a.; Skiff, W. M. *Journal of the American Chemical Society* **1992**, *114*, 10024–10035.

[42] Allen, M. P.; Tildesley, D. J. *Computer Simulation of Liquids*; Oxford Clarendon Press: Oxford, 1987.

[43] Nazarian, D.; Camp, J. S.; Sholl, D. S. *Chemistry of Materials* **2016**, *28*, 785–793.

[44] Colombo, V.; Galli, S.; Choi, H. J.; Han, G. D.; Maspero, A.; Palmisano, G.; Masciocchi, N.; Long, J. R. *Chemical Science* **2011**, *2*, 1311.

[45] Schoenecker, P. M.; Carson, C. G.; Jasuja, H.; Flemming, C. J. J.; Walton, K. S. *Industrial & Engineering Chemistry Research* **2012**, *51*, 6513–6519.

[46] Cousinsaintremi, J.; Rémy, T.; Vanhunskerken, V.; Vandeperre, S.; Duerinck, T.; Maes, M.; Devos, D.; Gobechiya, E.; Kirschhock, C. E. A. E. A.; Baron, G. V. V.; Denayer, J. F. M. F. M. *ChemSusChem* **2011**, *4*, 1074–1077.

[47] Spiandore, M.; Piram, A.; Lacoste, A.; Josse, D.; Doumenq, P. *Drug Testing and Analysis* **2014**, *6*, 67–73.

[48] Mérat, S.; Perez, J. P.; Rüttimann, M.; Bordier, E.; Lienhard, A.; Lenoir, B.; Pats, B. *Annales Francaises d'Anesthesie et de Reanimation* **2003**, *22*, 108–118.

[49] Seto, Y.; Kanamori-Kataoka, M.; Tsuge, K.; Ohsawa, I.; Matsushita, K.; Sekiguchi, H.; Itoi, T.; Iura, K.; Sano, Y.; Yamashiro, S. *Sensors and Actuators, B: Chemical* **2005**, *108*, 193–197.

[50] Saxena, A.; Hastings, N. B.; Sun, W.; Dabisch, P. A.; Hulet, S. W.; Jakubowski, E. M.; Mioduszewski, R. J.; Doctor, B. P. *Chemico-Biological Interactions* **2015**, *238*, 161–169.

[51] Jacobsson, S. O.; Cassel, G. E.; Persson, S. a. *Archives of toxicology* **1999**, *73*, 269–73.

[52] Choi, H. J.; DincaÌÈ, M.; Long, J. R. *Journal of the American Chemical Society* **2008**, *130*, 7848–7850.

[53] Howarth, A. J.; Liu, Y.; Li, P.; Li, Z.; Wang, T. C.; Hupp, J. T.; Farha, O. K. *Nature Reviews Materials* **2016**, *1*, 1–15.

[54] Mason, J. A.; Oktawiec, J.; Taylor, M. K.; Hudson, M. R.; Rodriguez, J.; Bachman, J. E.; Gonzalez, M. I.; Cervellino, A.; Guagliardi, A.; Brown, C. M.; Llewellyn, P. L.; Masciocchi, N.; Long, J. R. *Nature* **2015**, *527*, 357–361.

[55] Shearer, G. C.; Colombo, V.; Chavan, S.; Albanese, E.; Civalleri, B.; Maspero, A.; Bordiga, S. *Dalton Transactions* **2013**, *42*, 6450.

[56] Klingele (née Hausmann), J.; Prikhod'ko, A. I.; Leibeling, G.; Demeshko, S.; Dechert, S.; Meyer, F. *Dalton Trans.* **2007**, *20*, 2003–2013.

Conclusions

This thesis explores the use of porous materials as post-production solutions for the capture of a variety of pollutant gases including, post-combustion products, greenhouse gases, and chemical warfare agents. A combination of well-established simulation techniques supported by experimental results are used for this purpose.

The main conclusions of the use of zeolites for adsorption and separation of sulfur pollutants are: (Chapters 2-3)

1.- The highest values of heat of adsorption are observed in structures with the lowest pore volume, regardless of the gas under study. However, structures such as MOR, SBE, and FAU do not follow this trend since they have specific adsorption sites that affect the affinity for the different gases.

2.- Based on low-loading selectivity, MOR and FAU are the structures with the highest selectivity toward SO_2. On the other hand, structures containing specific adsorption sites inaccessible for SF_6 (e.g. MOR, FAU, or EON) exhibit the lowest SF_6/N_2 selectivity.

3.- The adsorption selectivity of the ternary mixture (20:40:40 SO_2, CO_2, and CO, respectively) at room conditions in zeolites shows that structures with the lowest pore volume are the most selective towards SO_2. This is due to a packing effect for SO_2 molecules.

4.- The study of diffusion properties in combination with adsorption selectivity allows discarding some initially promising structures because of the low diffusion of the guest molecules within the pores.

5.- Zeolites with channel-type topology and low pore volume (e.g. JRY and NAT) seem

the most adequate materials for selective capture of SO_2 over CO_2 and CO. On the other hand, SF_6/N_2 separation is more efficient using zeolites that have intersecting channels and windows diameters between 5 and 7 Å (e.g. BEC, ITR, IWW, and SFG).

Results using the full screening procedure and the inclusion of adsorption and diffusion properties at several operation conditions demonstrate that the selection of materials for applications in separations should not be based solely on prediction of low coverage properties such as Henry's constants and heats of adsorption.

With regard to the study of the effect of confinement on the equilibrium chemical reaction between NO_2 and N_2O_4, the most relevant conclusions are: (Chapter 4)

6.- Simulations confirm that the increase of temperature or the decrease of pressure favor the destruction of dimers (N_2O_4).

7.- The confinement in zeolites favors the formation of dimers. This is explained by the increase of the density of the adsorbates in the pore, as well as by the selectivity of the zeolites for the dimer.

8.- The largest differences between the concentration of dimers in the bulk and in the pore are found at low temperature and high pressure. This is due to the high density of the adsorbate inside the pores and the strong effect of confinement under these conditions.

9.- Among the studied zeolites, MFI exerts the most noticeable effect on the equilibrium composition due to its narrow system of channels. On the other hand, the large size of the cages in zeolite FAU reduces the effect of confinement.

10.- The formation of dimer molecules within the confined environment is affected by special structural features such as side-pockets in MOR that selectively adsorb monomer molecules. These features must be explicitly considered for NO_2 adsorption in computational screenings, given that the topology of the structure has been shwon to be crucial.

Chapter 4 demonstrates that the composition of chemical substances involved in reactions can be strongly modified by the confinement in porous materials. Formation or decomposition reactions can be favored by zeolite topology and/or the operation conditions.

Regarding the use of MOFs for chemical warfare agent protection, the main conclusions are: (Chapter 5)

11.- The agreement between low coverage adsorption properties for chemical warfare agent molecules in MOFs and their respective simulants supports the use of the latters in experimental settings.

12.- The use of the Widom insertion method to identify hydrophobic materials that minimize water affinity is supported by obtaining negligible water loadings at 80% relative humidity.

13.- The top three MOFs with the largest adsorption capacity for the chemicals under study exhibit metal-pyrazolate coordinate covalent bonds, that are known to impart high thermal and chemical stability.

14.- Breakthrough experiments in one of the top structures, identified from simulations and synthesized for testing, confirm selective adsorption of diethylsulfide (chemical warfare agent simulant) from a humid stream and also the stability of the structure.

The exceptional adsorption selectivity and stability of the experimentally tested material in the presence of humidity strongly support the utility of the high-throughput computational screening procedure.

All in all, the results presented in this thesis indicate that prediction of materials for separation processes should be based not only on low coverage adsorption properties, but also on the adsorption capacities and transport properties under expected operation conditions. Molecular simulation techniques have proven to be powerful tools for the design, screening, and selection of the most suitable materials for a given capture and/or separation process. Results also confirm the importance of combining simulations and experimental procedures for a realiable selection of materials.

Resumen (Summary in spanish)

En esta tesis se aborda el uso de materiales porosos como soluciones postproductivas para la reducción y eliminación de gases contaminantes tales como óxidos de nitrógeno, óxidos de azufre, dióxido de carbono, hexafluoruro de azufre y agentes de guerra química. Para este fin íntimamente relacionado con la protección del medio ambiente y la mejora de la calidad del aire y la salud, se han utilizado dos familias de materiales con demostrada aplicación actual en este tipo de procesos, como son las zeolitas y los MOFs (del inglés *Metal Organic Frameworks*). Dichas familias de materiales presentan amplia diversidad, ya sea de topológica (en el caso de las zeolitas) y/o estructural (en el caso de los MOFs). En este ámbito, la simulación molecular se perfila como una herramienta esencial no solo para dar una explicación a nivel molecular de los fenómenos que rigen el proceso de captura y separación de los distintos gases, sino también como elemento capaz de probar y cribar un gran número de materiales e incluso diseñar otros nuevos. En este trabajo, se han usado técnicas de simulación molecular bien conocidas y validadas (Monte Carlo y Dinámica Molecular). Por medio de estas técnicas se han estudiado procesos de adsorción y difusión de gases contaminantes en el seno de los materiales porosos anteriormente citados. Los procesos de adsorción/separación concretos que se han abordado en esta tesis son 1) adsorción de gases de combustión y gases de efecto invernadero, incluyendo SO_2, CO_2, SF_6 y CO usando zeolitas 2) el estudio del efecto del confinamiento en la reacción de dimerización del NO_2 y 3) materiales capaces capturar agentes químicos de guerra en presencia de humedad atmosférica para la protección contra eventuales ataques deliberados.

Efecto de la topología en la captura y separación de compuestos gaseosos de azufre (Capítulos 2 y 3):

En este bloque se profundiza en el estudio a nivel molecular del efecto que ejercen una variedad de zeolitas con diferente topología en la captura y separación de compuestos

de azufre (SO_2 y SF_6) que afectan al medio ambiente. Para ello se tienen en cuenta no solo propiedades de adsorción a bajo recubrimiento, sino también propiedades de difusión y selectividades a condiciones de presión y temperatura óptimas para realizar el proceso de separación y captura. Concretamente, en el Capítulo 2 se aborda la captura selectiva de SO_2 sobre CO_2 y CO, una mezcla proveniente de gases de combustión. Por otro lado, el Capítulo 3 pone el foco en mezclas de SF_6 y N_2, comunmente utilizadas en la industria eléctrica como aislante. Cabe destacar que en ambos capítulos se han desarrollado los parámetros de interacción para describir la adsorción de los compuestos de azufre anteriormente citados en zeolitas, ajustando los resultados obtenidos con datos experimentales.

Las principales conclusiones de este bloque de contenidos son:

Los dos compuestos de azufre muestran una interacción más fuerte con las zeolitas que la del resto de gases estudiados, un comportamiento que está relacionado con su tamaño y forma. Por otro lado, las interacciones más fuertes se observan en materiales con menor volumen de poro, aunque hay algunas estructuras concretas que escapan de esta tendencia general debido a la existencia de sitios específicos de adsorción que son capaces de modificar la afinidad por el material a bajo recubrimiento. De este modo, para el SO_2 zeolitas como MOR son las más selectivas. Sin embargo, el mayor tamaño de la molécula de SF_6 hace que esta no pueda acceder a alguno de estos sitios, de forma que las estructuras que los presentan, como por ejemplo MOR, tienen una peor selectividad por este gas. Del estudio de la mezcla ternaria $SO_2/CO_2/CO$ en condiciones ambientales se extrae que el SO_2 es el gas más adsorbido a pesar de hallarse en menor proporción en la mezcla. Por otro lado, del estudio de la mezcla binaria SF_6/N_2 a temperatura ambiente se concluye que el intervalo óptimo de presión está localizado entre 3×10^2-3×10^3 kPa. En ambos capítulos se subraya la importancia de tener en cuenta las propiedades de difusión para la selección de de los materiales más adecuados, llegándose a descartar materiales que habían mostrado una buena selectividad de adsorción por ser muy baja la difusión en ellos. En cuanto a la topología, se concluye que estructuras con sistemas de canales y pequeño volumen de poro son las más adecuadas para la captura selectiva de SO_2 sobre CO_2, mientras que la separación de SF_6 de N_2 es más eficiente utilizando zeolitas con sistemas de canales interconectados con tamaño de poro comprendido entre 5 y 7 Å.

Efecto del confinamiento en el equilibrio de reacciones químicas (Capítulo 4):

El capítulo 4 se centra en identificar el efecto que ejerce el confinamiento sobre reac-

ciones químicas como la del proceso de formación de dímeros a partir de la molécula de NO_2. Se utilizan una serie de zeolitas con distinta topología para hacer un estudio comparativo del equilibrio fuera y dentro de cada una de ellas y su evolución frente a condiciones variables de presión y temperatura.

De este capítulo cabe extraen las siguientes conclusiones:
El confinamiento en zeolitas es responsable de la formación de dímeros debido tanto a un incremento en la densidad del adsorbato como a un comportamiento selectivo del material hacia esta especie. Las mayores modificaciones de las condiciones ideales de equilibrio se observan en zeolitas con canales de diámetro similar a las moléculas de estudio. Por otro lado, la formación de dímeros debida al confinamiento también se ve afectada por la existencia de sitios preferentes de adsorción al aumentar éstos la afinidad de los materiales por las moléculas de monómero a determinadas condiciones de presión y temperatura. Estas particularidades mostradas por algunos materiales deben tenerse en cuenta cuando se trabaje con reacciones químicas similares a la estudiada aqui.

Captura selectiva de agentes de guerra química usando MOFs (Capítulo 5):

En el quinto capítulo de este trabajo se estudia la capacidad que tienen un elevado número de MOFs para capturar gas mostaza, sarin y soman en presencia de humedad atmosférica. Para ello se analiza la hidrofobicidad de los MOFs, seleccionando aquellos que minimicen la adsorción de agua. A partir de éstos se realiza una nueva selección de materiales en base a su capacidad de adsorción para los tres agentes químicos. El proceso finaliza con la síntesis y prueba experimental de uno de los MOFs seleccionados validando así el método computacional de selección.

Las conclusiones más relevantes de este estudio son:
El uso de simulaciones de bajo coste computacional, como la obtención de calores de adsorción y constantes de Henry, para la búsqueda de materiales que minimicen la adsorción de agua queda validado con los resultados obtenidos en condiciones de alta humedad relativa. El propio proceso de selección de materiales usando diferentes metodologías computacionales ha sido finalmente validado por los resultados experimentales obtenidos tras la síntesis y utilización de uno de los materiales seleccionados. Estos resultados experimentales muestran una excelente capacidad adsorción para sulfuro de dietilo, molécula análoga al gas mostaza, en presencia de agua, así como una buena estabilidad del material durante el proceso.

Como conclusión general, los resultados mostrados en esta tesis demuestran la utilidad de la simulación como instrumento para la selección y el diseño de materiales porosos cristalinos capaces de ayudar a paliar algunos de los problemas ambientales que afectan a la sociedad actual. En cuanto al proceso de cribado y selección, los resultados también demuestran que dicho proceso no puede basarse sólo en el estudio de propiedades de adsorción a bajo recubrimiento, sino que además debe incluir simulaciones más complejas y costosas que proporcionen información sobre la capacidad de adsorción y difusión de los materiales en las condiciones de presión y temperatura de interés para cada proceso concreto. Finalmente se destaca la importancia de una buena sinergia entre los procedimientos experimentales y la simulación, herramientas que, como se ha demostrado, se retroalimentan y sirven de ayuda para para seleccionar los materiales más adecuados para cada proceso de captura y separación de gases.

Appendix 1

Associated content of:

Zeolite Screening for the Separation of gas Mixtures Containing SO$_2$, CO$_2$, and CO

Table A1. 1. Topological and geometrical parameters describing pore systems in IZA zeolites. Each structure is characterized in terms of number of pore systems (#PS). For structures with #PS>0, each pore system (PS ID) is characterized in terms of dimensionality (dim), the diameter of the largest spheres included (Di), free (Df), and included along free sphere path (Dif); as well as the character of the pore system (C- channel, IC- interconnected cage).

Zeolite	#PS	PS ID	Di	Df	Dif	dim	PC	Zeolite	#PS	PS ID	Di	Df	Dif	dim	PC
ABW	2	0	3.61	3.10	3.61	1	C	APD	4	0	4.19	3.23	4.19	1	C
		1	3.61	3.10	3.61	1	C			1	4.20	3.23	4.20	1	C
ACO	1	0	3.90	3.16	3.90	3	C			2	4.20	3.23	4.20	1	C
AEI	1	0	6.90	3.44	6.90	3	IC			3	4.19	3.23	4.19	1	C
AEL	2	0	5.22	4.07	5.22	1	C	AST	0						
		1	5.22	4.07	5.22	1	C	ASV	1	0	4.95	4.03	4.95	1	C
AEN	2	0	3.90	3.18	3.90	2	C	ATN	2	0	5.51	3.71	5.51	1	C
		1	3.90	3.18	3.90	2	C			1	5.51	3.71	5.51	1	C
AET	2	0	7.77	7.16	7.77	1	C	ATO	3	0	5.34	5.09	5.34	1	C
		1	7.77	7.16	7.77	1	C			1	5.34	5.09	5.34	1	C
AFG	0									2	5.34	5.09	5.34	1	C
AFI	1	0	7.56	7.02	7.56	1	C	ATS	2	0	6.57	6.36	6.57	1	C
AFN	2	0	4.75	3.09	4.75	1	IC			1	6.57	6.36	6.57	1	C
		1	4.75	3.09	4.75	1	IC	ATT	1	0	4.88	3.39	4.88	2	C
AFO	2	0	5.03	4.33	5.03	1	C	ATV	2	0	3.90	3.04	3.90	1	C
		1	5.03	4.33	5.03	1	C			1	3.90	3.04	3.90	1	C
AFR	2	0	7.82	6.57	7.82	2	C	AWO	4	0	4.49	3.26	4.49	1	C
		1	7.82	6.57	7.82	2	C			1	4.49	3.26	4.49	1	C
AFS	1	0	9.11	5.61	9.11	3	IC			2	4.48	3.26	4.48	1	C
AFT	1	0	7.14	3.28	7.14	3	IC			3	4.48	3.26	4.48	1	C
AFX	1	0	7.11	3.33	7.11	3	IC	AWW	2	0	6.90	3.77	6.90	1	IC
AFY	1	0	7.42	5.50	7.42	3	C			1	6.88	3.77	6.88	1	IC
AHT	0							BCT	0						
ANA	0							BEA	1	0	6.10	5.63	6.10	3	C
APC	0							BEC	1	0	6.23	5.91	6.23	3	C

Table A1.2. Topological and geometrical parameters describing pore systems in IZA zeolites. Each structure is characterized in terms of number of pore systems (#PS). For structures with #PS>0, each pore system (PS ID) is characterized in terms of dimensionality (dim), the diameter of the largest spheres included (Di), free (Df), and included along free sphere path (Dif); as well as the character of the pore system (C- channel, IC- interconnected cage).

Zeolite	#PS	PS ID	Di	Df	Dif	dim	PC	Zeolite	#PS	PS ID	Di	Df	Dif	dim	PC
BIK	2	0	3.76	3.14	3.76	1	C	CON	1	0	6.77	5.20	6.77	3	C
		1	3.76	3.14	3.76	1	C	CZP	1	0	3.75	3.24	3.75	1	C
BOF	2	0	5.15	4.18	5.15	1	C	DAC	2	0	4.79	3.40	4.79	2	C
		1	5.15	4.17	5.15	1	C			1	4.79	3.40	4.79	2	C
BOG	1	0	7.49	6.48	7.49	3	C	DDR	3	0	7.06	3.25	7.06	2	IC
BPH	1	0	9.11	5.61	9.11	3	IC			1	7.06	3.25	7.06	2	IC
BRE	0									2	7.06	3.25	7.06	2	IC
BSV	2	0	4.76	3.44	4.76	3	C	DFO	1	0	10.89	6.79	10.89	3	IC
		1	4.76	3.44	4.76	3	C	DFT	1	0	4.18	3.25	4.18	1	C
CAN	1	0	5.76	5.42	5.76	1	C	DOH	0						
CAS	0							DON	2	0	8.17	7.67	8.17	1	C
CDO	2	0	4.97	3.04	4.97	2	IC			1	8.17	7.67	8.17	1	C
		1	4.97	3.04	4.97	2	IC	EAB	2	0	6.62	3.14	6.62	2	IC
CFI	2	0	7.07	6.86	7.07	1	C			1	6.61	3.14	6.61	2	IC
		1	7.07	6.86	7.07	1	C	EDI	1	0	4.86	3.04	4.86	1	IC
CGF	0							EMT	1	0	10.99	6.97	10.99	3	IC
CGS	2	0	5.30	3.61	5.30	1	C	EON	3	0	5.60	2.84	5.60	2	IC
		1	5.31	3.61	5.31	1	C			1	7.27	6.39	7.27	1	C
CHA	1	0	6.74	3.32	6.74	3	IC			2	7.27	6.39	7.27	1	C
CHI	4	0	3.51	3.23	3.51	1	C	EPI	2	0	4.92	3.22	4.92	2	IC
		1	3.51	3.23	3.51	1	C			1	4.92	3.22	4.92	2	IC
		2	3.51	3.23	3.51	1	C	ERI	1	0	6.3	3.02	6.3	3	IC
		3	3.51	3.23	3.51	1	C	ESV	2	0	5.67	3.25	5.67	1	IC
CLO	2	0	15.32	5.91	15.32	3	IC			1	5.67	3.26	5.67	1	IC
		1	10.18	3.79	10.18	3	IC	ETR	1	0	9.61	8.92	9.61	1	C
EUO	2	0	6.26	4.54	6.26	1	C	ISV	1	0	6.36	5.78	6.36	3	C
		1	6.26	4.54	6.26	1	C	ITE	4	0	7.77	3.81	7.77	1	IC
EZT	2	0	5.90	5.61	5.90	1	C			1	7.77	3.81	7.77	1	IC
		1	5.91	5.61	5.91	1	C			2	7.77	3.81	7.77	1	IC
FAR	0									3	7.77	3.81	7.77	1	IC
FAU	1	0	10.70	6.95	10.70	3	IC	ITH	1	0	6.28	4.67	6.28	3	C
FER	2	0	5.41	4.29	5.16	2	C	ITR	1	0	5.96	4.71	5.96	3	C
		1	5.41	4.29	5.16	2	C	ITW	2	0	4.16	3.47	4.16	1	C
FRA	0									1	4.16	3.47	4.16	1	C
GIS	1	0	4.57	2.87	4.57	3	IC	IWR	1	0	6.90	5.51	6.90	3	C
GIU	0						C	IWS	1	0	7.62	6.26	7.62	3	C
GME	1	0	7.11	6.68	7.11	3	C	IWV	2	0	8.12	6.63	8.12	2	C
GON	2	0	5.66	4.87	5.66	1	C			1	8.12	6.63	8.12	2	C
		1	5.66	4.87	5.66	1	C	IWW	1	0	6.55	5.84	6.55	3	C
GOO	0							JBW	1	0	3.85	3.32	3.85	1	C
HEU	4	0	5.21	3.27	5.21	1	IC	JRY	2	0	4.10	3.72	4.10	1	C
		1	4.68	3.10	4.68	1	IC			1	4.10	3.72	4.10	1	C
		2	4.68	3.10	4.68	1	IC	KFI	1	0	10.17	3.64	10.17	3	IC
		3	5.21	3.27	5.21	1	IC	LAU	2	0	5.47	3.67	5.47	1	C
IFR	2	0	6.56	5.98	6.56	1	C			1	5.47	3.67	5.47	1	C
		1	6.56	5.98	6.56	1	C	LEV	3	0	6.39	3.13	6.39	2	IC
IHW	2	0	6.07	3.27	6.07	2	IC			1	6.39	3.13	6.39	2	IC
		1	6.07	3.27	6.07	2	IC			2	6.39	3.13	6.39	2	IC
IMF	2	0	6.68	4.87	6.68	2	C	LIO	0						
		1	6.68	4.87	6.68	2	C	LIT	0						

Table A1. 3. Topological and geometrical parameters describing pore systems in IZA zeolites. Each structure is characterized in terms of number of pore systems (#PS). For structures with #PS>0, each pore system (PS ID) is characterized in terms of dimensionality (dim), the diameter of the largest spheres included (Di), free (Df), and included along free sphere path (Dif); as well as the character of the pore system (C- channel, IC- interconnected cage).

Zeolite	#PS	PS ID	Di	Df	Dif	dim	PC	Zeolite	#PS	PS ID	Di	Df	Dif	dim	PC
LOS	0							MRE	2	0	5.73	5.19	5.73	1	C
LOV	1	0	4.25	3.38	3.73	3	C			1	5.73	5.18	5.73	1	C
LTA	1	0	10.24	3.81	10.24	3	IC	MSE	1	0	6.49	5.98	6.49	3	C
LTF	2	0	7.76	7.1	7.76	1	C	MSO	0						
		1	6.51	6.00	6.51	3	C	MTF	2	0	5.58	3.63	5.58	1	IC
LTL	1	0	9.61	7.10	9.61	1	C			1	5.58	3.63	5.58	1	IC
LTN	0							MTN	0						
MAR	0							MTT	2	0	5.52	4.55	5.52	1	C
MAZ	2	0	7.69	7.10	7.69	1	C			1	5.52	4.54	5.52	1	C
		1	5.63	2.85	5.63	3	IC	MTW	2	0	5.31	5.08	5.31	1	C
MEI	1	0	7.66	6.45	7.66	1	C			1	5.31	5.08	5.31	1	C
MEL	1	0	6.87	4.77	6.87	3	C	MVY	0						
MEP	0							MWW	2	0	9.29	3.98	9.29	2	IC
MER	4	0	6.25	3.80	6.25	1	IC			1	5.73	4.17	5.73	2	C
		1	3.59	2.80	3.59	1	C	NAB	1	0	3.76	3.09	3.76	3	C
		2	6.25	3.80	6.25	1	IC	NAT	4	0	3.95	3.84	3.95	1	C
		3	3.59	2.80	3.59	1	C			1	3.95	3.84	3.95	1	C
MFI	1	0	5.94	4.28	5.94	3	C			2	3.95	3.84	3.95	1	C
MFS	2	0	6.21	4.94	6.21	1	C			3	3.95	3.84	3.95	1	C
		1	6.21	4.94	6.21	1	C	NES	2	0	6.17	4.66	6.17	2	C
MON	1	0	3.74	3.13	3.74	3	C			1	6.17	4.66	6.17	2	C
MOR	2	0	6.20	6.03	6.20	1	C	NON	0						
		1	6.20	6.03	6.20	1	C	NPO	1	0	3.34	3.10	3.34	1	C
MOZ	2	0	9.63	7.14	9.63	1	C	NSI	2	0	3.45	2.87	3.45	1	C
		1	6.50	6.05	6.48	3	C			1	3.45	2.87	3.45	1	C
OBW	1	0	8.86	4.78	8.86	3	IC	RWR	4	0	3.92	2.83	3.92	1	C
OFF	1	0	6.49	6.04	6.49	3	C			1	3.92	2.83	3.92	1	C
OSI	2	0	6.26	5.88	6.26	1	C			2	3.92	2.83	3.92	1	C
		1	6.26	5.88	6.26	1	C			3	3.92	2.83	3.92	1	C
OSO	1	0	5.67	5.47	5.67	3	C	RWY	1	0	14.00	5.89	14.00	3	IC
OWE	1	0	5.20	3.38	5.20	2	IC	SAF	2	0	6.23	5.73	6.23	1	C
PAR	2	0	3.68	3.19	3.68	1	C			1	6.23	5.73	6.23	1	C
		1	3.68	3.19	3.68	1	C	SAO	1	0	8.22	6.28	8.22	3	C
PAU	3	0	10.08	3.66	10.08	3	IC	SAS	2	0	8.53	3.82	8.53	1	IC
		1	6.22	3.30	6.22	3	IC			1	8.54	3.82	8.54	1	IC
		2	10.08	3.66	10.08	3	IC	SAT	1	0	6.17	2.85	6.17	3	IC
PHI	2	0	5.00	3.23	5.00	2	IC	SAV	1	0	8.28	3.70	8.28	3	IC
		1	5.00	3.23	5.00	2	IC	SBE	2	0	12.09	6.81	12.09	3	IC
PON	2	0	4.50	3.90	4.50	1	C			1	12.09	6.81	12.09	3	IC
		1	4.50	3.90	4.50	1	C	SBN	2	0	4.39	3.40	4.39	2	C
PUN	1	0	4.98	3.95	4.97	3	C			1	4.40	3.40	4.40	2	C
RHO	2	0	10.03	3.66	10.03	3	IC	SBS	1	0	10.97	6.87	10.97	3	IC
		1	10.03	3.66	10.03	3	IC	SBT	1	0	10.39	6.94	10.38	3	C
RRO	2	0	3.87	3.51	3.87	1	C	SFE	1	0	6.23	5.81	6.23	1	C
		1	3.87	3.51	3.87	1	C	SFF	2	0	7.07	4.94	7.07	1	C
RSN	2	0	4.24	3.37	3.73	2	C			1	7.08	4.94	7.08	1	C
		1	4.24	3.37	3.73	2	C	SFG	1	0	6.35	4.98	6.35	2	C
RTE	2	0	6.40	3.58	6.40	1	IC	SFH	4	0	7.66	6.36	7.66	1	C
		1	6.40	3.58	6.40	1	IC			1	7.66	6.36	7.66	1	C
RTH	2	0	7.63	3.74	7.63	1	IC			2	7.66	6.35	7.66	1	C
		1	7.63	3.74	7.63	1	IC			3	7.66	6.35	7.66	1	C
RUT	0							SFN	2	0	7.46	6.30	7.46	1	C
										1	7.46	6.30	7.46	1	C

Table A1. 4. Topological and geometrical parameters describing pore systems in IZA zeolites. Each structure is characterized in terms of number of pore systems (#PS). For structures with #PS>0, each pore system (PS ID) is characterized in terms of dimensionality (dim), the diameter of the largest spheres included (Di), free (Df), and included along free sphere path (Dif); as well as the character of the pore system (C- channel, IC- interconnected cage).

Zeolite	#PS	PS ID	Di	Df	Dif	dim	PC	Zeolite	#PS	PS ID	Di	Df	Dif	dim	PC
SFO	2	0	7.48	6.55	7.48	2	C	TOL	0						
		1	7.48	6.55	7.48	2	C	TON	2	0	5.04	4.65	5.04	1	C
SFS	1	0	7.03	5.47	7.03	2	C			1	5.04	4.65	5.04	1	C
SGT	0							TSC	1	0	15.86	3.68	15.85	3	IC
SIV	1	0	4.98	3.28	4.98	3	IC	TUN	1	0	8.04	4.99	8.04	3	IC
SOD	0							UEI	4	0	5.11	3.36	5.11	1	IC
SOF	1	0	4.74	3.82	4.74	3	C			1	5.11	3.36	5.11	1	IC
SOS	2	0	4.38	3.81	4.38	1	C			2	5.11	3.36	5.11	1	IC
		1	4.38	3.82	4.38	1	C			3	5.11	3.36	5.11	1	IC
SSF	1	0	7.26	5.76	7.26	2	C	UFI	2	0	9.69	3.49	9.69	2	IC
SSY	2	0	6.92	5.54	6.92	1	C			1	9.69	3.49	9.69	2	IC
		1	6.93	5.53	6.93	1	C	UOS	2	0	5.30	3.73	5.30	1	C
STF	2	0	7.22	5.04	7.22	1	C			1	5.30	3.74	5.30	1	C
		1	7.22	5.04	7.22	1	C	UOZ	0						
STI	4	0	5.81	4.53	5.81	1	C	USI	2	0	6.32	5.84	6.32	2	C
		1	5.81	4.54	5.81	1	C			1	6.32	5.84	6.32	2	C
		2	5.81	4.54	5.81	1	C	UTL	2	0	8.70	7.12	8.70	2	C
		3	5.81	4.54	5.81	1	C			1	8.70	7.12	8.70	2	C
STO	4	0	6.40	5.35	6.4	1	C	VET	1	0	5.99	5.58	5.99	1	C
		1	5.75	4.96	5.75	1	C	VFI	1	0	11.4	10.99	11.4	1	C
		2	6.31	5.61	6.31	1	C	VNI	0						
		3	6.35	5.39	6.35	1	C	VSV	4	0	3.73	3.37	3.73	2	C
STT	2	0	6.56	3.66	6.56	1	IC			1	3.73	3.37	3.73	2	C
		1	6.56	3.66	6.56	1	IC			2	3.73	3.37	3.73	2	C
STW	1	0	4.90	4.48	4.90	3	C			3	3.73	3.37	3.72	2	C
SVR	1	0	5.34	4.55	5.34	3	C	WEI	1	0	3.79	3.03	3.79	3	C
SZR	1	0	5.58	4.29	5.58	3	C	WEN	1	0	4.96	3.62	4.96	2	C
TER	2	0	6.17	4.68	6.17	2	C	YUG	0						
		1	6.17	4.68	6.16	2	C	ZON	2	0	5.20	3.12	5.20	1	IC
THO	2	0	4.47	3.29	4.47	1	C			1	5.20	3.12	5.20	1	IC
		1	4.48	3.29	4.48	1	C								

Table A1.5. Unit cell length and angle, pore volume, surface area, and references of the crystallographic positions of some representative zeolites used in this study. The selection is based on pore character and pore space dimensionality.

Zeolite	Crystallographic positions	Unit Cell			Angles Unit Cell			Pore Volume	SSA (Helium)
		a (Å)	b (Å)	c (Å)	α (°)	β (°)	γ (°)	(cm³/g)	(m²/g)
ASV	Baerlocher et al.	8.67	8.67	13.92	90	90	90	0.10	305.30
DON	Wessels et al.	14.97	8.48	30.03	90	102.65	90	0.17	508.77
ITW	Baerlocher et al.	10.45	15.03	8.95	90	90	90	0.10	382.27
JRY	Baerlocher et al.	8.17	9.20	17.29	90	90	90	0.09	333.56
LAU	Artioli and Stahl	14.85	13.17	7.54	90	110.32	90	0.13	471.29
LTL	Newsam	18.47	18.47	7.48	90	90	120	0.17	553.03
MOR	Gramlich	18.11	20.53	7.53	90	90	90	0.15	477.93
NAT	Baerlocher et al.	13.85	13.85	6.42	90	90	90	0.12	436.30
PON	Baerlocher et al.	8.91	9.21	16.09	90	90	90	0.09	329.22
AFR	Baerlocher et al.	22.31	13.57	6.97	90	90	90	0.25	817.97
FER	Morris et al.	18.72	14.07	7.42	90	90	90	0.13	407.45
IWV	Baerlocher et al.	27.83	26.08	13.94	90	90	90	0.27	883.36
NES	Baerlocher et al.	26.06	13.88	22.86	90	90	90	0.19	701.99
SFO	Baerlocher et al.	22.59	12.57	6.97	90	99.02	90	0.25	815.75
SFG	Baerlocher et al.	25.53	12.58	13.07	90	90	90	0.14	494.75
TER	Baerlocher et al.	9.81	23.65	20.24	90	90	90	0.18	647.26
AFY	Baerlocher et al.	12.33	12.33	8.60	90	90	120	0.29	1208.05
BEC	Baerlocher et al.	12.77	12.77	12.98	90	90	90	0.28	979.93
BOG	Pluth and Smith	20.24	23.80	12.80	90	90	90	0.24	817.50
MEL	Fyfe et al.	20.07	20.07	13.41	90	90	90	0.15	544.96
MFI	van Koningsveld et al.	20.02	19.90	13.38	90	90	90	0.16	547.66
ITR	Baerlocher et al.	11.67	21.97	25.17	90	90	90	0.16	572.09
SBT	Baerlocher et al.	17.19	17.19	41.03	90	90	120	0.34	1057.79
STW	Baerlocher et al.	11.89	11.89	29.92	90	90	120	0.20	804.89
SZR	Baerlocher et al.	18.87	14.40	7.51	90	90	90	0.12	398.51
ITQ-3	Camblor et al.	20.62	9.72	19.62	90	90	90	0.23	693.71
MTF	Baerlocher et al.	9.63	30.39	7.25	90	90.45	90	0.09	263.69
SAS	Baerlocher et al.	14.35	14.35	10.40	90	90	90	0.26	794.61
DDR	Gies	13.86	13.86	40.89	90	90	120	0.14	400.48
LEV	Merlino and Alberti	13.34	13.34	23.01	90	90	120	0.15	706.26
MWW	Baerlocher et al.	14.39	14.39	25.20	90	90	120	0.23	801.23
CHA	Calligaris et al.	9.46	9.46	9.46	94.1	94.1	94.1	0.25	893.81
ERI	Gard et al.	13.27	13.27	15.05	90	90	120	0.22	716.96
FAU	Hriljac et al.	24.26	24.26	24.26	90	90	90	0.33	1020.96
ITQ-29	Corma et al.	11.87	11.87	11.87	90	90	90	0.29	849.36
KFI	Parise et al.	18.67	18.67	18.67	90	90	90	0.23	786.75
PAU	Gordon et al.	35.09	35.09	35.09	90	90	90	0.16	538.21
RHO	McCusker and Baerlocher	15.03	15.03	15.03	90	90	90	0.25	783.40
SBE	Baerlocher et al.	18.53	18.53	27.13	90	90	90	0.32	938.11

Table A1.6. Computed amount of adsorbed molecules and adsorption selectivity from the ternary mixture (SO_2/CO_2/CO with ratio 20:40:40). These values were taken from the adsorption isotherms obtained from Monte Carlo simulations at room conditions for temperature and pressure.

Zeolite	SO_2 loading (mol kg^{-1})	CO_2 loading (mol kg^{-1})	CO loading (mol kg^{-1})	S SO_2/CO_2	S CO_2/CO
ASV	1.750	0.040	0.005	86.761	8.730
DON	1.062	0.235	0.016	9.029	14.816
ITW	2.810	0.024	0.008	238.558	3.018
JRY	2.682	0.021	0.002	256.479	9.693
LAU	2.226	0.107	0.003	41.689	31.387
LTL	1.412	0.245	0.014	11.547	17.406
MOR	2.472	0.164	0.004	30.059	40.659
NAT	3.829	0.052	0.007	147.817	7.755
PON	2.620	0.021	0.002	247.229	8.635
AFR	3.055	0.341	0.016	17.928	21.103
FER	2.295	0.021	0.001	220.820	20.079
IWV	3.033	0.362	0.016	16.744	22.008
NES	1.791	0.331	0.010	10.822	33.355
SFO	2.830	0.359	0.017	15.754	20.809
SFG	1.925	0.119	0.005	32.325	26.184
TER	2.924	0.160	0.003	36.443	53.852
AFY	6.780	0.084	0.006	161.626	14.905
BEC	2.097	0.481	0.020	8.723	23.992
BOG	2.528	0.393	0.012	12.855	31.683
MEL	2.594	0.054	0.002	95.872	35.978
MFI	2.748	0.055	0.001	100.558	47.259
ITR	2.321	0.149	0.006	31.163	24.254
SBT	0.968	0.324	0.039	5.980	8.388
STW	4.519	0.037	0.003	247.469	13.430
SZR	2.407	0.036	0.003	133.290	12.950
ITQ-3	3.116	0.259	0.004	24.059	71.405
MTF	1.249	0.047	0.002	52.800	21.257
SAS	2.335	0.415	0.016	11.244	25.918
DDR	1.610	0.133	0.003	24.137	52.881
LEV	1.928	0.367	0.009	10.501	40.805
MWW	2.933	0.264	0.010	22.198	26.446
CHA	2.409	0.369	0.013	13.057	27.801
ERI	2.191	0.252	0.008	17.371	32.525
FAU	0.803	0.278	0.035	5.778	7.925
ITQ-29	2.673	0.384	0.017	13.916	22.950
KFI	2.091	0.397	0.011	10.528	35.640
PAU	2.179	0.191	0.006	22.830	31.904
RHO	1.090	0.310	0.024	7.029	13.069
SBE	1.173	0.228	0.036	10.271	6.430

Table A1. 7. Computed amount of adsorbed molecules and adsorption selectivity from the binary equimolar mixture (CO_2/CO). These values were taken from the adsorption isotherms obtained from Monte Carlo simulations at room conditions for temperature and pressure.

Zeolite	CO_2 loading (mol kg^{-1})	CO loading (mol kg^{-1})	S CO_2/CO	Zeolite	CO_2 loading (mol kg^{-1})	CO loading (mol kg^{-1})	S CO_2/CO
ITW	0.611	0.048	12.787	MTF	0.710	0.013	55.363
JRY	1.127	0.042	27.092	SAS	0.873	0.065	13.469
MOR	0.513	0.094	5.477	DDR	0.946	0.026	36.461
FER	1.451	0.035	41.730	LEV	1.116	0.051	21.680
SFG	0.823	0.034	23.958	MWW	1.148	0.053	21.579
TER	1.241	0.062	20.024	CHA	0.915	0.061	14.923
MEL	1.619	0.034	47.466	FAU	0.255	0.046	5.567
MFI	1.551	0.042	36.630	PAU	0.832	0.047	17.742
STW	1.840	0.060	30.782	RHO	0.384	0.054	7.160
ITQ-3	1.252	0.061	20.450	SBE	0.406	0.059	6.918
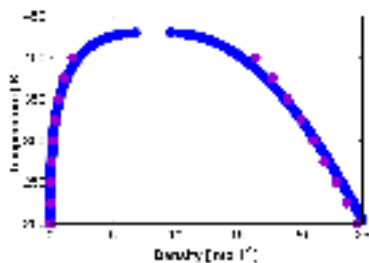
Figure A1.1. Vapor-liquid equilibrium curve of sulfur dioxide: Comparison of experimental (blue) and simulation data (purple). Note that the force field performs well even near the critical point, where it is well established that Gibbs Ensemble Monte Carlo provides values with large error bars.
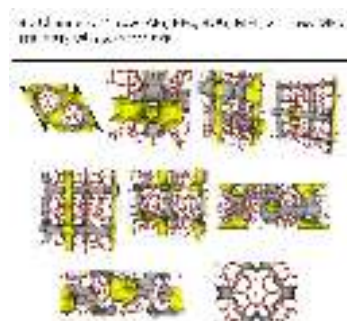
Figure A1.3. Pore landscapes of the selected 3D channels-type zeolites. The inner surface of the pores is highlighted in yellow. The color codes for atoms are red and beige for oxygen and silicon, respectively.
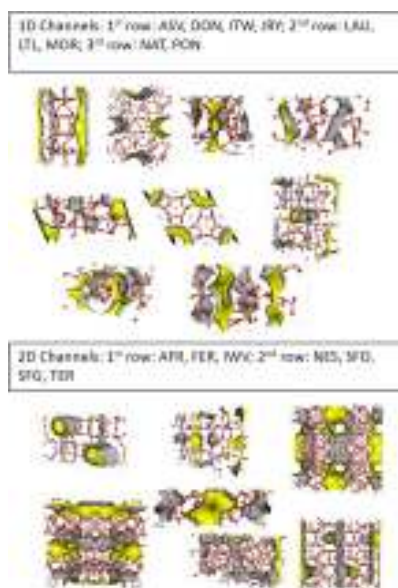
Figure A1.2. Pore landscapes of the selected 1D and 2D channels-type zeolites. The inner surface of the pores is highlighted in yellow. The color codes for atoms are red and beige for oxygen and silicon, respectively.
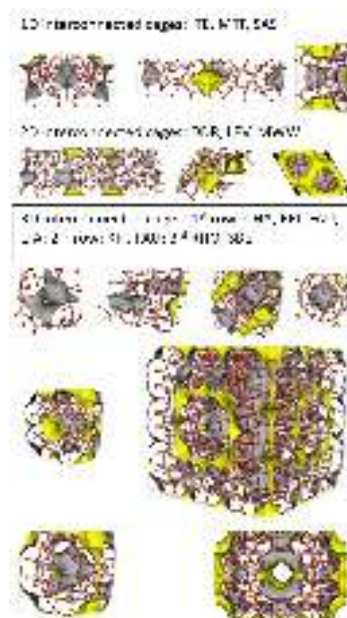
Figure A1.4. Pore landscapes of the selected zeolites of three considered classes of interconnected cages. The inner surface of the pores is highlighted in yellow. The color codes for atoms are red and beige for oxygen and silicon, respectively.
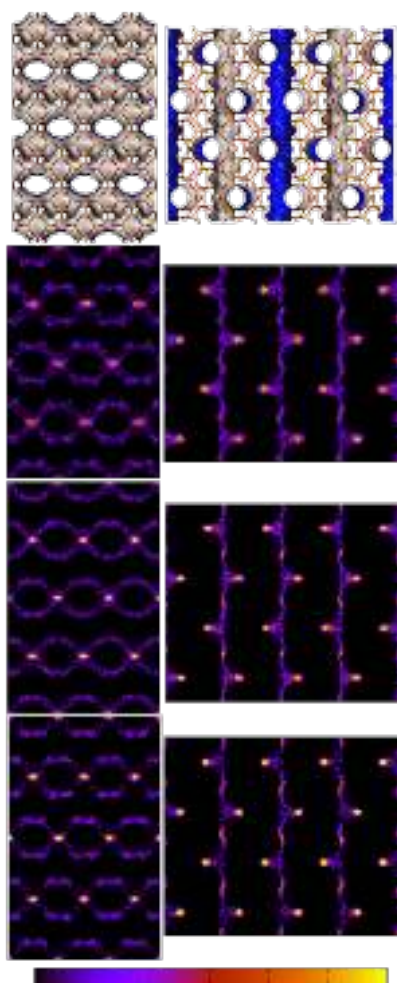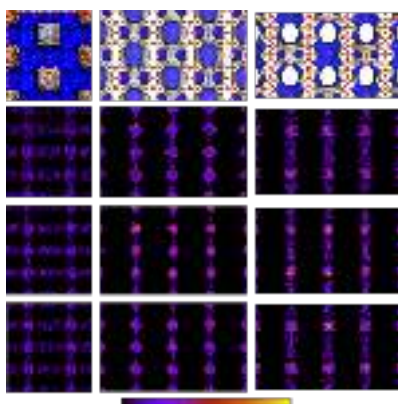
Figure A1. 5. Average occupation profiles of carbon monoxide (second row), carbon dioxide (third row), and sulfur dioxide (fourth row) obtained for one molecule in TER zeolite. The figure shows the projection of the center of mass of the molecules over the x-y (left), and y-z (right) planes. The color graduation indicates the occupational density (from black to yellow). To guide the view we add a representation of the structure (first row). The atomic structure is represented by the oxygen and silica atoms in red and yellow respectively. A grid surface is also depicted (where the accessible part is colored in blue and the non-accessible part is colored in gray).
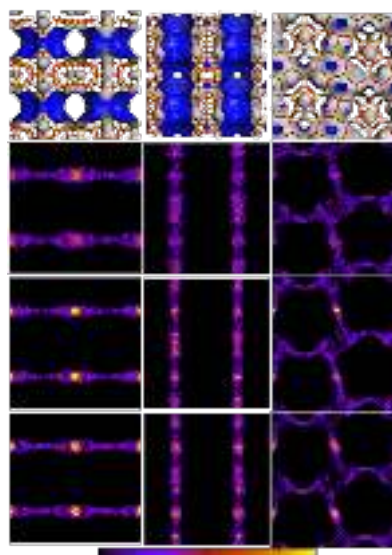
Figure A1. 6. Average occupation profiles of carbon monoxide (second row), carbon dioxide (third row), and sulfur dioxide (fourth row) obtained for one molecule in SFG zeolite. The figure shows the projection of the center of mass of the molecules over the x-y (left), y-z (middle), and x-z (right) planes. The color graduation indicates the occupational density (from black to yellow). To guide the view we add a representation of the structure (first row). The atomic structure is represented by the oxygen and silica atoms in red and yellow respectively. A grid surface is also depicted (where the accessible part appears in blue and the non-accessible part is colored in gray).
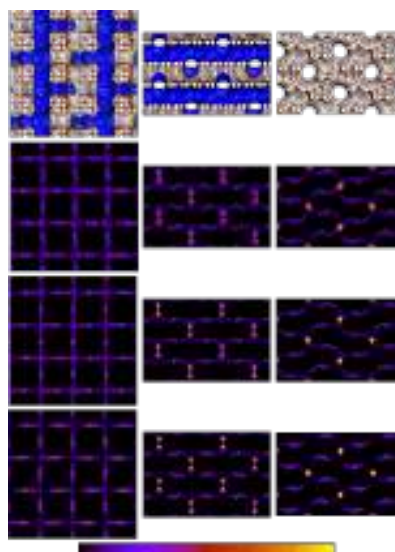
Figure A1. 7. Average occupation profiles of carbon monoxide (second row), carbon dioxide (third row), and sulfur dioxide (fourth row) obtained for one molecule in NES zeolite. The figure shows the projection of the center of mass of the molecules over the x-y (left), z-y (middle), and z-x (right) planes. The color graduation indicates the occupational density (from black to yellow). To guide the view we add a representation of the structure (first row). The atomic structure is represented by the oxygen and silica atoms in red and yellow respectively. A grid surface is also depicted (where the accessible part appears in blue and the non-accessible part is colored in gray).

Figure A1. 8. Average occupation profiles of carbon monoxide (second row), carbon dioxide (third row), and sulfur dioxide (fourth row) obtained for one molecule in MFI zeolite. The figure shows the projection of the center of mass of the molecules over the x-y (left), y-z (middle), and x-z (right) planes. The color graduation indicates the occupational density (from black to yellow). To guide the view we add a representation of the structure (first row). The atomic structure is represented by the oxygen and silica atoms in red and yellow respectively. A grid surface is also depicted (where the accessible part is colored in blue and the non-accessible part is colored in gray).
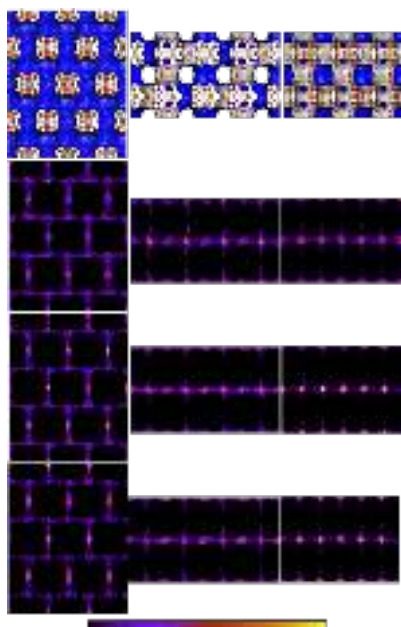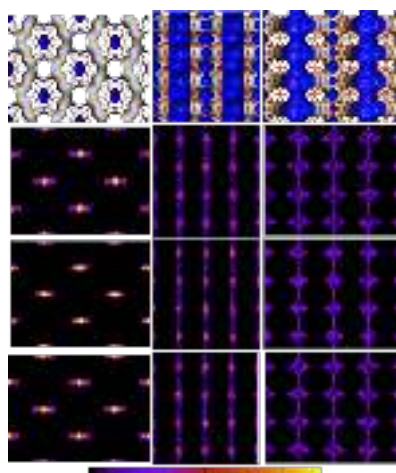
Figure A1. 9. Average occupation profiles of carbon monoxide (second row), carbon dioxide (third row), and sulfur dioxide (fourth row) obtained for one molecule in ITR zeolite. The figure shows the projection of the center of mass of the molecules over the x-y (left), y-z (middle), and x-z (right) planes. The color graduation indicates the occupational density (from black to yellow). To guide the view we add a representation of the structure (first row). The atomic structure is represented by the oxygen and silica atoms in red and yellow respectively. A grid surface is also depicted (where the accessible part appears in blue and the non-accessible part is colored in gray).

Figure A1. 10. Average occupation profiles of carbon monoxide (second row), carbon dioxide (third row), and sulfur dioxide (fourth row) obtained for one molecule in SZR zeolite. The figure shows the projection of the center of mass of the molecules over the x-y (left), y-z (middle), and x-z (right) planes. The color graduation indicates the occupational density (from black to yellow). To guide the view we add a representation of the structure (first row). The atomic structure is represented by the oxygen and silica atoms in red and yellow respectively. A grid surface is also depicted (where the accessible part appears in and while the non-accessible part is colored in gray).
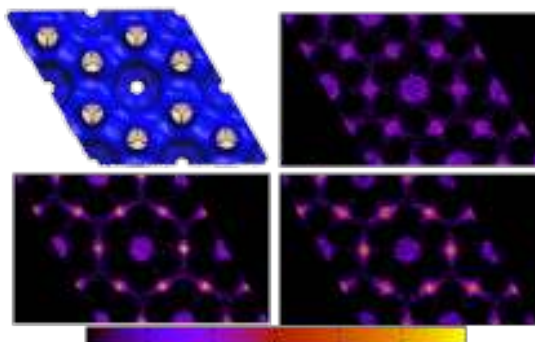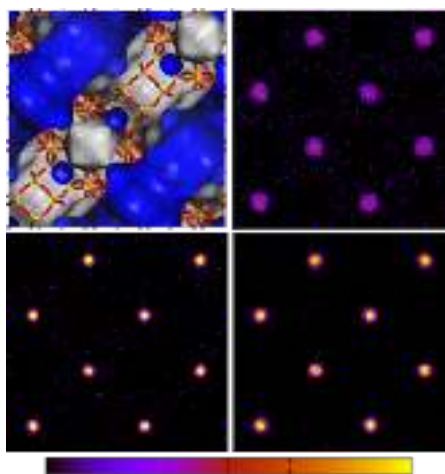
Figure A1. 11. Average occupation profiles of carbon monoxide (top right), carbon dioxide (bottom left), and sulfur dioxide (bottom right) computed for one molecule in MWW zeolite. The figure shows the projection of the center of mass of the molecules over the x-y plane. The color graduation indicates the occupational density (from black to yellow). To guide the view we add a representation of the structure (top left). The atomic structure is represented by oxygen and silica atoms in red and yellow respectively. A grid surface is also depicted, where the accessible part appears in blue and the non-accessible part is colored in gray).

Figure A1. 12. Average occupation profiles of carbon monoxide (top right), carbon dioxide (bottom left), and sulfur dioxide (bottom right) computed for one molecule in FAU zeolite. The figure shows the projections of the center of mass of the molecules over the x-y plane. The color graduation indicates the occupational density (from black to yellow). To guide the view we add a representation of the structure (top left). The atomic structure is represented by the oxygen and silica atoms in red and yellow respectively. A grid surface is also depicted (where the accessible part is colored in blue and the non-accessible part is colored in gray).

Associated content of:

Zeolites for the selective adsorption of sulfur hexafluoride

Table A2.1. Unit cell length and angle, pore volume, surface area, and references of the crystallographic positions of zeolites used in this study.

Zeolite	Crystallographic positions	Unit Cell			Angles Unit Cell			Pore Volume	SSA (Helium)
		a (Å)	b (Å)	c (Å)	α (°)	β (°)	γ (°)	(cm^3/g)	(m^2/g)
AFR	1	22.31	13.57	6.97	90	90	90	0.249	818.00
AFY	1	12.33	12.33	8.60	90	90	120	0.295	1208.05
ASV	1	8.67	8.67	13.92	90	90	90	0.096	305.30
BEC	1	12.77	12.77	12.98	90	90	90	0.284	979.93
BOG	2	20.24	23.80	12.80	90	90	90	0.240	817.50
CFI	1	13.96	5.26	25.97	90	90	90	0.149	456.56
CHA	3	9.46	9.46	9.46	94.07	94.07	94.07	0.253	893.81
DDR	4	13.86	13.86	40.89	90	90	120	0.140	400.48
DON	5	14.97	8.48	30.03	90	102.65	90	0.167	508.77
EMT	1	17.22	17.22	28.08	90	90	120	0.340	1030.19
EON	1	7.57	18.15	25.93	90	90	90	0.164	378.34
ERI	6	13.27	13.27	15.05	90	90	120	0.219	716.96
FAU	7	24.26	24.26	24.26	90	90	90	0.332	1020.96
FER	8	18.72	14.07	7.42	90	90	90	0.129	407.45
ITQ-29	9	11.87	11.87	11.87	90	90	90	0.286	849.36
ITQ-3	10	20.62	9.72	19.62	90	90	90	0.227	693.71
ITR	1	11.67	21.97	25.17	90	90	90	0.155	572.09
ITW	1	10.45	15.03	8.95	90	105.64	90	0.102	382.27
IWW	1	41.69	12.71	12.71	90	90	90	0.197	883.36
JRY	1	8.17	9.20	17.29	90	90	90	0.094	333.56
KFI	11	18.67	18.67	18.67	90	90	90	0.233	786.75
LAU	12	14.85	13.17	7.54	90	110.32	90	0.133	471.29
LEV	13	13.34	13.34	23.01	90	90	120	0.219	706.26
LTL	14	18.47	18.47	7.48	90	90	120	0.168	553.03
MEL	15	20.07	20.07	13.41	90	90	90	0.154	544.96
MFI	16	20.02	19.90	13.38	90	90	90	0.164	547.66
MOR	17	18.11	20.53	7.53	90	90	90	0.150	477.93
MTF	1	9.63	30.39	7.25	90	90.45	90	0.086	263.69
MWW	1	14.39	14.39	25.20	90	90	120	0.233	801.23
NES	1	26.06	13.88	22.86	90	90	90	0.194	701.99
OBW	1	13.91	13.91	30.84	90	90	90	0.324	989.06
PAU	18	35.09	35.09	35.09	90	90	90	0.159	538.21
PON	1	8.91	9.21	16.09	90	90	90	0.094	329.22
RHO	19	15.03	15.03	15.03	90	90	90	0.252	783.40
SAS	1	14.35	14.35	10.40	90	90	90	0.259	794.61
SBE	1	18.53	18.53	27.13	90	90	90	0.307	938.11
SBT	1	17.19	17.19	41.03	90	90	120	0.339	1057.79
SFG	1	25.53	12.58	13.07	90	90	90	0.141	494.75
SFO	1	22.59	13.57	6.97	90	99.02	90	0.249	815.75
STW	1	11.89	11.89	29.92	90	90	120	0.203	804.89
SZR	1	18.87	14.40	7.51	90	90	90	0.117	398.51
TER	1	9.81	23.65	20.24	90	90	90	0.176	647.26

Table A2. 2. Self-diffusion coefficients (in $10^{-8} m^2 s^{-1}$) calculated for sulfur hexafluoride in the studied zeolites. Simulations were carried out at 298 K with two molecules per simulation cell.

Zeolite	D_{avg}	D_x	D_y	D_z	Zeolite	D_{avg}	D_x	D_y	D_z
AFR	0.2031	-	-	0.6100	LAU	-	-	-	-
AFY	0.2594	-	-	0.7735	LEV	-	-	-	-
ASV	-	-	-	-	LTL	0.0666	-	-	0.1969
BEC	0.2736	0.3703	0.3663	0.1026	MEL	0.0008	0.0010	0.0010	0.0005
BOG	0.2892	0.8453	0.0199	-	MFI	0.0302	0.0300	0.0564	0.0114
CFI	0.8558	-	2.5671	-	MOR	0.8245	-	-	2.4735
CHA	-	-	-	-	MTF	-	-	-	-
DDR	-	-	-	-	MWW	-	-	-	-
DON	0.6025	-	1.8065	-	NES	0.0161	0.0374	0.0128	-
EMT	0.4793	0.4416	0.4478	0.5366	OBW	0.0050	0.0082	0.0049	-
EON	0.6589	1.9769	-	-	PAU	-	-	-	-
ERI	-	-	-	-	PON	-	-	-	-
FAU	0.8132	0.8276	0.8319	0.8030	RHO	-	-	-	-
FER	-	-	-	-	SAS	-	-	-	-
LTA	-	-	-	-	SBE	0.2557	0.3845	0.3788	-
ITE	-	-	-	-	SBT	0.4124	0.4659	0.4490	0.3164
ITR	0.0012	0.0007	0.0002	0.0028	SFG	0.0049	-	-	0.0148
ITW	-	-	-	-	SFO	0.1957	0.0117	-	0.5743
IWW	0.0313	-	-	0.0993	STW	0.0029	-	-	0.0088
JRY	-	-	-	-	TER	0.0240	0.0719	-	-
KFI	-	-	-	-					

Table A2. 3. Loading of SF_6 and N_2 and SF_6/N_2 selectivity at the given pressure from the mixture SF_6/N_2 (10:90) at room temperature. The values of pressure were chosen using criteria that combines both high selectivity and SF_6 loading.

Zeolite	Pressure (kPa)	SF_6 loading (mol kg^{-1})	N_2 loading (mol kg^{-1})	Selectivity SF_6/N_2
AFR	300	1.07	0.20	48.39
AFY	300	0.61	0.34	16.31
BEC	300	2.28	0.07	296.06
BOG	300	1.53	0.17	80.74
CFI	300	0.68	0.08	80.25
DON	300	0.55	0.11	43.30
EMT	3000	2.28	0.74	27.61
EON	60	0.35	0.04	74.76
FAU	1000	1.52	0.50	27.64
ITR	300	1.73	0.02	731.10
IWW	300	1.70	0.04	404.12
LTL	1000	1.22	0.27	40.60
MEL	300	1.80	0.11	144.01
MFI	300	1.75	0.11	145.69
MOR	60	0.58	0.08	61.70
NES	300	1.43	0.08	151.24
OBW	300	0.57	0.18	27.79
SBE	1000	1.40	0.64	19.68
SBT	3000	2.93	0.54	48.81
SFG	300	1.28	0.04	327.16
SFO	300	1.68	0.09	169.06
STW	300	0.51	0.52	8.84
TER	100	0.82	0.13	56.17
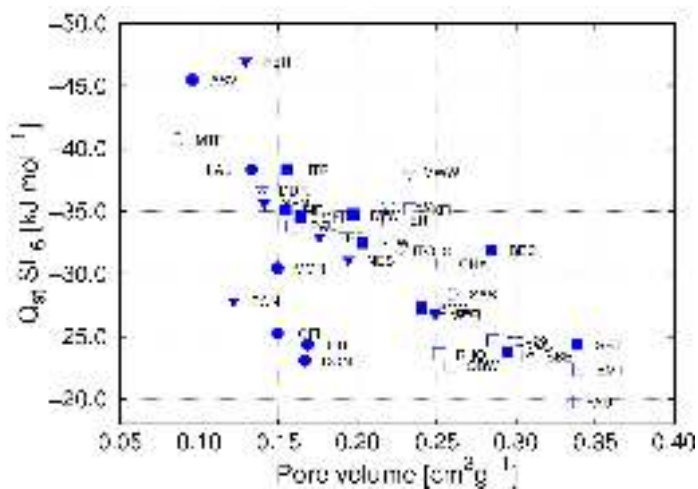
Figure A2.1. Computed isosteric heats of adsorption of sulfur hexafluoride at 298 K as a function of the zeolite pore volume. Open symbols show the results obtained for channel-type zeolites and closed symbol for the interconnected-type. The directionally of the pore space is represented by circles (1D), inverted triangles (2D), and squares (3D).
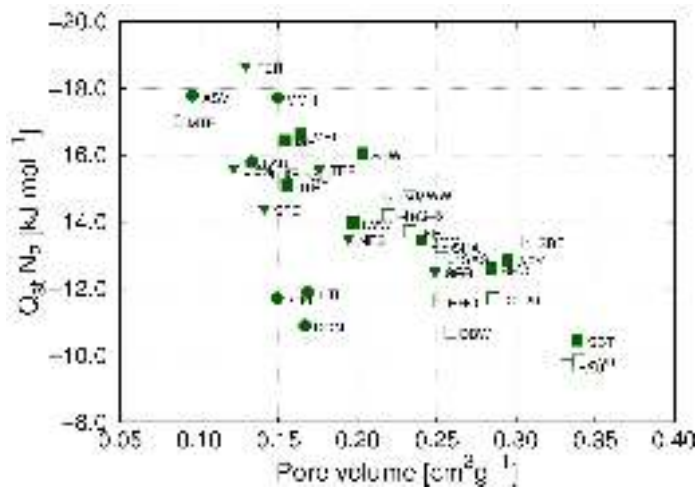
Figure A2.2. Computed isosteric heats of adsorption of nitrogen at 298 K as a function of the zeolite pore volume. Open symbols show the results obtained for channel-type zeolites and closed symbol for the interconnected-type. The directionally of the pore space is represented by circles (1D), inverted triangles (2D), and squares (3D).
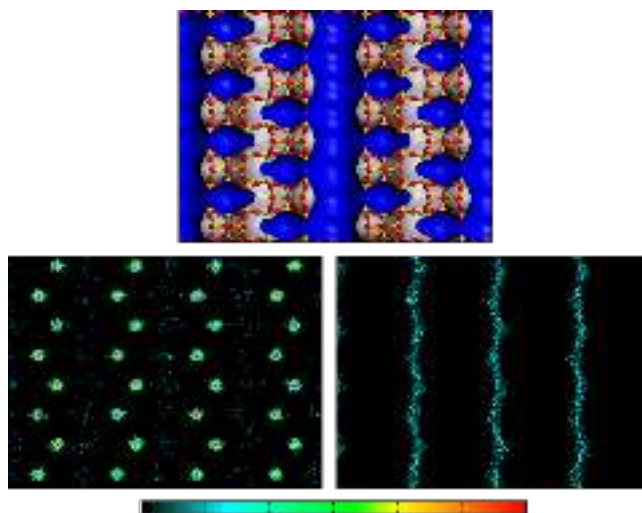
Figure A2. 3. Average occupation profiles obtained in MOR zeolite for nitrogen (bottom left) and sulfur hexafluoride (bottom right). These figures show the projection of the center of mass of the molecules over the z-x plane. The color gra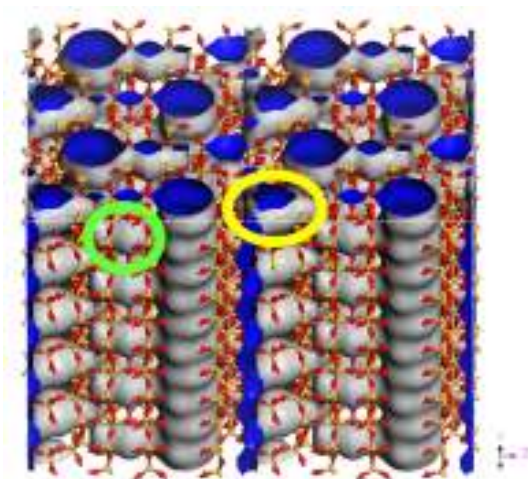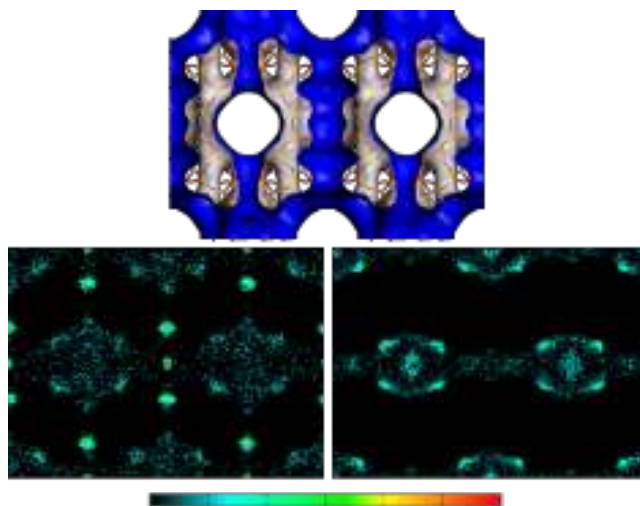duation indicates the occupation density (from black to red). To guide the view we add a representation of the structure (top). Oxygen atoms are depicted in red and silica atoms in yellow. A grid surface is also represented where the accessible part appears in blue while the non-accessible part is colored in gray.
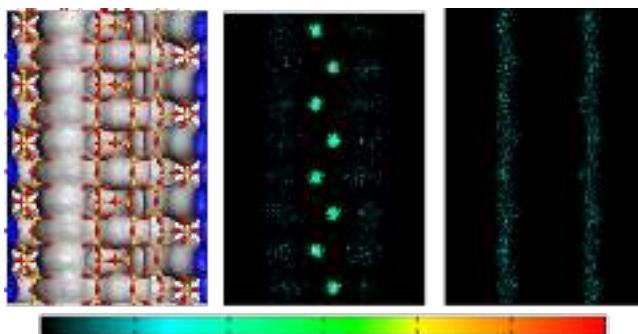
Figure A2. 4. Average occupation profiles obtained in EON zeolite for nitrogen (center) and sulfur hexafluoride (right). These figures show the projection of the center of mass of the molecules over the z-x plane. The color graduation indicates the occupation density (from black to red). To guide the view we add a representation of the structure (left). Oxygen atoms are depicted in red and silica atoms in yellow. A grid surface is also represented where the accessible part appears in blue while the non-accessible part is colored in gray.
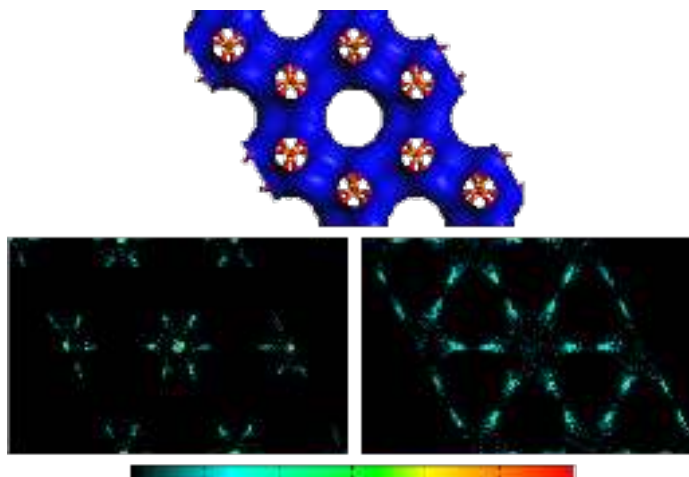
Figure A2. 5. Representation of the atomic structure of zeolite EON. Oxygen atoms are depicted in red and silica atoms in yellow. A grid surface is also represented where the accessible part appears in blue while the non-accessible part is colored in gray. Local structure features are highlighted with circles colored in green (side-pockets) and yellow (T-box).

Figure A2. 6. Average occupation profiles obtained in SBE zeolite for nitrogen (bottom left) and sulfur hexafluoride (bottom right). These figures show the projection of the center of mass of the molecules over the z-x plane (or y-z plane). The color graduation indicates the occupation density (from black to red). To guide the view we add a representation of the structure (top). Oxygen atoms are depicted in red and silica atoms in yellow. A grid surface is also represented where the accessible part appears in blue while the non-accessible part is colored in gray.

Figure A2. 7. Average occupation profiles obtained in AFY zeolite for nitrogen (bottom left) and sulfur hexafluoride (bottom right). These figures show the projection of the center of mass of the molecules over the x-y plane. The color graduation indicates the occupation density (from black to red). To guide the view we add a representation of the structure (top). Oxygen atoms are depicted in red and silica atoms in yellow. A grid surface is also represented where the accessible part appears in blue while the non-accessible part is colored in gray.

References and Notes

[1] Baerlocher, C.; McCusker, L. B.; Olson, D. Atlas of Zeolite Framework types, 6th ed.; Elsevier: London, 2007.

[2] Pluth, J. J.; Smith, J. V. *American Mineralogist* **1990**, *75*, 501-507.

[3] Calligaris, M.; Nardin, G.; Randaccio, L. *Zeolites* **1983**, *3*, 205-208.

[4] Gies, H. Z. *Kristallogr.* **1986**, *175*, 93-104.

[5] Wessels, T.; Baerlocher, C.; McCusker, L. B.; Creyghton, E. J. *Journal of the American Chemical Society* **1999**, *121*, 6242-6247.

[6] Gard, J. A.; Tait, J. M. Proc. 3rd Int. Conf. *Molecular Sieves* **1973**, 94-99.

[7] Hriljac, J.; Eddy, M.; Cheetham, A.; Donohue, J.; Ray, G. *Journal of Solid State Chemistry* **1993**, *106*, 66-72.

[8] Morris, R. E.; Weigel, S. J.; Henson, N. J.; Bull, L. M.; Janicke, M. T.; Chmelka, B. F.; Cheetham, A. K. *Journal of the American Chemical Society* **1994**, *116*, 11849-11855.

[9] Corma, A.; Rey, F.; Rius, J.; Sabater, M. J.; Valencia, S. *Nature* **2004**, *431*, 287-290.

[10] Camblor, M. A.; Corma, A.; Lightfoot, P.; Villaescusa, L. A.; Wright, P. A. *Angewandte Chemie-International Edition* **1997**, *36*, 2659-2661.

[11] Parise, J. B.; Shannon, R. D.; Prince, E.; Cox, D. E. *Zeitschrift Fur Kristallographie*

1983, *165*, 175-190.

[12] Artioli, G.; Stahl, K. *Zeolites* **1993**, *13*, 249-255.

[13] Merlino, S.; Galli, E.; Alberti, A. *Tschermaks Min. Petr. Mitt* **1975**, *22*, 117-129.

[14] Newsam, J. M. *Journal of Physical Chemistry* **1989**, *93*, 7689-7694.

[15] Fyfe, C. A.; Gies, H.; Kokotailo, G. T.; Pasztor, C.; Strobl, H.; Cox, D. E. *Journal of the American Chemical Society* **1989**, *111*, 2470-2474.

[16] van Koningsveld, H.; van Bekkum, H.; Jansen, J. C. *Acta Crystallographica Section B-Structural Science* **1987**, *43*, 127-132.

[17] Gramlich, V. Untersuchung und Verfeinerung pseudosymmetrischer Strukturen. Ph.D. thesis, 1971.

[18] Gordon, E. K.; Samson, S.; Kamb, W. B. *Science* **1966**,*154*, 1004-1007.

[19] McCusker, L. B.; Baerlocher, C. J. *Solid State Chem.* **1984**, 812-822.

Appendix 3

Associated content of:

Adsorption Equilibrium of Nitrogen Dioxide in Porous Materials

Table A3.1. Structural and topological properties of the zeolites under study.

Zeolite	Pore Volume [$cm^3\ g^{-1}$]	Surface Area [$m^2\ g^{-1}$]	Density [$kg\ m^3$]	Channel System	Channel Diameter			Ring sizes
FER	0.066	235.07	1837.870	2D (1D)	4.69	3.40	-	10 8 6 5
TON	0.091	301.41	1968.716	1D	5.11	-	-	10 6 5
MOR	0.150	477.92	1711.056	1D	6.45	-	-	12 8 5 4
MFI	0.164	547.67	1796.342	3D	4.70	4.46	4.46	10 6 5 4
FAU	0.332	1020.88	1342.047	3D - Cages	7.35	7.35	7.35	12 6 4

Table A3.2. Mole fraction of NO_2 and N_2O_4 for the bulk phase reaction dimerization over a temperature range of 273-404 K and a pressure range of 0.1-5 atm. The table shows the results obtained in this work from RxMC simulations in the NPT ensemble and calculated data from Chao et al. for direct comparison.

|	Pt [atm] = 0.1					Pt [atm] = 0.5			
	Mole Fraction		Mole Fraction			Mole Fraction		Mole Fraction	
T [K]	NO_2	N_2O_4	NO_2	N_2O_4	T [K]	NO_2	N_2O_4	NO_2	N_2O_4
273	0.362	0.638	0.342	0.658	273	0.183	0.817	0.172	0.828
298	0.704	0.296	0.672	0.328	298	0.435	0.565	0.405	0.595
318	0.888	0.112	0.879	0.121	318	0.674	0.326	0.659	0.341
360	0.988	0.012	0.987	0.013	360	0.946	0.054	0.942	0.058
375	0.994	0.006	0.994	0.006	375	0.973	0.027	0.971	0.029
404	0.998	0.002	0.998	0.002	404	0.992	0.008	0.992	0.008
	Pt [atm] = 1					Pt [atm] = 5			
	Mole Fraction		Mole Fraction			Mole Fraction		Mole Fraction	
T [K]	NO_2	N_2O_4	NO_2	N_2O_4	T [K]	NO_2	N_2O_4	NO_2	N_2O_4
273	0.130	0.870	0.125	0.875	273	0.005	0.995	0.058	0.942
298	0.331	0.669	0.309	0.691	298	0.151	0.849	0.153	0.847
318	0.556	0.444	0.541	0.459	318	0.297	0.703	0.299	0.701
360	0.902	0.098	0.895	0.105	360	0.699	0.301	0.688	0.312
375	0.949	0.051	0.945	0.055	375	0.811	0.189	0.803	0.197
404	0.985	0.015	0.984	0.016	404	0.932	0.068	0.928	0.072
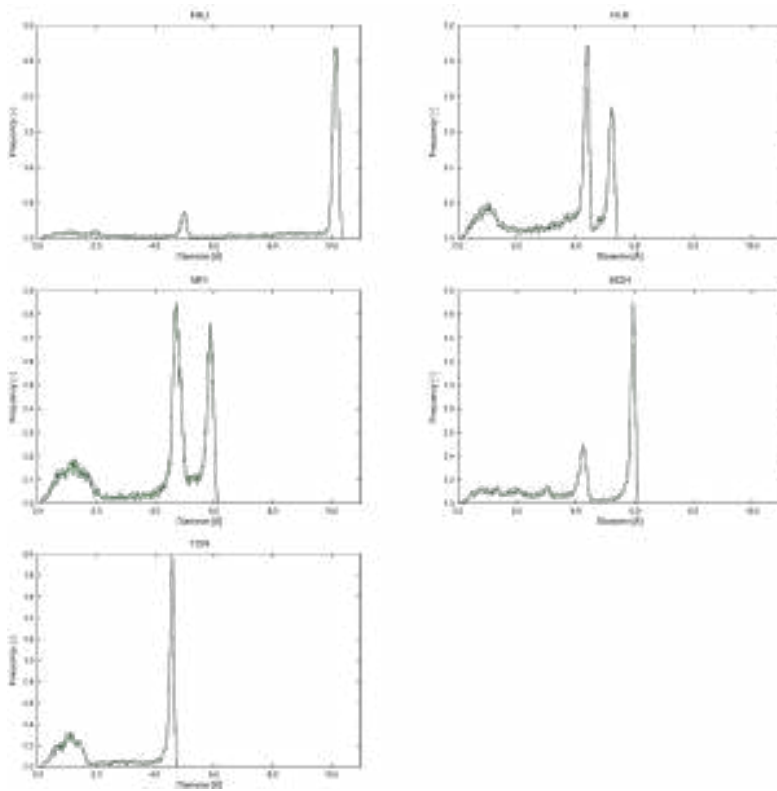
Figure A3.1. Pore-size distributions of the zeolites under study (from top left to bottom right: FAU, FER, MFI, MOR, and TON).
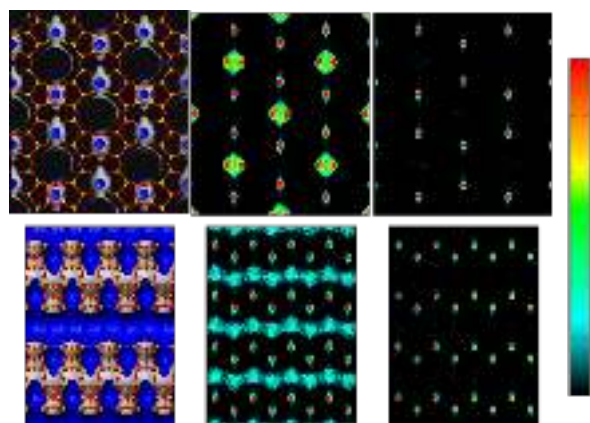
Figure A3. 2. Average occupation profiles for nitrogen dioxide in MOR zeolite at $5x10^2$ kPa and room temperature, obtained from pure component (central column) and binary equimolar mixture NO_2-N_2O_4 (right column). The figures show the projection of the center of mass of the molecules over the x-y (top) and z-y (bottom) planes. The color graduation indicates the occupation density (from black to red). To guide the view a representation of the s tructure (left column) is added (oxygen atoms are depicted in red and silica atoms in yellow). A grid surface is also represented where the accessible part appears in blue while the non-accessible part is colored in gray.
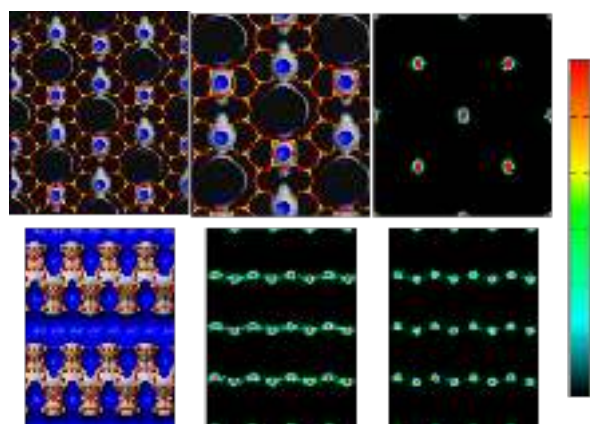

Figure A3. 3. Average occupation profiles for dinitrogen tetroxide in MOR zeolite obtained from pure component at room pressure (central column) and binary equimolar mixture NO_2 -N_2O_4 at 10^3 kPa (right column) and room temperature in both cases. The figures show the projection of the center of mass of the molecules over the x-y (top) and z-y (bottom) planes. The color graduation indicates the occupation density (from black to red). To guide the view a representation of the structure (left column) is added (oxygen atoms are depicted in red and silica atoms in yellow). A grid surface is also represented where the accessible part appears in blue while the non-accessible part is colored in gray.
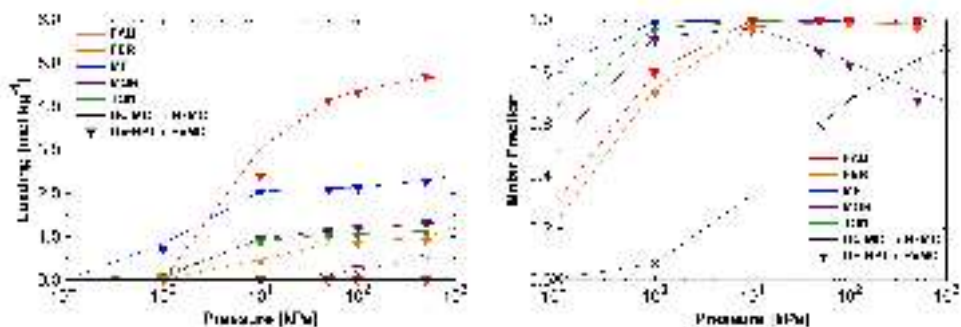
Figure A3.4. Simulated binary mixture adsorption isotherms (left), and mole fractions (right) of NO_2 (empty symbols) and N_2O_4 (full symbols) at room temperature in FAU (red), FER (orange), MFI (blue down triangles), MOR (purple squares), and TON (green triangles). In both figures, results obtained using reactive Grand-Canonical Monte Carlo simulation are depicted as line and those obtained from constant pressure Gibbs ensemble reactive simulations as down pointed triangles. To clear the figure and guide the eye in (right), only the N_2O_4 mole fractions are plotted (the sum of both mole fractions is equal to 1) and the bulk mole fractions are also added in black. Reaction move is switched on here.

Associated content of:

Discovery of an Optimal Porous Crystalline Material for the Capture of Chemical Warfare Agents

Computational Details. Force fields.

Table A4. 1. Parameters for non-bonded interactions.

	ε/k_B(K)	σ(Å)	Charge (e^-)		ε/k_B(K)	σ(Å)	Charge (e^-)
Mustard				*Soman*			
S	228.7044	3.330768	-0.261284	CH$_3$	98.0000	3.750000	-0.080000^c/-0.100000^d/-0.150000^f
CH$_2$	48.7044	3.361100	0.140655^a/0.164474^b	CH	10.0000	4.330000	0.430000
Cl	150.6672	3.469820	-0.174487	C	0.5000	6.400000	0.540000
DES				O-(CH)	55.0000	2.800000	-0.630000
S	199.0000	3.580000	-0.300000	O=(P)	79.0000	3.050000	-0.770000
CH$_2$	46.0000	3.950000	0.150000	P	86.0000	4.000000	1.400000
CH$_3$	98.0000	3.750000	0.000000	F	26.7000	2.950000	-0.340000
Sarin				*DIFP*			
CH$_3$	98.0000	3.750000	-0.100000^d/-0.080000^e	O=(P)	79.0000	3.050000	-0.720000
CH-(O)	10.0000	4.680000	0.620000	O-(CH)	55.0000	2.800000	-0.670000
O-(CH)	55.0000	2.800000	-0.630000	CH-(O)	10.0000	4.330000	0.630000
O=(P)	79.0000	3.050000	-0.770000	CH$_3$	98.0000	3.750000	-0.100000
P	86.0000	4.000000	1.400000	F	26.7000	2.950000	-0.360000
F	26.7000	2.950000	-0.340000	P	86.0000	4.000000	1.560000
DMMP				*Water (TIP4P)*			
CH$_3$	98.0000	3.750000	0.280000^c/-0.140000^d	O	77.9360	3.154000	0.000000
O-(CH$_3$)	55.0000	2.800000	-0.530000	H	-	-	0.520000
O=(P)	79.0000	3.050000	-0.800000	L	-	-	-1.040000
P	86.0000	4.000000	1.440000				

^{a}Site adjacent to Cl. ^{b}Site adjacent to S. ^{c}Site adjacent to oxygen. ^{d}Site adjacent to phosphorus. ^{e}Site adjacent to CH group. ^{f}Site adjacent to C.

Table A4. 2. Vibration and Bending Parameters for DMMP, Sarin, Soman, Mustard, DES, and water.

Vibration	Bond length (Å)	Bending	Bond angle (deg)	k_θ/k_b (K)
P=O	1.4580	⊲O=P-CH3	116.30	80586
P-CH$_3$	1.7900	⊲O=P-O	116.50	100794
P-O	1.5800	⊲CH$_3$-P=O	104.30	40894
O-CH$_3$	1.4100	⊲CH$_3$-O-P	121.00	80586
CH$_3$-CH	1.5400	⊲O-P-O	106.50	62500
CH-O	1.4100	⊲CH$_3$-CH-O	106.00	62500
CH-C	1.5400	⊲CH$_3$-CH-CH$_3$	114.00	62500
CH$_3$-C	1.5400	⊲CH$_3$-C-CH$_3$	109.40	62500
F-P	1.5800	⊲CH$_3$-P-F	104.30	40894
S-CH$_2$	1.8200	⊲CH$_3$-CH$_2$-S	114.00	62500
CH$_2$-CH$_3$	1.5400	⊲CH$_2$-CH$_2$-S	109.47	65400
CH$_2$-CH$_2$	1.5400	⊲CH$_2$-S-CH$_2^a$	99.00 4	5550
CH$_2$-Cl	1.7670	⊲CH$_2$-S-CH$_2^b$	109.47	57000
O-H	0.9575	⊲Cl-CH$_2$-CH$_2$	109.47	58080
O-L	0.1500	⊲H-O-L	52.26	-
		⊲H-O-H	104.52	-

^{a}Bending parameters for DES. ^{b}Bending parameters for mustard gas.

Table A4. 3. Vibration and bending parameters for DIFP.

	k_{bond}/k_b (K)	Bond length (Å)	Bending	Bond angle (deg)	k_θ/k_b (K)
P=O	7325119.2	1.480	⊲O=P-F	113.00	65666.4
F-P	324237.6	1.630	⊲O=P-O	117.44	69055.2
P-O	346992.0	1.614	⊲F-P-O	101.72	72182.4
O-CH	412800.0	1.473	⊲O-P-O	103.22	62325.6
CH-CH₃	226560.0	1.520	⊲P-O-CH	120.66	80359.2
			⊲O-CH-CH₃	107.40	62325.6
			⊲CH₃-CH-CH₃	113.99	62325.6

Water molecule is defined as rigid, with fixed bond lengths and angles. The TraPPE force fields (sarim, soman, and DMMP) as well as Müller et al.(Mustard) uses fixed bond lengths, while the Vishnyakov et al. force field (DIFP) uses a harmonic potential to model bond stretching [4.1]:

$$U_{bond} = \frac{1}{2}k_{bond}(l - l_0)^2 \qquad (4.1)$$

where K_Θ is the force constant and l_0 is the equilibrium bond length. In all force fields, a harmonic potential was used to describe bond angle bending [4.2]:

$$U_{bend} = \frac{1}{2}k_\Theta(\Theta - \Theta_0)^2 \qquad (4.2)$$

where Θ is the measured bond angle, Θ_0 the equilibrium bond angle, and k_Θ the force constant.

Table A4. 4. Torsional Parameters for DMMP, Sarin, and Soman; DES; mustard gas; and DIFP.

Vibration	C_0/k_b (K)	C_1/k_b (K)	C_2/k_b (K)	C_3/k_b (K)	C_4/k_b (K)	C_5/k_b (K)	f
[a]O=P-O-CH₃	1534.91	-1102.11	291.88	397.57	-	-	-0.15
[a]CH₃-CH-O-P	1041.22	-753.00	432.00	227.00	-	-	1.88
[a]CH₃-P-O-CH	57.48	1476.00	184.10	0.00	-	-	-0.34
[a]O=P-O-CH	2996.00	-1467.00	215.00	-31.60	-	-	0.44
[a]CH₃-C-CH-O	0.00	176.6.00	-53.30	769.90	-	-	0.00
[a]CH₃-C-CH-CH₃	0.00	355.00	-68.20	791.30	-	-	0.00
[a]CH₂-S-CH₂-CH₃	0.00	367.60	-270.18	581.64	-	-	0.00
[a]P-O-CH-CH₃	1038.36	-750.84	430.80	226.32	-	-	1.88
[b]F-P-O-CH	6015.72	-852.36	315.36	1647.48	-520.68	-662.40	-

	C_0/k_b (Krad²)	τ					
[c]CH₂-S-CH₂-CH₂	710.40	180.0					
[c]Cl-CH₂-CH₂-S	710.40	180.0					

Rotation about dihedral angles was controlled through a cosine series[a], which included a phase angle term f to account for asymmetric rotational barriers (4.3):

$$U_{Tors} = C_0 + C_1[1 + cos(\varphi + f)] + C_2[1 - cos(2\varphi + f)] + C_3[1 + cos(3\varphi + f)] \qquad (4.3)$$

where φ is the dihedral angle, and C_i are Fourier constants. Additionally, a six-cosine dihedral[b] [4.4] is employed to describe the F-P-O-CH dihedral angle for DIFP.

$$U_{Tors} = \sum_{n=0}^{5} C_n cos^n(\varphi) = C_0 - C_1 cos^1(\varphi) + C_2 cos^2(\varphi) - C_3 cos^3(\varphi) + C_4 cos^4(\varphi) - C_5 cos^5(\varphi)$$

$$(4.4)$$

Finally, the harmonic dihedral potentialc was used by Müller et al. to describe intramolecular rotations about bonds in mustard gas molecule [4.5].

$$U_{Tors} = \frac{1}{2} C_0(\varphi - \tau)^2 \qquad (4.5)$$

HTS adsorption results.
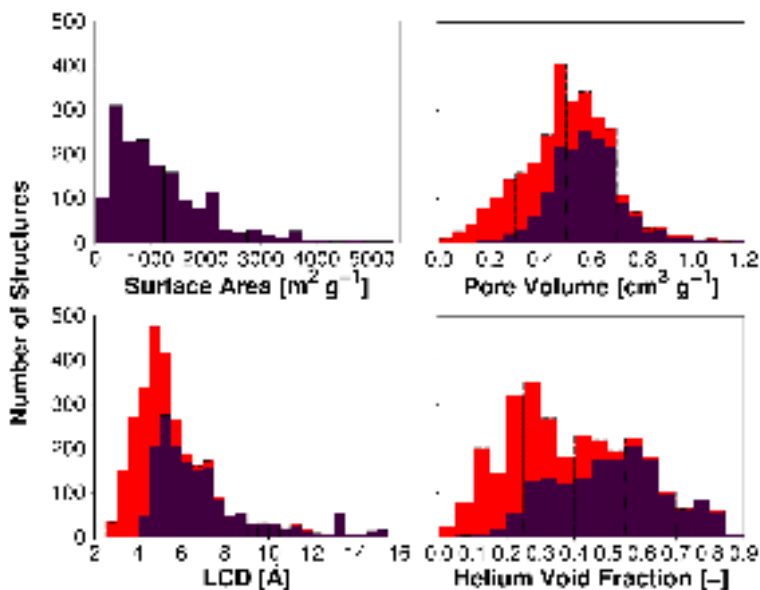
Figure A4.1. Histograms of structural properties for the 2932 MOF structures from the DDEC database: gravimetric surface area, pore volume, large cavity diameter, and helium void fraction. Gravimetric surface area was calculated using a probe radius of 1.86 Å (corresponding to N_2). Structures with PLD lower than 1.86 Å are depicted in red.
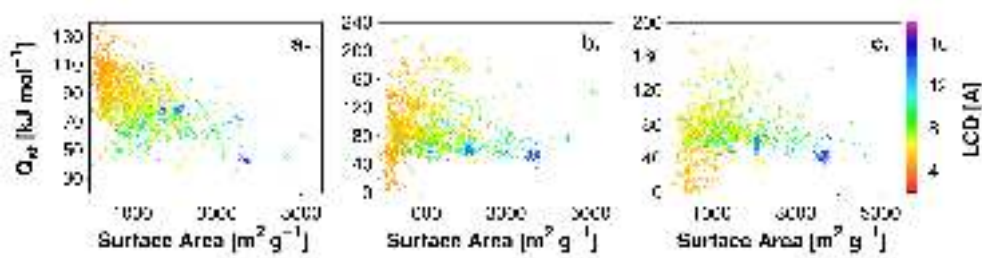
Figure A4.2. Heat of adsorption (Q_{st}) as a function of gravimetric surface area of 1647 MOFs for a. mustard gas, b. sarin, and c. soman. Color code represents the largest cavity diameter (LCD) of MOF structures.
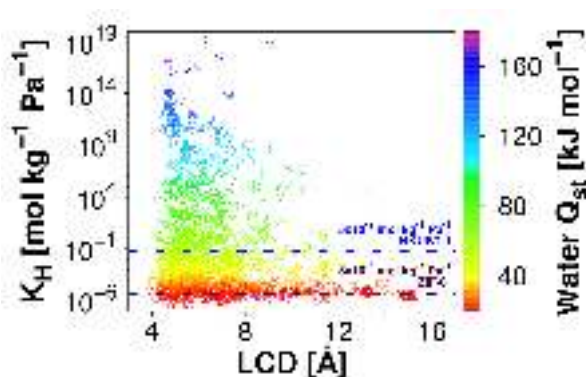
Figure A4.3. Henry's constants (K_H) for water as a function of the largest cavity diameter (LCD) in 1647 MOF structures at 298 K. Purple and blue dashed lines depict water K_H in ZIF-8 and HKUST-1, respectively, as benchmarks for hydrophobicity and hydrophilicity in MOFs. Color code represents isosteric heat of adsorption (Q_{st}) for water.
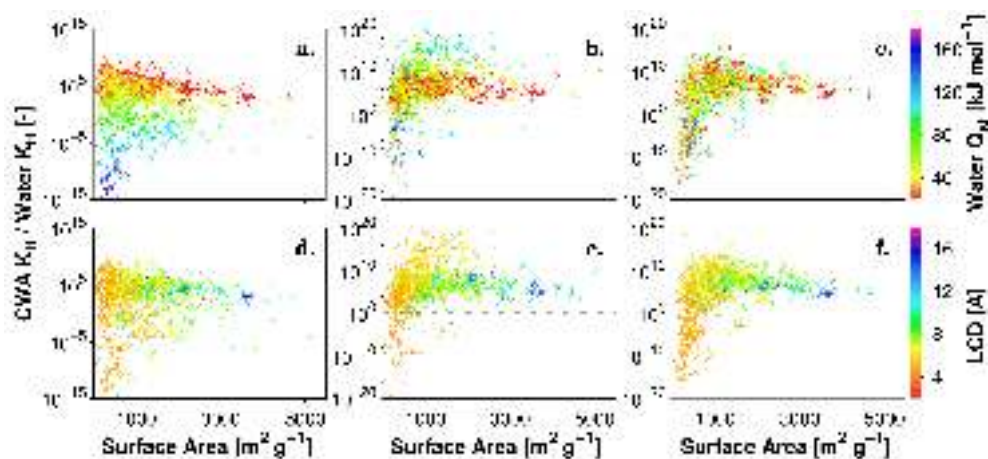
Figure A4.4. Selectivity of a., d. DES, b., e. DMMP, and c., f. DIFP over water based on the K_H ration as a functional of surface area in 1647 MOF structures at 298 K. The color code represents the isosteric heat of adsorption (Q_{st}) for water (a-c) and the largest cavity diameter (d-f) for each MOF structure.
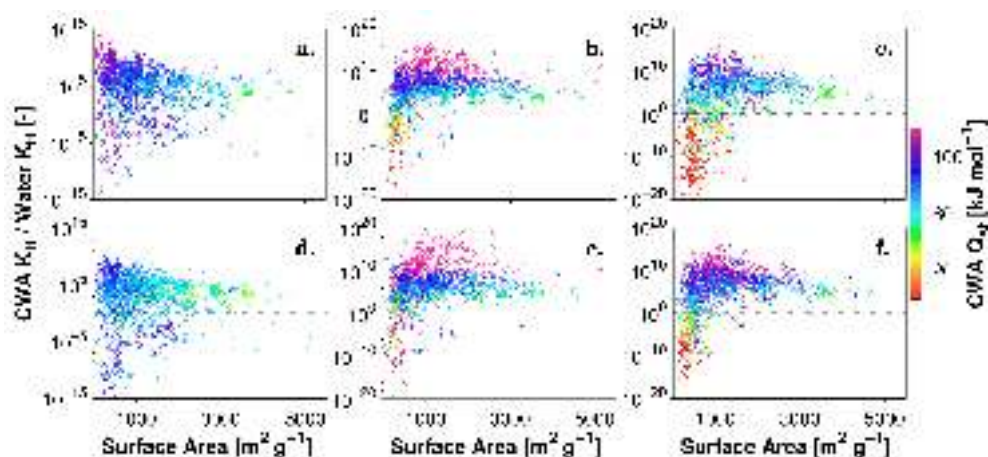
Figure A4.5. Selectivity of a. mustard gas, b. sarin, c. soman, d. DES, e. DMMP, and f. DIFP over water based on the K_H ration as a function of the surface area in 1647 MOF structures. The color code shows the isosteric heat of adsorption (Q_{st}) for each CWA or simulant.
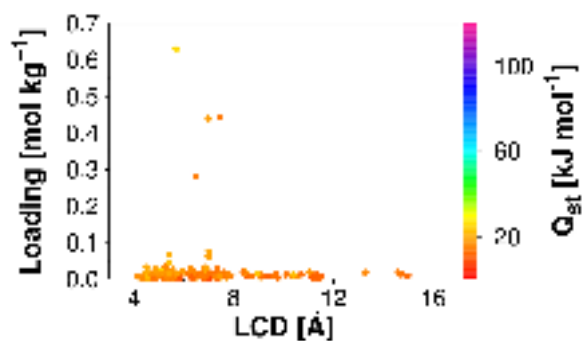
Figure A4.6. GCMC simulations of water adsorption at 3280 Pa (i.e. 80% RH) as a function of the largest cavity diameter (LCD) for 156 selected hydrophobic MOFs. The color code shows the isosteric heat of adsorption (Q_{st}) for water.
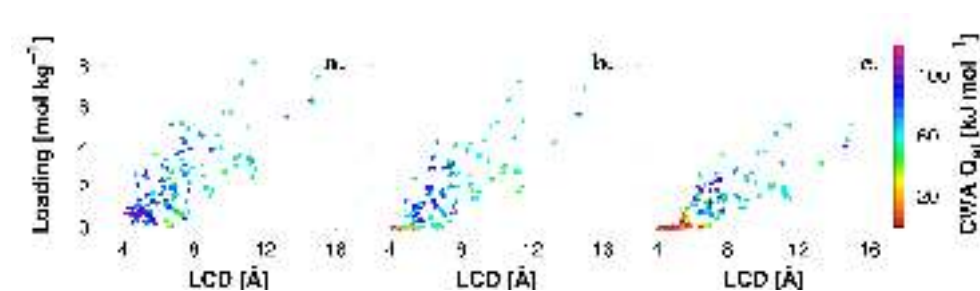

Figure A4.7. GCMC calculated a. mustard, b. sarin, and c. soman loading at 13.8 Pa (mustard), 0.8 Pa (sarin and soman) as a function the largest cavity diameter (LCD) of 156 selected hydrophobic MOFs. The color code shows the isosteric heat of adsorption (Q_{st}) for each CWA.

Selection of top MOFs

The synthesis of the first selected MOF structure (CSD code: **BIBXUH**), ([$Ni_8(OH)_4$ $(H_2O)_2(L)_6]_n$, where L = 1,4-(4-bispyrazolyl)benzene (H_2BPB), was first reported by Padial et al., along with an isoreticular series of MOFs based on bi-pyrazolate linkers and Ni^{II} hydroxo clusters. The design of this MOF was oriented to the capture of VOCs under moisture conditions. **Co26NDP**[1] was also highlighted in our results, having built up by interconnecting 1D Co^{II} polymer chains with naphthalene instead of benzene as spacer in the bipyrazolate linker. Finally, the MOF referenced as **UTEWOG** was reported by Colombo et al. as one of four framework based on the ligand 1,3,5-tris(1H-pyrazol-4-yl)benzene (H_3BTP). This MOF, also named $Ni_3(BTP)_2$, shows an expanded sodalite-like topology.
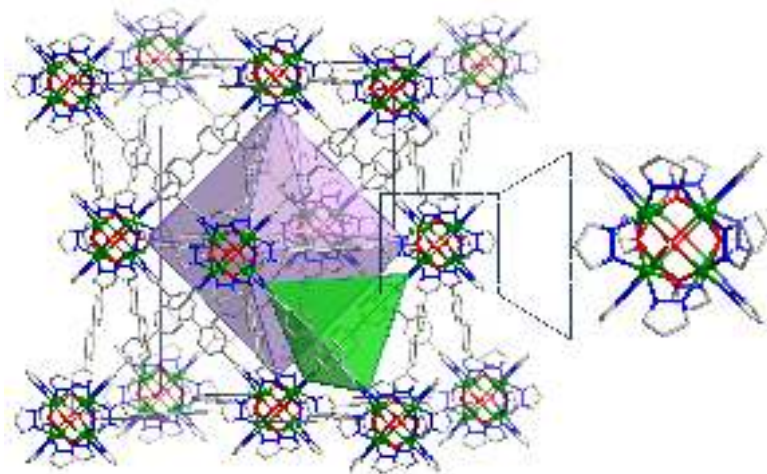

Figure A4.8. Crystal structure of NiBPB (CCDC code: BIBXUH). The inset shows the Ni(II) hydroxo cluster. Carbon, gray; nitrogen, blue; nickel, green; oxygen, red. Hydrogen atoms have been omitted for simplification.

---

[1]This MOF corresponds to core-mof-ddec-365 from the work from Nazarian et al.; no CSD code was provided in the paper, and is not found in the CSD, which strongly suggests it is a hypothetical structure.
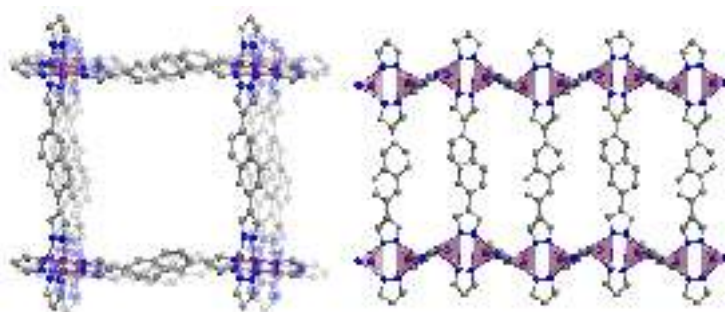
Figure   A4. 9.   Atomic   representation   of   the   structure   of   Co26NDP.   Car-
bon,   nitrogen,   and   cobalt   atoms   are   depicted   in   grey,   blue,   and   pur-
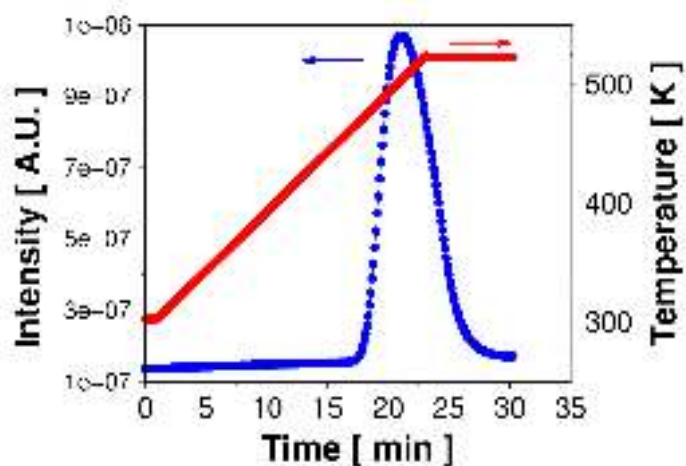ple   respectively.   Hydrogen   atoms   have   been   omitted   for   simplification.

Figure   A4. 10.   Temperature   programed   desorption   of $[Ni_3(BTP)_2]$,   blue   curve,   af-
ter   the   measurement   of   the   DES   breakthrough   curve.   20   mL min^{-1} flow   of N_2
and   a   heating   rate   of   10 ^0C min^{-1}.   The   released   DES   was   studied   by   means   of
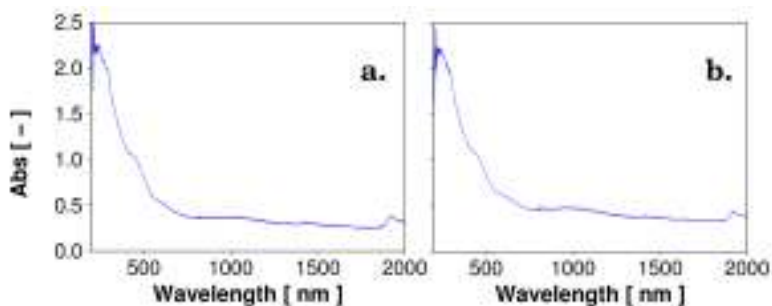a   mass   spectrometer.   Red   curve   represents   the   evolution   of   temperature   with   time.

Figure A4.11. TGA of hydrated [Ni$_3$(BTP)$_2$] a. before and b. after the DES breakthrough curve measurement at RH (80%). Air atmosphere and heating rate of 20 ^{o}C min^{-1}. [Ni$_3$(BTP)$_2$]$*$7.5H$_2$O (H$_2$O calc. 15.7%; found: 15.7%) [Ni$_3$(BTP)$_2$]$*$4H$_2$O$*$0.5(DES), (H$_2$O calc. 8.6%; found: 8.5%) (DES calc. 5.4%; found: 4.6%).
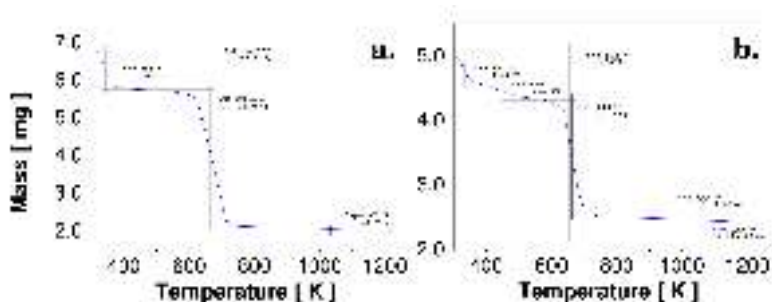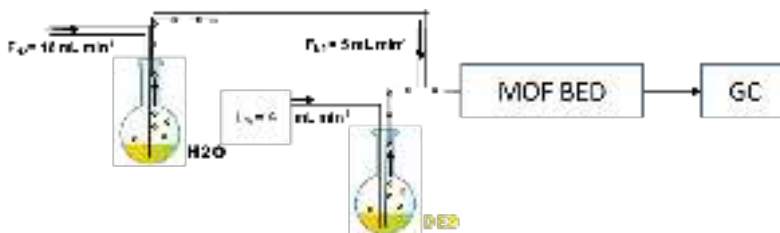

Figure A4.12. Diffuse reflectance spectra of hydrated [Ni$_3$(BTP)$_2$] a. before and b. after the DES breakthrough curve measurement at RH (80%).

Scheme A4.1. Schematic representation of the experimental setup used to evaluate diethylsulphide (DES) capture by [Ni$_3$(BTP)$_2$] MOF under humid conditions (80% relative moisture) at room temperature.

Table A4. 5. Structural properties for the top three MOF structures and calculated adsorption loadings for mustard, sarin, soman and water at 298 K and at 3280, 13.8 Pa and 0.8 Pa for water, mustard, and sarin and soman respectively.

CCDC	Density g cm^{-3}	LCD Å	GAS m^2 g^{-1}	HVF (−)	Mustard mol kg^{-1}	Sarin mol kg^{-1}	Soman mol kg^{-1}	Water mol kg^{-1}
BIBXUH	0.74	14.7	2523	0.77	6.151	5.574	4.327	0.013
Co26NDP	0.65	10.7	2435	0.70	7.132	6.317	4.649	0.014
UTEWOG	0.75	14.6	1702	0.81	6.315	5.621	4.017	0.019

Table A4. 6. Results obtained from Widom simulations in the top three MOF structures for mustard, sarin, soman and Water at 298 K.

CCDC	Mustard Q_{st} kJ mol^{-1} Pa^{-1}	Mustard K_H mol kg^{-1} Pa^{-1}	Sarin Q_{st} kJ mol^{-1} Pa^{-1}	Sarin K_H mol kg^{-1} Pa^{-1}	Soman Q_{st} kJ mol^{-1} Pa^{-1}	Soman K_H mol kg^{-1} Pa^{-1}	Water Q_{st} kJ mol^{-1} Pa^{-1}	Water K_H mol kg^{-1} Pa^{-1}	Mustard/Water SelQ$_{st}$ (-)	Mustard/Water SelK$_H$ (-)	Sarin/Water SelQ$_{st}$ (-)	Sarin/Water SelK$_H$ (-)	Soman/Water SelQ$_{st}$ (-)	Soman/Water SelK$_H$ (-)
BIBXUH	-58.19	2.32E+00	-58.99	3.44E+00	-62.97	3.67E+01	-13.17	3.75E-06	4.42	6.19E+05	4.48	9.17E+05	4.78	9.79E+06
Co26NDP	-65.86	9.65E+00	-62.24	6.14E+00	-68.14	3.33E+02	-12.61	3.82E-06	5.22	2.53E+06	4.94	1.61E+06	5.40	8.73E+07
UTEWOG	-80.42	1.28E+03	-82.33	1.17E+04	-90.09	1.04E+06	-14.19	4.73E-06	5.67	2.70E+08	5.80	2.47E+09	6.35	2.21E+11

List of publications

Publications included in this thesis

- **Chapter 2**

  Matito-Martos, I.; Martin-Calvo, A.; Gutiérrez-Sevillano, J. J.; Haranczyk, M.; Doblaré, M.; Parra, J. B.; Ania, C. O.; Calero, S. "Zeolite Screening for the Separation of Gas Mixtures Containing SO_2, CO_2 and CO" *Phys. Chem. Chem. Phys.*, 16 (19884–19893), **2014**.

- **Chapter 3**

  Matito-Martos, I.; Álvarez-Ossorio, J.; Gutiérrez-Sevillano, J. J.; Doblaré, M.; Martin-Calvo, A.; Calero, S. "Zeolites for the Selective Adsorption of Sulfur Hexafluoride" *Phys. Chem. Chem. Phys.*, 17 (8121-18130), **2015**.

- **Chapter 4**

  Matito-Martos, I.; Rahbari; A.; Dubbeldam, D.; Martin-Calvo, A.; Vlugt, T. J. H.; Calero, S. "Adsorption Equilibrium of Nitrogen Dioxide in Porous Materials" *Phys. Chem. Chem. Phys.*, 20 (4189-4199), **2018**.

- **Chapter 5**

  Matito-Martos, I.; Moghadam, P. Z.; Li, A.; Colombo, V.; Navarro, J. A. R.; Calero, S.; Fairen-Jimenez, D. "Discovery of an Optimal Porous Crystalline Material for the Capture of Chemical Warfare Agents" *Chemistry of Materials*, 30 (4571-4579), **2018**.

Other publications directly related to this thesis

- Matito-Martos, I.; Sepúlveda, C.; Gómez, C.; Acién, G. ; Pérez-Carbajo, J.; Delgado, J. A.; Águeda, V. I.; Ania, C. O.; Parra, J. B.; Calero, S.; Anta, J. A. "Potential CO_2 capture from Flue Gas by Physicochemical and Biological methos: a Comparative Study" *Submited*, **2018**.

- Matito-Martos, I ; Martin-Calvo, A.; Ania, C. O.; Parra, J. B.; Vicent-Luna, J. M.; Calero, S. "Ammonia Adsorption Using Zeolites" *Submited*, **2018**.

- Matito-Martos, I,; García-Reyes, J.; Martin-Calvo, A.; Dubbeldam, D.; Calero, S. "Improving Ammonia Production Using Zeolites" *Submited*, **2018**.

- Cacho-Bailo, F.; Matito-Martos, I.; Pérez-Carbajo, J.; Etxeberría-Benavides, M.; Karvan, O.; Sebastián, V.; Calero, S.; Téllez, C.; Coronas, J."On the molecular mechanisms for the H_2/CO_2 separation performance of zeolite imidazolate framework two-layered membranes" *Chem. Sci.*, 8 (325-333), **2017**.

- Martin-Calvo, A.; Matito-Martos, I.; Gutiérrez-Sevillano, J. J.; Vlugt, T. J. H.; Calero, S. "Identifying Zeolite Topologies for Storage and Release of Hydrogen" *J. Phys. Chem. C.*, 122 (12485-12493), **2018**.

- Pérez-Carbajo, J.; Matito-Martos, I.; Balestra R. G., S.; Mihalis, N. T.; van de Sanden, M. C. M.; Delgado, J. A.; Águeda, V. I.; Merkling, P. J. "Zeolites for CO_2-CO-O_2 Separation to Obtain CO_2-neutral Fuels" *ACS Appl. Mater. Interfaces.*, 10 (20512-20520), **2018**.

Non-peer reviewed journals

- Matito-Martos, I. "Zeolitas: Materiales con Aplicaciones Tecnológicas y Medioambientales" *MoleQla*, ISSN 2173-0903, 11 (9.1), **2013**.

Acknowledgements/Agradecimientos

He aquí el final de la aventura, la Calle Victoria y la liga, el sueño de todo maestro Poké...
No espera, que esto iba de otra cosa ...

Entiéndase la confusión, no en vano esto también ha sido una verdadera aventura. Una aventura que empezaba varios años atrás ya, conmigo recién acabando la carrera y con la propuesta de Sofía C. sobre la mesa para emprender el camino del doctorado. Por aquellos entonces lo veía lejos, un imposible ... ¿yo?, ¿doctor?, parecía casi una broma. Pero ahora ya estamos aquí, con el imposible al alcance de la mano, con el camino recorrido y la mochila llena de recuerdos, sabiduría y vivencias. Y es justo ahora cuando hay que mirar atrás por última vez para coger impulso y para recordar y agradecer a todos los que han hecho de este imposible una realidad.

El primer agradecimiento no puede ser a otras personas que a mis dos directoras Sofía C. y Ana M. Muchas gracias por tantas horas, tanto esfuerzo y tanta dedicación. Gracias por confiar en mí incluso cuando ni yo mismo a veces confiaba, cuando me atascaba y todo me parecía cuesta arriba. Por hacerme dar siempre un poquito más y propinarme los sutiles empujoncitos necesarios para que no me desviase del camino. Esta tesis no habría sido posible sin vuestra guía. Gracias por estar siempre ahí.

Gracias a Juanjo G. por los primeros pasos cuando era un joven e inexperto proyecto fin de carrera que no había tocado nada parecido a Linux en la vida. Aún guardo esos primeros apuntes donde aprendía a hacer "cd" y esas cosas de "hackers", como las veía al sufrir la primera bajada desde el mundo de la amigable (o no tanto) interfaz gráfica de Windows a la oscuridad de una terminal en la que me he pasado varios añitos (y ahora hasta me gusta). También agradecer en este aspecto más "técnico" al ya-no técnico de laboratorio Julio P., por sus años en los que era al arregla-todo y por haber cuidado tan bien de Tritón y Kraken. Agradecer también a Julio P. junto con Jose M. V. y Salvador R. por enseñarme todo que he aprendido sobre "scripts" (y dejarme claro que ni de lejos esto es como programar), sin los cuales no habría sobrevivido ante tal vorágine de datos,

simulaciones y cribados de estructuras. Agradecer igualmente a Jose M. V. por haberme enseñado a prisa y corriendo a escribir en LateX y ofrecerme la plantilla sobre la que se ha escrito esta tesis, y a Azhara L. y a todos los anteriores por servirme de apoyo técnico ante emergencias durante la escritura.

Gracias a Raspa, a todos los rasposos con los que he compartido tantas horas, y perdón si se me olvida alguno, pero ahora que ya tengo los 30 puedo echarle la culpa a la edad. Gracias a mis compañeros de aventura, a la vieja guardia. Gracias a Jose M. V., Salvador R., Julio P., Paco L., Rocio B., Jose M. O., Chema O. y Azhara L. por tantas cosas vividas en el laboratorio y fuera de él. Gracias por las comidas, por los congresos, por los caminantes, por el máster... ¡Qué máster! A los doctores Patrick M., Juan A. M., Paula G., Rabdel R. y Said H. por vuestra ayuda, por vuestros consejos y por haber estado ahí para enriquecer aún más esta tesis con vuestros conocimientos y aportes. Gracias también a la, y para ello me tomo la licencia de usar el término acuñado en su tesis por el ya doctor Salvador R., *"Raspa Next Generation"*, Madero, Carmen, y Pilar, pues puedo marchar tranquilo sabiendo que el legado de Raspa queda en las mejores manos ... *"Mi guardia ha terminado"*. Gracias tambié Javier G., por todo lo que ha estado trabajando este año y por ser tan buen chaval. Y en general gracias a todo lo que constituye o ha constituido en estos años el grupo Raspa y sus alrededores, un lugar donde no solo se hace ciencia de calidad y rigor, sino donde además existe un ambiente de colaboración en el que da gusto trabajar e investigar.

Gracias a David F. por acogerme en la Universidad de Cambridge y brindarme una magnifica oportunidad de realizar allí la estancia y a todas las personas de su grupo de investigación por hacerme la estancia tan agradable y provechosa, personal y científicamente. Thanks a lot to Peyman for supervising my work during my visit and the support during this time.

Gracias también al resto de colaboradores que han hecho posible los artículos de esta tesis y que la han llenado de aportes y matices. Especialmente darle las gracias a J. B. Parra por su calidad como científico y como persona y por enseñarme tanto del mundo de la zeolita desde el otro lado, el oscuro lado del laboratorio que tantos problemas a la par que alegrías me ha traído en estos años de tesis. También agradecer a Conchi A. por el apoyo experimental de los trabajos presentados.

No olvidarme de todos los amigos que han estado ahí. A Cris, Migue, Hilario, Lana, Jose, Jesús y muchos otros, gracias por acompañarme en el camino. Gracias también a todos los compañeros y compañeras del MAES que me han hecho este último año de trabajo acelerado más agradable y llevadero. A mis infatigables compañeras de mesa del genérico E. Cristina y Ana por esas mañanas pasando frío en las clases y esperando el momento de desayunar. Muchas gracias también a los compañeros del específico y

en especial a los "A-Margaos", Daniel y Jose por tantos ratitos buenos. Y no puedo, ni quiero olvidarme de Rocío por haber sido sin duda la mejor compañera de prácticas que podía haberme tocado y por hacerlas tan agradables. El futuro está asegurado con profesores/as así y con estudiantes tan buenos como los del curso de primero de bachillerato del IES Juan de Mairena, a vosotros también os doy las gracias.

Por último, y no por ello menos importante, agradecer a toda mi familia, sin la que tampoco estaría donde estoy. Darles las gracias a todos por apoyarme a pesar de seguir sin saber del todo a que me he estado dedicando estos años. Gracias a mis padres May y Nicolas por estar ahí siempre. A mi hermano Nicolás y a mi sobrino, que es lo más bonito que hay.

Gracias

"Este mundo está habitado por ~~criaturas~~
estructuras llamadas ~~pokémon~~ zeolitas ...
yo las estudio como profesión."

Profesor Oak, Pueblo Paleta